

Copyright

by

Chenchen Jimmy Li

2016

**The Dissertation Committee for Chenchen Jimmy Li Certifies that this is the
approved version of the following dissertation:**

**In-Situ, High-Resolution Radar Imaging of Dynamic Targets Using an
Ultra-Wideband Radar**

Committee:

Hao Ling, Supervisor

Ali Yilmaz

Mark Hamilton

Surya Santoso

Adrian Lin

**In-Situ, High-Resolution Radar Imaging of Dynamic Targets Using an
Ultra-Wideband Radar**

by

Chenchen Jimmy Li, B.S.; M.S.E.

Dissertation

Presented to the Faculty of the Graduate School of

The University of Texas at Austin

in Partial Fulfillment

of the Requirements

for the Degree of

Doctor of Philosophy

The University of Texas at Austin

August 2016

Acknowledgements

I would like to take this opportunity to thank the people that have made this dissertation possible. First and foremost, I would like to thank my supervisor, Dr. Hao Ling, for his unwavering support, keen insight, wonderful guidance, and never-ending enthusiasm. He has helped guide me through the thick and thin of research and has helped me grow as a graduate student. I am also grateful to Dr. Ali Yilmaz, Dr. Mark Hamilton, Dr. Surya Santoso, and Dr. Adrian Lin for serving on my dissertation committee and providing helpful comments.

My appreciation goes out to my fellow lab members: Dr. Shang-Te Yang, Dr. Ick-Jae Yoon, Dr. Aale Naqvi, Dr. Nicholas Whitelonis, and Mr. Xiao Liu. I have learned a lot through them, and their research topics have broadened my understanding of the field.

Special thanks to the UT students who have assisted in various parts of my dissertation: Ms. Tiffany Dang, Mr. Li Wang, and Mr. Kevin Chaloupka. I'd also like to extend my appreciation to the high school students who worked in our lab during the summer, Mr. Reid Li and Mr. Sam Grayson.

Special thanks to Mr. Alan Petroff of Time Domain Corporation for providing technical support on the PulsON radars, as well as Mr. Colton Bostick of UAV Direct and Mr. Lenny Tropiano of FlyTheSkyDrone Productions for providing consumer drones for measurement.

This work was supported in part by the National Science Foundation under Grant ECCS-1232152, and in part by the Thrust 2000-Archie W. Straiton Endowed Graduate Fellowship in Engineering #2. I would also like to thank EM Software & Systems (now part of Altair) for providing FEKO GOLD licensing and software support.

Finally, I would like to thank my family and friends for their support and encouragement over the years.

CHENCHEN JIMMY LI

The University of Texas at Austin

August 2016

In-Situ, High-Resolution Radar Imaging of Dynamic Targets Using an Ultra-Wideband Radar

Chenchen Jimmy Li, Ph.D.

The University of Texas at Austin, 2016

Supervisor: Hao Ling

This dissertation investigates in-situ, high-resolution radar imaging of dynamic targets using an ultra-wideband (UWB) radar. Three challenging classes of dynamic targets are investigated: wind turbines, vehicles, and small consumer drones. First, the measurement and processing methodologies are developed to capture the inverse synthetic aperture radar (ISAR) image of an operating horizontal-axis wind turbine. Measurement data of a small three-blade wind turbine are collected using a UWB radar, and the measured signatures are compared to simulation results based on physical optics. The backscattering phenomenology is examined in the sinogram, spectrogram, and ISAR image domains. The same methodologies are then applied to generate the in-situ ISAR imagery of an 18-blade windmill and a 1.7 MW utility-class wind turbine. Next, the radar signatures of a vertical-axis wind turbine are studied. Measurement and simulation are carried out for a 1.5 m tall Darrieus-type turbine model. Interpretation of the dominant backscattering mechanisms is carried out. Subsequently, the radar signatures of a 112 m tall turbine are examined using simulation. Second, wide-angle ISAR imaging of vehicles is investigated. Measurement data of moving vehicles are collected using a stationary roadside UWB radar. The generated baseline ISAR images show a clear distinction between different-sized vehicles. The images are further focused through motion

compensation using a p -norm minimization. The resulting images are well focused and correspond closely to the physical dimensions of the vehicles. Third, the ISAR imaging of small consumer drones is considered. Laboratory measurement is conducted first, where the drones are rotated on a turntable and the backscattered data are collected over a wide frequency band to form high-resolution images. The effects of frequency band, aspect, polarization, dynamic blade rotation, camera mount, and drone types are examined. Subsequently, ISAR imaging of in-flight drones, from data collected using a stationary UWB radar on the ground, is demonstrated. Finally, synthetic aperture radar (SAR) imaging using a small drone as the radar platform is explored. The entire system including a UWB radar, antennas, a camera, and a single-board computer fits on the small drone and is controlled through a Wi-Fi connection. Both the side-looking and downward-looking SAR scenarios are presented.

Table of Contents

List of Figures	xi
Chapter 1: Introduction	1
1.1 Background	1
1.2 Motivation	3
1.3 Scientific Objective and Approach	5
1.4 Organization	5
Chapter 2: Basic Radar Imaging Theory and Formulation	7
Chapter 3: ISAR Imaging of Horizontal-Axis Wind Turbines	18
3.1 Introduction	18
3.2 Methodology	20
3.2.1 Measurement	20
3.2.2 Simulation	22
3.3 Measurement and Simulation Results	23
3.3.1 Sinogram	23
3.3.2 Spectrogram	24
3.3.3 ISAR Image	27
3.3.4 360° ISAR Image	29
3.3.5 Discussion	31
3.4 Scaling to Larger Turbines	33
3.4.1 Windmill	33
3.4.2 Utility-Class Wind Turbine	39
3.4.3 Updated Measurement Setup	45
3.5 Conclusion	46
Chapter 4: ISAR Imaging of a Vertical-Axis Wind Turbine	48
4.1 Introduction	48
4.2 Measurement and Simulation Setup	49
4.3 Measurement and Simulation Results	50

4.4	Full-Size Turbine Simulation.....	56
4.5	Ground-Bounce Effects	58
4.6	360° ISAR Image.....	60
4.7	Conclusion	61
Chapter 5: Wide-Angle ISAR Imaging of Vehicles		62
5.1	Introduction.....	62
5.2	Cooperative Imaging.....	63
5.3	Non-Cooperative Imaging	67
5.4	Conclusion	72
Chapter 6: Wide-Angle ISAR Imaging of Small Consumer Drones		73
6.1	Introduction.....	73
6.2	Laboratory Measurement Setup and Post-Processing.....	74
6.3	Measurement Results: DJI Phantom 2.....	75
6.3.1	Baseline Scenario.....	75
6.3.2	Effect of Rotating Blades.....	78
6.3.3	Effects of Polarization.....	79
6.3.4	Effects of Mounted Camera	79
6.3.5	Effects of Frequency Change.....	80
6.3.6	Elevation Scan	81
6.4	Measurement Results: Larger Drones.....	82
6.5	In-Flight Measurement.....	84
6.5.1	In-Flight Measurement Setup	85
6.5.2	Image Formation	86
6.5.3	Results: Azimuth Scan	88
6.5.4	Results: Elevation Scan.....	88
6.5.5	Inspire 1 Measurement.....	91
6.6	Conclusion	91
Chapter 7: Wide-Angle SAR Imaging Using a Small Consumer Drone.....		93
7.1	Introduction.....	93

7.2	Side-Looking SAR Measurement Synopsis.....	94
7.3	Image Formation	96
7.4	Side-Looking SAR Results	97
7.5	Downward-Looking SAR Measurement Synopsis.....	101
7.6	Downward-Looking SAR Results	102
7.7	Conclusion	107
Chapter 8: Conclusion and Future Work		108
8.1	Conclusion	108
8.2	Future Work	111
Appendix: Near-Field to Far-Field Transformation		114
References.....		124

List of Figures

Fig. 2.1	Illustration of a point-scatterer model of a complex target and the associated range profile.....7	7
Fig. 2.2	GTD scattering mechanisms. (a) Surface reflection. (b) Edge diffraction. (c) Cone tip diffraction. (d) Dihedral corner reflection.8	8
Fig. 2.3	Illustration of sample forward problem.9	9
Fig. 2.4	Radar imaging illustration.....12	12
Fig. 2.5	Polar reformat illustration.13	13
Fig. 2.6	Image spot size illustration.14	14
Fig. 2.7	Image unambiguous range illustration.....16	16
Fig. 3.1	Skystream 3.7 wind turbine. (a) Measurement layout. (b) Wind turbine photo. (c) Collection setup including two dual-ridged broadband horn antennas, the Time Domain PulsON 410 radar unit, and a laptop computer. (d) Simulation model.21	21
Fig. 3.2	Skystream sinogram. (a) Measurement. (b) Simulation.24	24
Fig. 3.3	Skystream spectrogram. (a) Measurement. (b) Simulation.25	25
Fig. 3.4	(a) Positive Doppler blade flash. (b) Positive Doppler specular edge contribution. (c) Negative Doppler blade flash. (d) Negative Doppler specular edge contribution.26	26
Fig. 3.5	Skystream ISAR snapshots. (a)(c)(e)(g) Measurement. (b)(d)(f)(h) Simulation.28	28
Fig. 3.6	Skystream 360° ISAR image. (a) Measurement without motion compensation. (b) Measurement with motion compensation. (c) Simulation.30	30

Fig. 3.7	Turbine point-scatterer simulation. (a) Near field. (b) Far field.....	31
Fig. 3.8	FEKO geometrical optics simulation. (a) Model. (b) Resulting image.	32
Fig. 3.9	(a) Windmill photo. (b) Simplified simulation model.	34
Fig. 3.10	Windmill sinogram. (a) Measurement. (b) Simulation.....	35
Fig. 3.11	Windmill spectrogram. (a) Measurement. (b) Simulation.....	36
Fig. 3.12	Windmill ISAR snapshots. (a)-(e)Measurement. (f)-(j) Simulation.	37
Fig. 3.13	360° ISAR image of a windmill. (a) Measurement. (b) Simulation.	38
Fig. 3.14	Utility-class wind turbine. (a) Measurement setup. (b) Measurement at base of wind turbine. (c) Wind turbine from radar perspective. (d) Simplified simulation model.....	39
Fig. 3.15	Utility-class turbine point-scatterer simulation. (a) Near field. (b) Far field. (c) NFFFT applied to near field.....	41
Fig. 3.16	Utility-class turbine sinogram. (a) Measurement. (b) Simulation. ...	43
Fig. 3.17	Utility-class turbine spectrogram. (a) Measurement. (b) Simulation.	43
Fig. 3.18	Utility-class turbine 360° ISAR image. (a) Measurement. (b) Simulation.	44
Fig. 3.19	P440 measurement. (a) Measurement setup. (b) 360° ISAR image.	45
Fig. 4.1	Two types of wind turbines. (a) Horizontal-axis wind turbine. (b) Vertical-axis wind turbine.....	48
Fig. 4.2	Simplified Darrieus-type turbine model. (a) Measurement. (b) FEKO.	50
Fig. 4.3	Sinogram of simplified turbine model. (a) Measurement. (b) Simulation.	51

Fig. 4.4	Scattering mechanisms. (a) Blade returns. (b) Tower and strut returns.	52
Fig. 4.5	Spectrogram of the simplified turbine model. (a) Measurement. (b) Far- field simulation. (c) Near-field simulation.....	53
Fig. 4.6	ISAR snapshots of the simplified turbine model. (a)-(d) Measurement. (e)-(h) Simulation.....	55
Fig. 4.7	Full-size turbine spectrogram. (a) VAWT 1.5 GHz. (b) VAWT 3 GHz. (c) HAWT 1.5 GHz. (d) HAWT 3 GHz.	57
Fig. 4.8	Vertical-axis wind turbine with ground bounce. (a) Direct path. (b) Two single-bounce paths. (c) Double-bounce path.....	59
Fig. 4.9	Spectrogram of the full-size turbine with ground at 1.5 GHz. (a) Direct path and double-bounce contributions. (b) Two single-bounce contributions. (c) Sum of all four contributions.....	60
Fig. 4.10	(a) Full-size VAWT 360° ISAR image. (b) Associated regions.....	61
Fig. 5.1	Vehicle cooperative measurement synopsis. (a) Measurement scenario and collection setup. (b) Test vehicles.....	64
Fig. 5.2	Vehicle cooperative measurement. (a) Measured range profiles. (b) k - space data.....	65
Fig. 5.3	Baseline images. (a) SUV. (b) Sedan. (c) Truck. (d) Subcompact...65	
Fig. 5.4	Focused images. (a) SUV. (b) Sedan. (c) Truck. (d) Subcompact...67	
Fig. 5.5	Vehicle non-cooperative measurement synopsis. (a) Measurement collection setup. (b) Test vehicle.	68
Fig. 5.6	Vehicle non-cooperative range alignment. (a) Raw range profile. (b) Aligned range profile.....	68

Fig. 5.7	Vehicle non-cooperative final images. (a) After coarse motion compensation. (b) After fine motion compensation.	69
Fig. 5.8	Wide-angle ISAR imaging of different vehicles. (a) Subcompact photo. (b) Subcompact ISAR image. (c) Mid-size sedan photo. (d) Mid-size sedan ISAR image. (e) Large truck photo. (f) Large truck ISAR image.	71
Fig. 6.1	(a) Drone ISAR collection setup. (b) DJI Phantom 2 with GoPro camera [84].	75
Fig. 6.2	DJI Phantom 2 baseline scenario. (a) Sinogram. (b)-(f) ISAR image at 8° , 45° , 90° , 135° , 172° respectively.	77
Fig. 6.3	Effect of rotating blades. (a) Baseline scenario (static blades). (b) Rotating blades scenario.	78
Fig. 6.4	Effects of horizontal polarization. (a) Baseline scenario (vertical polarization). (b) Horizontal polarization scenario.	79
Fig. 6.5	Effects of a mounted camera. (a) Baseline scenario (no camera). (b) Mounted camera scenario.	80
Fig. 6.6	Effects of frequency change. (a) Baseline scenario (12-15 GHz). (b) 3-6 GHz scenario.	81
Fig. 6.7	Elevation scan. (a) ISAR image centered at -90° elevation. (b) ISAR image centered at 0° elevation.	81
Fig. 6.8	(a) 3DR Solo [86]. (b) Solo ISAR image at 90° (12-15 GHz). (c) Solo ISAR image at 90° (3-6 GHz). (d) DJI Inspire 1 [87]. (e) Inspire 1 ISAR image at 270° (12-15 GHz). (f) Inspire 1 ISAR image at 270° (3-6 GHz).	83
Fig. 6.9	Drone in-flight measurement setup.	85

Fig. 6.10	Drone in-flight range profiles. (a) Before coarse motion compensation. (b) After coarse motion compensation.....	86
Fig. 6.11	Drone in-flight spectrogram (a) Before fine motion compensation. (b) After fine motion compensation.	87
Fig. 6.12	In-flight ISAR images: azimuth scan. (a)-(c) Blind motion compensation. (d)-(f) GPS-assisted motion compensation.....	89
Fig. 6.13	In-flight ISAR images: elevation scan. (a)(b) Blind motion compensation. (c)(d) GPS-assisted motion compensation.....	90
Fig. 6.14	In-flight ISAR images of Inspire 1. (a) $AZ = 270^\circ$. (b) $AZ = 262^\circ$. .	91
Fig. 7.1	Drone-SAR system and measurement setup.....	94
Fig. 7.2	Drone-SAR system on the Phantom 2 drone. (a) Top-down view. (b) Belly-up view.....	95
Fig. 7.3	Helix antenna measurement. (a) Reflection coefficient. (b) Gain. ...	95
Fig. 7.4	Drone-SAR measurement scene with 4 trihedrals.....	96
Fig. 7.5	(a) Measured range profiles vs. flight time from 4 trihedrals on the ground collected from the drone-SAR. (b) Simulated range profiles based on a point-scatterer model and constant velocity flight. (c) Aligned measured range profiles. (d) Aligned simulated range profiles.....	97
Fig. 7.6	(a) Simulated SAR image. (b) Measured SAR image with drone on rail. (c) Measured drone-SAR image.	98
Fig. 7.7	Measurement scenario for near-field backprojection.	99
Fig. 7.8	SAR images after near-field backprojection. (a) Simulated. (b) Rail-SAR. (c) Drone-SAR.	100

Fig. 7.9	Drone-SAR image of a vehicle. (a) Photo of orientation 1. (b) SAR image of orientation 1. (c) Photo of orientation 2. (d) SAR image of orientation 2.	101
Fig. 7.10	Drone measurement system and setup.....	102
Fig. 7.11	Measurement of trees. (a) Photograph. (b) Range profiles.....	104
Fig. 7.12	Measurement of vehicles. (a) Photograph. (b) Range profiles.	105
Fig. 7.13	Measurement of humans. (a) Photograph. (b) Range profiles.....	106
Fig. A.1	Problem geometry for planar Huygens' surface with a single point scatterer.....	115
Fig. A.2	Problem geometry for planar aperture under the monostatic scenario.	118
Fig. A.3	Problem geometry for circular Huygens' surface with a single point scatterer.....	119
Fig. A.4	Problem geometry for circular aperture under the monostatic scenario.	121

Chapter 1: Introduction

1.1 BACKGROUND

Microwave radar is an active sensor that transmits microwave energy and detects the reflected microwave signal from a scene to gather information about the scene. Since microwave can penetrate through clouds and work in the dark, microwave radar can operate 24-7 in all-weather conditions. A typical pulse radar transmits and receives short-duration pulses in order to collect reflectivity data of the scene as a function of pulse travel time, which is proportional to the distance (or range) of various scatterers in the scene from the radar. The resulting reflectivity data as a function of range is called a range profile. The range resolution in distinguishing the various scatterers in a range profile is determined by $\Delta r = c/2F$, where c is the speed of light and F is the equivalent bandwidth of the pulse. For example, if the equivalent bandwidth of the radar pulse is 0.5 GHz, $\Delta r = 0.3$ m. The range profile is only a one-dimensional image. To form a two-dimensional (2-D) image of the scene, similar to what an optical system is capable of generating, a radar must utilize an antenna with a narrow beam. For example, in a side-looking airborne radar (SLAR), an aircraft-mounted antenna is pointed perpendicular to the flight path and it transmits and receives a series of pulses. The resulting radar image, formed using the real-aperture antenna, has an azimuthal (or cross-range) resolution determined by the beamwidth of the antenna as $\Delta cr = r \times \text{beamwidth}$, where r is the range. For example, using an antenna with a 1° beamwidth, $\Delta cr = 167$ m for targets located 10 km away from the radar. Since the beamwidth of an antenna is inversely proportional to the electrical size of the aperture, the cross-range resolution is inversely proportional to the size of the antenna aperture. Therefore, to achieve fine cross-range

resolution in a radar image, an electrically large antenna is needed, which is often difficult to realize in practice in the microwave frequency range.

The synthetic aperture radar (SAR) imaging concept was invented in the early 1950s for airborne radar to provide enhanced azimuth resolution without the need for a large physical aperture [1-4]. By collecting and coherently processing a series of pulses from a moving aircraft (where each return pulse corresponds to the range profile from a different aspect of the scene being imaged), a synthetic aperture is formed that effectively narrows the beamwidth. It can be shown that the cross-range resolution is approximately related to the size of the synthetic aperture as $\Delta cr = \lambda_c/2\Phi$, where λ_c is the center frequency of the pulse and Φ is the angular swath of the collection. The basic assumption in forming a SAR image is that the aircraft moves in a straight line at a constant velocity. However, in practical data collection, the aircraft motion may deviate from this assumption. In order to form a focused image, a motion compensation (or auto-focusing) algorithm is often applied with the aid of known motion data of the aircraft collected using on-board instruments [2, 3, 5, 6].

The typical SAR imaging scenario entails a moving radar and stationary targets in a scene, where different aspects of the target reflectivity are collected through movement of the radar. However, it is also possible to take advantage of the motion of a moving target with respect to a stationary radar to generate a radar image of the target. In this case, different aspects of the target reflectivity are collected through the motion (in particular, the rotation) of the target. The inverse synthetic aperture radar (ISAR) concept was introduced in the early 1980s [7, 8] for the imaging scenario with a moving target and a stationary radar. The imaging principles are the same as SAR—oftentimes ISAR is said to be equivalent to the spotlight SAR scenario [2]. The range and cross-range resolution equations are the same, except Θ is now the angular swath due to the target

rotation. A significant complication with ISAR is that blind motion compensation is needed to form a focused image since the motion of the target is generally not known. Sophisticated motion compensation algorithms must be applied to form a focused image [5, 7-13]. Usually, these algorithms are based on some motion model (for both translation and rotation) with unknown parameters. The assumption that one or more prominent point scatterers on the target are visible throughout the image collection interval is then made to determine the motion parameters from the data and generate a focused image.

1.2 MOTIVATION

While radar imaging techniques (SAR and ISAR) are well established, recent advances in radio-frequency integrated circuits (RFICs) are having a significant impact on reducing the size and weight of radar components, therefore expanding radar imaging beyond purely military applications. One particularly interesting area is the development of commercial ultra-wideband (UWB) technology. In 2002, the Federal Communications Commission (FCC) allocated spectrum for the commercial usage of low-power UWB technologies for communications and sensing [14]. Since then, commercial UWB devices have become popular. One of the great appeals of UWB devices for radar applications is that they can provide high-resolution range information due to the wide bandwidth (at the centimeter level). The design of receiver architecture has been improved to deal with the wide instantaneous bandwidth. The conventional heterodyne receiver design requires a broadband analog-to-digital converter (ADC) to cover the wide bandwidth of the pulse. An ADC of this nature would typically have heavy power consumption and limited number of bits. Thus, different sampling schemes have been proposed such as subsampling [15] and equivalent time sampling [16-18]. A low power realization is

implemented by the Time Domain Corporation in their commercial UWB transceivers, of which the latest generation is the PulsON 410 (P410) [19]. The P410 emits short pulses at a pulse repetition frequency (PRF) of 10 MHz with an equivalent frequency bandwidth from 3.1 to 5.3 GHz centered at 4.3 GHz. The pulse shape was engineered to be compatible with FCC regulations. Furthermore, the pulses are pseudo-random coded to overcome the 15 m maximum unambiguous range (due to the 10 MHz PRF) and improve the signal-to-noise ratio (SNR). Overall, the P410 is a low-cost platform with low power consumption (4-9 hours of continuous operation on its 35 Wh battery pack), high portability (contained on a single 3" x 3.15" board), and a convenient universal serial bus (USB) interface. It represents the latest state-of-the-art in UWB transceiver technology. More importantly, this instrument opens up many new possibilities of portable, in-situ radar measurements, which were prohibitive in the past.

By having a large pulse bandwidth, UWB transceivers can provide high-resolution range information. However, in order to obtain equally high-resolution in cross-range, the physical or synthetic collection aperture must also be increased. For physical apertures, the use of 1-D arrays combined with UWB radars for high-resolution imaging has been investigated in the context of through-wall imaging [20-25]. Advanced signal processing algorithms such as MUSIC or RELAX have also been applied to further reduce the physical size of antenna arrays [26-28]. For synthetic aperture imaging, some previous works on generating high-resolution SAR images [25, 29] and ISAR images [30] have been reported in the literature. However, they are laboratory measurements where the synthetic collection aperture is increased on well-controlled rails or turntables. The use of UWB radars for in-situ synthetic aperture collection is largely unexplored and warrants further investigation.

1.3 SCIENTIFIC OBJECTIVE AND APPROACH

The objective of this dissertation is to investigate and demonstrate the use of a portable UWB radar system to achieve in-situ, high-resolution radar imaging of moving targets. The scientific question we set out to address is the following. Since UWB radar provides high range resolution, can an equally high cross-range resolution be obtained through an increased synthetic aperture for in-situ data collection? Only if this is realizable will a high-resolution, two-dimensional image result, thus fulfilling the true potential of UWB imaging. Under realistic conditions, either the radar platform (as in SAR) or the target (as in ISAR) can deviate significantly from the highly idealized motions assumed in the motion compensation model, making the motion compensation task much more challenging. In particular, three challenging classes of moving targets will be investigated — wind turbines, vehicles, and small drones. The unique dynamic radar signatures of these targets will be investigated and exploited to facilitate radar image processing and image interpretation. To achieve this objective, the following approach is implemented: (1) develop measurement and simulation methodologies for moving targets, (2) collect in-situ data using a UWB radar, (3) develop and implement motion compensation and image formation algorithms to form high-resolution radar images, (4) compare and validate images from measurement and simulation data, and (5) interpret the resulting radar images and investigate the scattering phenomenology.

1.4 ORGANIZATION

This dissertation is organized as follows. In Chapter 2, we introduce the basic radar imaging theory that is used throughout this dissertation. In Chapter 3, we discuss the ISAR imaging of wind turbines. The interaction between wind farms and radar waves is a topic of current interest [31-47]. The time-varying radar scattering from the rotating

blades of a wind turbine creates Doppler clutter that may interfere with radar detection and tracking. Understanding the detailed radar scattering phenomenology of wind turbines is therefore an important step toward assessment and mitigation. In Chapter 4, we investigate vertical-axis wind turbines. Recently, the US Department of Energy is considering vertical-axis wind turbines as a candidate for off-shore wind power generation [48]. Some of the potential advantages of a vertical-axis wind turbine over its horizontal-axis counterpart include better scalability to large sizes and mechanical simplicity for service and maintenance. From the radar perspective, it becomes important to evaluate how the radar signatures of a vertical-axis wind turbine differ from those of the more commonly seen three-blade horizontal-axis wind turbine. In Chapter 5, we discuss the ISAR imaging of vehicles. Radar is a possible alternative to optical cameras for vehicle sensing in traffic monitoring and perimeter security applications [49-56]. SAR imaging of stationary ground vehicles from airborne sensors has already been a subject of extensive investigations in the past [49-52]. We investigate whether ISAR imaging of moving vehicles from a stationary radar may also be realized under proper conditions. In Chapter 6, we discuss the ISAR imaging of a small drone. The proliferation of small consumer drones has raised strong interest in the regulation and monitoring of these drones [57-60]. We investigate whether the vehicle imaging methodology can be extended to image a drone in flight. In Chapter 7, we discuss SAR imaging by using the small drone as a radar platform. This topic is motivated by the recent boom on the use of small drones for aerial photography. The use of these low-cost drones for radar imaging could open up some interesting potential applications in scientific, agricultural, environmental, and structural health monitoring. Finally, in Chapter 8, we provide a detailed conclusion and potential future work is discussed.

Chapter 2: Basic Radar Imaging Theory and Formulation

In this chapter, we provide the basic radar imaging theory and formulation that will be used throughout this dissertation. The goal of radar imaging is to identify the spatial location and backscattering strength of the scatterers on a target based on its radar backscattered data. We begin with the forward problem. That is, given a target, what is the radar backscattered field? A commonly used approach to model the backscattering of a target is the so-called “point-scatterer model,” or “scattering center model.” The premise of this approach is that the scattering from a complex target can be approximately modeled as scattering (or re-radiation) from highly localized scattering centers on the target. Hence, a complex target can instead be sparsely represented by a collection of discrete scatterers on the target. Fig. 2.1 illustrates an example scenario in which a complex target (an airplane) is illuminated by a distant radar. We model the target as a collection of discrete point scatterers, and the backscattered signal from the target is considered to originate from these scatterers. Fig. 2.1 also shows the associated

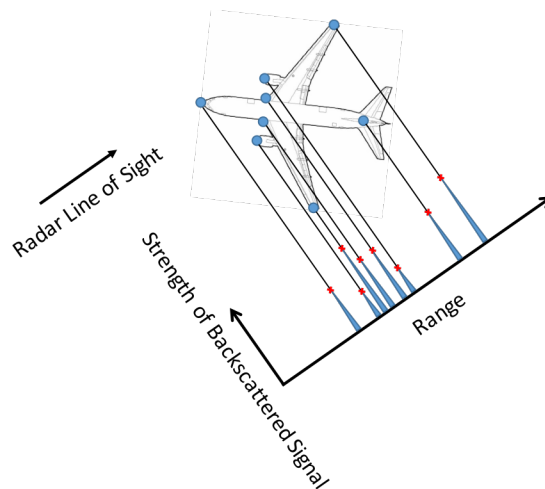


Fig. 2.1 Illustration of a point-scatterer model of a complex target and the associated range profile.

high-resolution range profile collected by the radar. In essence, the range profile is a map of the strength of the scattering centers that are located on the target along the range dimension. A range profile can therefore be considered as a “one-dimensional radar image” of the target. If we extend this concept into the cross-range dimension (i.e., the direction perpendicular to the range), a two-dimensional radar image is then a map of the strength of the scattering centers in the range and cross-range dimensions.

It should be pointed out that the point-scatterer model can be related to first-principle electromagnetic theory through high-frequency ray optics, also known as the geometrical theory of diffraction (GTD) [61, 62]. In GTD, high-frequency electromagnetic wave scattering by a target is described through reflected and diffracted rays. These rays are produced by incident rays that hit reflection or diffraction points such as specular reflections from smooth surfaces, edge diffractions from edges and tips, as well as multiple scattering from dihedral and trihedral surfaces. This is illustrated in

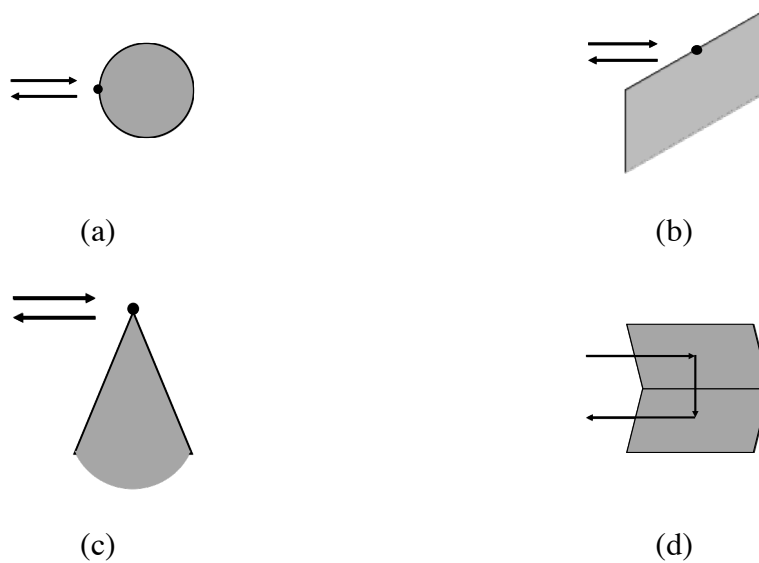


Fig. 2.2 GTD scattering mechanisms. (a) Surface reflection. (b) Edge diffraction. (c) Cone tip diffraction. (d) Dihedral corner reflection.

Fig. 2.2. These reflection or diffraction points correspond to the scattering centers in the point-scatterer model. However, while the scattering amplitudes of a limited number of canonical structures have analytical solutions, the scattering amplitude of a more general structure may not have an analytical solution. Nevertheless, the point-scatterer model is a well-accepted way to describe the scattering from a complex target.

Let us now continue with the formulation for the forward problem. Consider the scenario in Fig. 2.3, where there is a point scatterer located at (x_0, y_0) . In this scenario, the radar is located at infinity, in the third quadrant, and is operating under the monostatic scenario (the transmitter (Tx) and receiver (Rx) are collocated). Relative to a reference point scatterer located at the origin, the return from the point scatterer located at (x_0, y_0) travels an extra $2(x_0 \cos \phi + y_0 \sin \phi)$ distance from the radar. The backscattered field can then be expressed as:

$$E^s(k, \phi) = A^s e^{-j2k(x_0 \cos \phi + y_0 \sin \phi)} \quad (2.1)$$

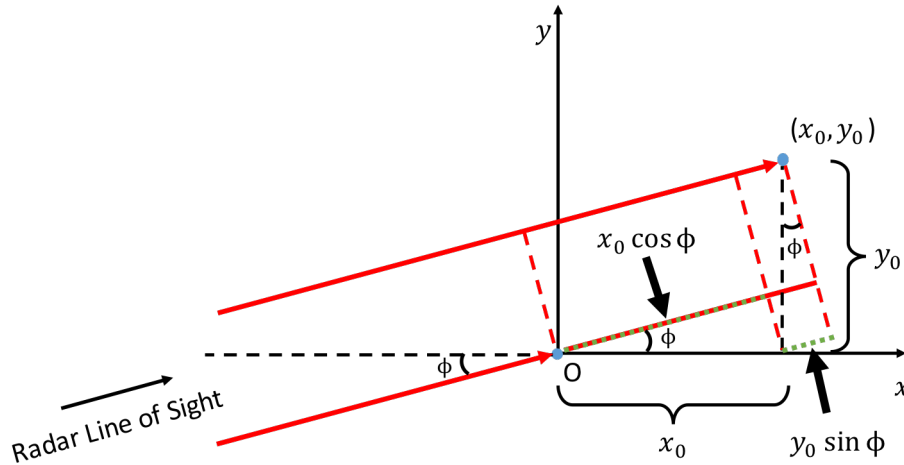


Fig. 2.3 Illustration of sample forward problem.

$$\text{where } k = \frac{2\pi}{\lambda} = \frac{2\pi f}{c} \quad (2.2)$$

E^S is the backscattered field, A^S is the amplitude of the backscattered field, ϕ is the incident angle, f is frequency, and c is the speed of light. Here, the phase of the backscattered field is relative to that from a point scatterer at the origin. Eq. (2.1) can be more conveniently rewritten as:

$$E^S(k_x, k_y) = A^S e^{-jk_x x_0} e^{-jk_y y_0} \quad (2.3)$$

$$\text{where } \begin{cases} k_x = 2k \cos \phi = \frac{4\pi f}{c} \cos \phi \\ k_y = 2k \sin \phi = \frac{4\pi f}{c} \sin \phi \end{cases} \quad (2.4)$$

Examining Eq. (2.3), we can see that the phase of the rewritten expression is linear in k_x and k_y . Note, A^S accounts for the strength of the transmitted field, the propagation loss between the target and radar, and the strength of the scatterer. Since the former two are the same for all point scatterers on the target in the far-field limit, A^S is proportional to the strength of the scatterer. Under the assumption that there is no multiple scattering between point scatterers, the expression for the scenario with multiple point scatterers in the scene simply becomes a summation of the backscattered fields from individual point scatterers:

$$E^S(k_x, k_y) = \sum_{n=1}^N A_n^S e^{-jk_x x_n} e^{-jk_y y_n} \quad (2.5)$$

This constitutes the signal model for the forward scattering problem.

Next, we examine the inverse problem (where we want to find A_n^s , x_n , and y_n from E^s). One method to solve this problem is to use a 2-dimensional (2-D) inverse Fourier transform (IFT). Recognizing that the scattered field model is a summation of exponential terms with linear phase in k_x and k_y , we can perform an inverse Fourier transform operation to extract the location information contained in the phase of the scattered field:

$$Image(x, y) = \frac{1}{(2\pi)^2} \iint_{-\infty}^{\infty} E^s(k_x, k_y) e^{jk_x x} e^{jk_y y} dk_x dk_y \quad (2.6)$$

Plugging in Eq. (2.5) into Eq. (2.6) results in:

$$\begin{aligned} Image(x, y) &= \frac{1}{(2\pi)^2} \iint_{-\infty}^{\infty} \sum_{n=1}^N A_n^s e^{jk_x(x-x_n)} e^{jk_y(y-y_n)} dk_x dk_y \\ &= \sum_{n=1}^N A_n^s \delta(x - x_n) \delta(y - y_n) \end{aligned} \quad (2.7)$$

Thus, the resulting $Image(x, y)$ is a 2-D map that will show all of the scatterers on the target at (x_n, y_n) of amplitude A_n^s . In summary, the 2-D IFT transforms the multi-frequency, multi-aspect backscattered data into a 2-D image that maps the location and backscattering amplitude of each scatterer. The forward and inversion models presented thus far based on the point-scatterer model are exceedingly simple. There are, however,

several complications that need to be addressed. First, the scattered field cannot be collected over an unbounded k_x and k_y space. This will limit the image resolution achievable in practice. Second, to reduce the computational complexity of the 2-D IFT operation, an inverse fast Fourier transform (IFFT) can be applied. These two issues will be discussed further next.

To collect data in measurement, multi-frequency data are collected at each aspect angle by varying the frequency content of the radar signal. Multi-aspect data are collected by either moving the radar around a stationary target (as in SAR) or by the rotation of the target while observing it from a stationary radar (as in ISAR). From this physical standpoint, it is common to denote x as range (or down-range) and y as cross-range. This is illustrated in Fig. 2.4.

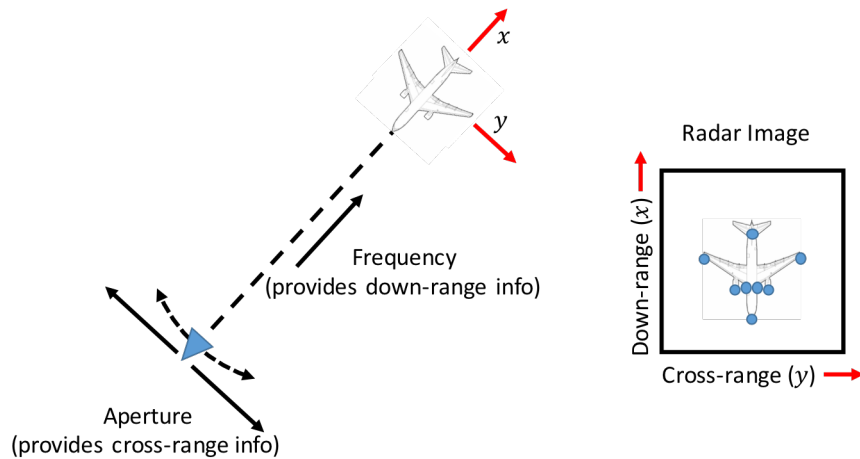


Fig. 2.4 Radar imaging illustration.

Let's consider the simple case in which data are collected uniformly in frequency and angle. From Eq. (2.4), it is clear that data collected in such a fashion would be in "polar form" in k -space, as shown in the left half of Fig. 2.5. While a brute-force 2-D IFT

can be used to generate the image from such data, the complexity is $O(N^4)$ due to $N_f \times N_\phi$ operations for each of the $N_x \times N_y$ points in the image. A 2-D IFFT would reduce the complexity to $O(N^2 \log^2 N)$. However, a 2-D IFFT would require the data to be uniform in k_x and k_y . One solution is to perform a polar-to-rectangular reformatting (or “polar reformatting”) of the data. In other words, the data on the uniform k_x - k_y grid are interpolated from the data that are collected uniformly in frequency and angle. This can be done using, for example, a bilinear interpolation [63]. Fig. 2.5 illustrates the polar reformatting step. Subsequently, a 2-D IFFT of uniformly sampled k -space data is performed to generate the image.

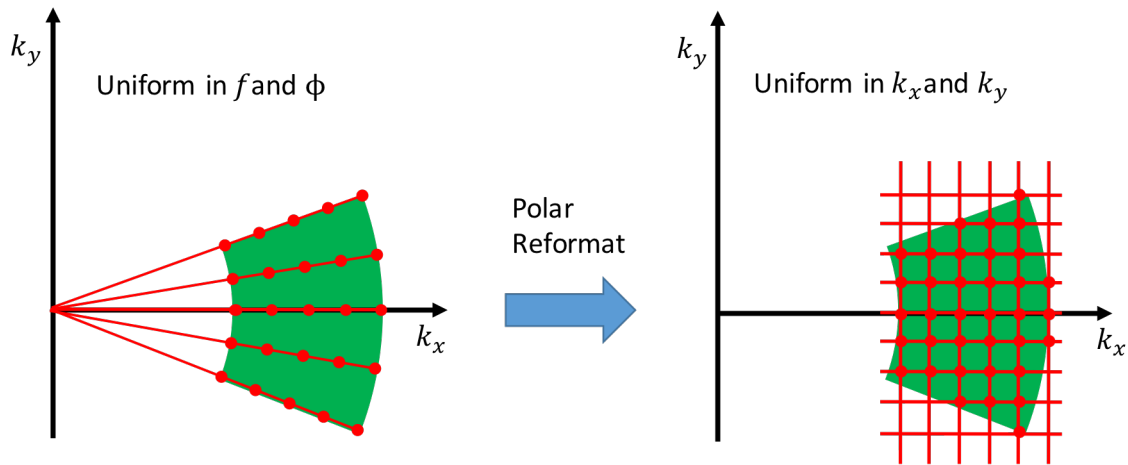


Fig. 2.5 Polar reformat illustration.

It is clear that the frequency bandwidth and angular bandwidth of the data collection limit the region of the accessible k -space. This in turn limits the achievable 2-D image resolution. To discuss this issue, let us consider the “narrow-band, small angle” imaging scenario (data are collected over a narrow bandwidth, F , and a narrow angular aperture, Φ). While this is an idealized case, and real data collection (including those to

be discussed in the later chapters) may deviate from this case, it is mathematically simpler to consider and provides some useful, approximate guidelines in the collection requirements. We make the following approximations as shown in Eq. (2.8):

$$k_x = \frac{4\pi f}{c} \cos \phi \cong \frac{4\pi f}{c}$$

$$k_y = \frac{4\pi f}{c} \sin \phi \cong \frac{4\pi f_c}{c} \phi$$
(2.8)

where f_c is the center frequency of the data. After making such approximations, we notice that the frequency and angle terms are now decoupled in the phase (k_x is only dependent on f , and k_y is only dependent on ϕ). The resulting approximation leads to the geometrical construct in the left half of Fig. 2.6. Under this approximation, data that are collected uniformly in f and ϕ are sampled uniformly on a rectangular grid in k_x and k_y . Since the data are already uniform in k_x and k_y , the image can simply be generated through a 2-D IFFT of the data collected uniformly in frequency and angle without polar reformatting.

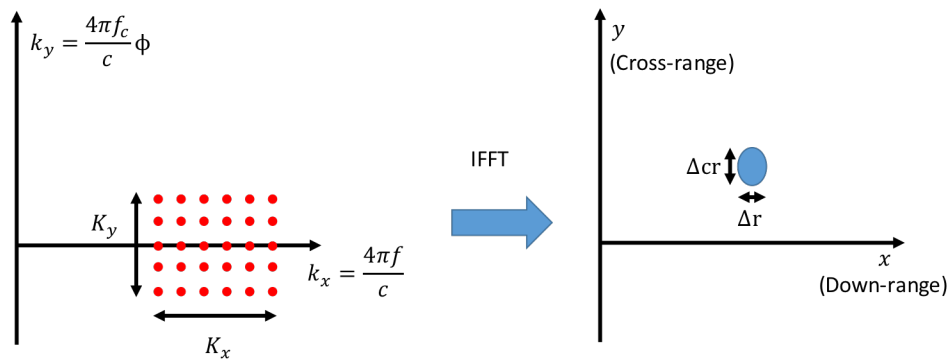


Fig. 2.6 Image spot size illustration.

Under this approximation and using standard Fourier transform analysis, we can find the expressions for the spot size of the “point spread response” in the image. The down-range resolution is inversely proportional to the extent of the data in k_x , which we denote as K_x . Similarly, the cross-range resolution is inversely proportional to the extent of the data in k_y , which we denote as K_y . This is illustrated in Fig. 2.6. The expressions for the range and cross-range resolution can then be derived easily and are given by Eq. (2.9). These are exactly the same expressions that were given in Chapter 1. Again, we can see that the range resolution is inversely proportional to the frequency bandwidth. Thus, the wider the bandwidth, the finer the range resolution. The cross-range resolution is inversely proportional to the angular swath of collection with a proportionality constant that is half the wavelength at the center frequency of the radar. Thus, the larger the collection aperture and higher the collection frequency, the finer the cross-range resolution.

$$\Delta r = \Delta x = \frac{2\pi}{K_x} = \frac{2\pi c}{4\pi F} = \frac{c}{2F}$$

$$\Delta cr = \Delta y = \frac{2\pi}{K_y} = \frac{2\pi c}{4\pi f_c \Phi} = \frac{\lambda_c}{2\Phi}$$
(2.9)

In addition to the down-range and cross-range resolutions, it is also important to take into consideration the maximum unambiguous down-range and cross-range windows as a result of the uniform sampling in the k -space. Based on Fourier analysis, the maximum unambiguous windows in range and cross-range are determined respectively by the frequency and angular sampling densities. Expressions for the maximum unambiguous down-range and cross-range are given in Eq. (2.10):

$$X = R = \frac{2\pi}{\Delta k_x} = \frac{c}{2\Delta f}$$

$$Y = CR = \frac{2\pi}{\Delta k_y} = \frac{\lambda_c}{2\Delta\phi}$$
(2.10)

They are very similar to the resolution expressions in Eq. (2.9), except that the frequency and angular extents are replaced by the frequency and angular sampling steps. An illustration of the relationships is shown in Fig. 2.7. The dashed-red box in Fig. 2.7(b) shows the maximum unambiguous image window. A window that is smaller than the target would result in aliasing in the image.

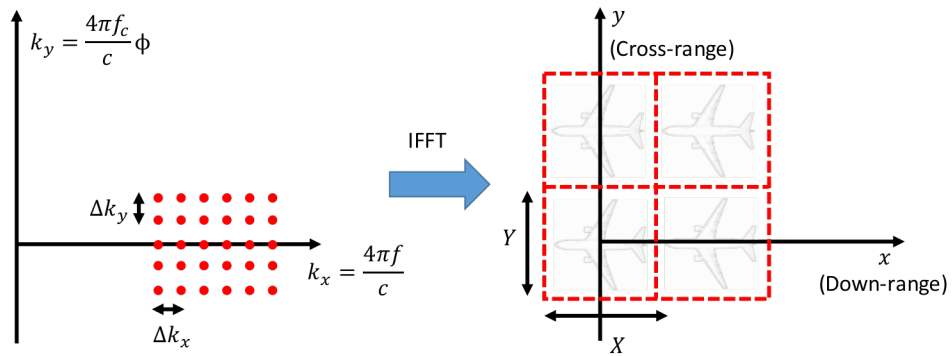


Fig. 2.7 Image unambiguous range illustration.

In this chapter, we have provided the framework for the radar imaging that will be used throughout this dissertation. It is established that both SAR and ISAR imaging require multi-frequency, multi-aspect data of the target to be collected. The formulation described in this chapter is known as “ k -space” imaging, where a 2-D IFT transforms the k -space data into a 2-D image of the target. In order to achieve high resolution in the 2-D image, both a wide bandwidth and angular swath are needed. In addition, sufficiently

dense sampling is needed in both frequency and angle in order to ensure that the final resulting image is not aliased. Lastly, in practice, the measurement scenario may not fit this highly idealized model. For example, the angular sampling in measurement will typically not be uniform. In ISAR scenarios, the angle at which the data are collected is not even known. The solutions to these non-idealities are discussed and implemented as they arise in the subsequent chapters.

Chapter 3: ISAR Imaging of Horizontal-Axis Wind Turbines^{1,2,3}

3.1 INTRODUCTION

Due to the growing demand for wind energy, the number of wind farms has been increasing rapidly worldwide. As a result, the interference of wind farms on radar operations has been a problem of growing concern for the radar community [31-34]. The large electrical size of utility-class wind turbines gives rise to significant radar clutter. In particular, the time-varying radar scattering from the rotating blades of a wind turbine creates Doppler clutter that may interfere with moving target detection and tracking. Understanding the detailed radar scattering phenomenology of wind turbines is therefore an important step toward assessment and mitigation. Significant efforts have been devoted in the electromagnetics community to simulating, measuring, and analyzing the radar signatures of wind turbines [35-47]. To date, the most complete in-situ measurement data set was collected by the Air Force Research Laboratory in 2006 of a wind farm located in Fenner, NY [35, 36]. Data were collected at discrete frequencies in the L, S, C, and X bands. The resulting time-varying radar returns at each frequency were then processed using the short-time Fourier transform (STFT) [11] into Doppler spectrograms, which showed strong positive and negative Doppler flashes at 60° blade rotation intervals. Simulations were also conducted using high-frequency ray tracing to corroborate the measurement findings. Subsequent works [37-45] have largely followed

¹ C. J. Li, S.-T. Yang, and H. Ling, "In-situ ISAR imaging of wind turbines," *IEEE Trans. Antennas Propag.*, vol. 64, pp. 3587-3596, Aug. 2016.

² C. J. Li, S.-T. Yang, and H. Ling, "ISAR imaging of a windmill – measurement and simulation," in *Proc. European Conference on Antennas and Propagation*, The Hague, Netherlands, pp. 1-5, Apr. 2014.

³ C. J. Li and H. Ling, "On simulating the high-resolution radar image of a wind turbine," in *Proc. European Conference on Antennas and Propagation*, Davos, Switzerland, pp. 1-2, Apr. 2016.

Chenchen Jimmy Li was the primary author for all content in the above publications.

this line of investigation, i.e., focusing on the Doppler features of wind turbines at a fixed frequency.

In fact, the down-range features of a turbine as a function of time (or the so-called sinogram) could also provide useful information on turbine scattering. Surprisingly, very little attention has been paid to sinograms of wind turbines. Moreover, when the down-range and Doppler information are properly combined, a two-dimensional (2-D) radar image of the turbine can be constructed. This is the well-established ISAR imaging technique often used to examine radar signatures of complex targets [7, 8]. In the standard instrumentation ISAR scenario, the target is assumed to be under constant rotational motion—which is already present in the relatively constant rotation of wind turbine blades. Therefore, it becomes possible to collect the desired data from an operating wind turbine using a stationary radar without any additional sensor movement.

In this chapter, we set out to collect in-situ radar data over a broad frequency bandwidth from a wind turbine and construct its ISAR image. The resulting imagery can resolve the prominent scattering features in both the down-range and Doppler (or cross-range) dimensions. This in turn provides additional insights that may not be available in either the down-range or Doppler domain alone. In addition, any motion anomalies associated with the turbine blades can be captured. We demonstrate the feasibility of ISAR imaging a wind turbine in-situ and examine its scattering phenomenology in the ISAR image plane in detail. In-situ measurements are carried out using the P410 UWB radar system [19]. One of the key challenges in the measurement is to collect high-resolution range profiles at a sufficiently high sampling rate to capture the Doppler information without aliasing. To develop and validate the measurement and processing methodologies, we first examine a small Skystream wind turbine with a 3.7 m rotor diameter. The backscattered data are post-processed into sinograms, spectrograms, and

ISAR images. The unique shape of the blades is clearly revealed in the resulting ISAR imagery. Results are also compared to those based on the physical optics (PO) simulation of the turbine model computed using FEKO [64]. The backscattering phenomenology is then examined in detail. Once the measurement and simulation methodologies are established and validated on the small wind turbine, we apply the same methodologies to larger structures: a 5 m rotor diameter windmill and finally a 1.7 MW utility-class wind turbine with a rotor diameter of 100 m.

3.2 METHODOLOGY

3.2.1 Measurement

In-situ measurements are made at a local wind turbine in Georgetown, Texas using the P410 radar. Two dual-ridged broadband horns are used as transmitting and receiving antennas. Coherent pulse integration is used to improve the signal-to-noise ratio. The radar sampling rate for consecutive range profiles is set to 250 Hz. This sampling rate is upper-bounded by a number of factors including the number of range bins measured, the number of coherently integrated pulses to form a range profile, as well as the radar-to-computer data transfer rate. It must be greater than the maximum Doppler extent of the wind turbine return to coherently process the range profiles into an unaliased ISAR image.

The radar is situated on the ground with the antennas pointed up towards the turbine. The turbine from the radar perspective is approximately at a $\theta = 60^\circ$ elevation angle onto the frontal, head-on view of the wind turbine (yaw angle = 0°). Fig. 3.1(a) shows the measurement layout, Fig. 3.1(b) shows a photo of the target wind turbine at a 60° elevation angle, and Fig. 3.1(c) shows the measurement collection setup including the

two horn antennas, the P410 radar unit, and a laptop computer. The measurement distance is approximately 27 m to the hub of the wind turbine.

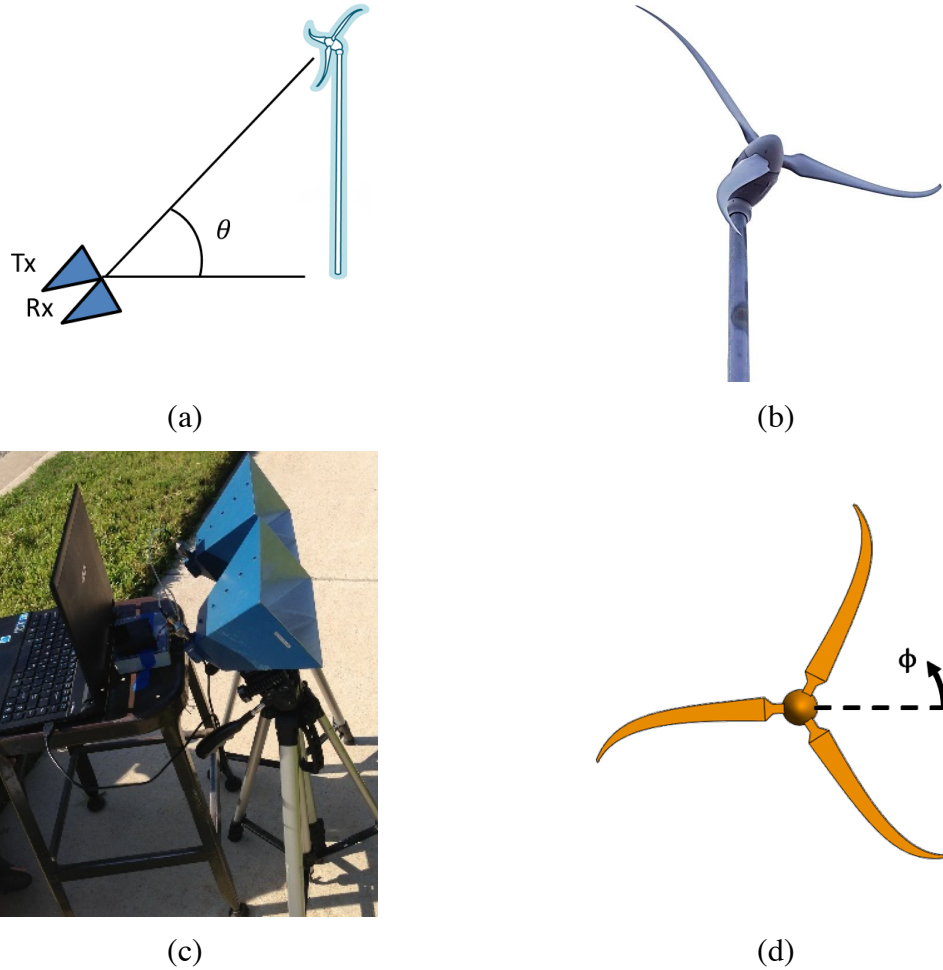


Fig. 3.1 Skystream 3.7 wind turbine. (a) Measurement layout. (b) Wind turbine photo. (c) Collection setup including two dual-ridged broadband horn antennas, the Time Domain PulsON 410 radar unit, and a laptop computer. (d) Simulation model.

The turbine rotor diameter is 3.7 m. The rotation rate was approximately 20 rpm during the collection. Taking the frontal perspective (at a $+60^\circ$ elevation angle) reduces the maximum down-range and Doppler extent of the wind turbine. The maximum down-

range extent is $(3.7 \text{ m}) * \sin(60^\circ) = 3.2 \text{ m}$, and the maximum Doppler extent can be estimated from:

$$f_{D,max} = 2 \left(\frac{2R_{rotor}\Omega}{\lambda} \right) \sin \theta \quad (3.1)$$

where R_{rotor} is the radius of the rotor, Ω is the rotation rate, λ is the wavelength, and θ is the elevation angle from the radar perspective. The extra factor of two accounts for the both the positive and negative Doppler returns from the blades. Thus, $f_{D,max}$ at 5.3 GHz is 237 Hz and our chosen 250 Hz sampling is sufficient to capture the phase variation from consecutive range profiles.

3.2.2 Simulation

A simplified computer-aided design (CAD) model of the wind turbine is created using the approximate dimensions. Only the blades and hub of the wind turbine are included, and the blades are flat with finite thickness. The thickness of each blade is tapered towards the tip. The blades and hub are assumed to be perfectly conducting. Fig. 3.1(d) shows the CAD model used in the FEKO simulation. Note that each blade has a straight portion as well as a curved portion.

The physical optics with full ray tracing (i.e. PO with shadowing) solver in FEKO is used in the simulation. Far-field conditions are assumed on both transmit and receive in the simulation. The frequency range is the same as the measurement, with 75 frequency points to provide a sufficient down-range window without aliasing. To simulate the rotating turbine blades, we rotate the blade geometry to form consecutive CAD files and carried out FEKO simulation for each file from the approximate incident angle in the measurement. The result of the simulation is the radar signature as a function of dwell

time. The required angular sampling between snapshots can be estimated as $\Delta\phi = \Omega/f_{D,max}$. Thus, to match the 250 Hz Doppler extent used in the measurement, the angular sampling should be spaced by 0.4° or less. While a full-wave solver could be used for a single rotation angle and frequency, it is not practical to solve for all the required rotation angles and frequencies due to the large amount of computation time.

3.3 MEASUREMENT AND SIMULATION RESULTS

The dynamic signatures from the measured and simulated backscattered data versus time (or blade rotation angle) are post-processed into sinograms, spectrograms, and ISAR images. Data for the vertical-vertical polarization on transmit-receive case are shown. The measured data are not calibrated in terms of absolute radar cross section (RCS) level but are instead normalized to the maximum value. Additionally, the measurement data have been motion filtered using a 4-tap finite impulse response filter during the data collection to remove stationary clutter.

3.3.1 Sinogram

The measured and simulated sinograms (i.e. range profiles versus time) are shown in Fig. 3.2. The range profile in the simulation is obtained by inverse Fourier transforming the frequency response after a Hamming window is applied. Reasonable agreement can be seen between the measurement and simulation results. There are six periodic “flashes” near zero down-range. These occur when the straight portion of the turbine blade becomes perpendicular to the radar line-of-sight (RLOS). There are two flashes per blade; one for the leading edge and one for the trailing edge a half-turn later. These flashes are focused in down-range with the leading edge flashes focused slightly below zero down-range and the trailing edge flashes focused slightly above zero down-

range. Additionally, there are six faint tilted tracks that extend beyond the flash points. These correspond to a specular return from the blade edge as the specular point travels along the curved portion of the blade as the blade continues to rotate. Finally, there is a static return from the hub near zero down-range that is seen in simulation but has been largely motion filtered out in measurement.

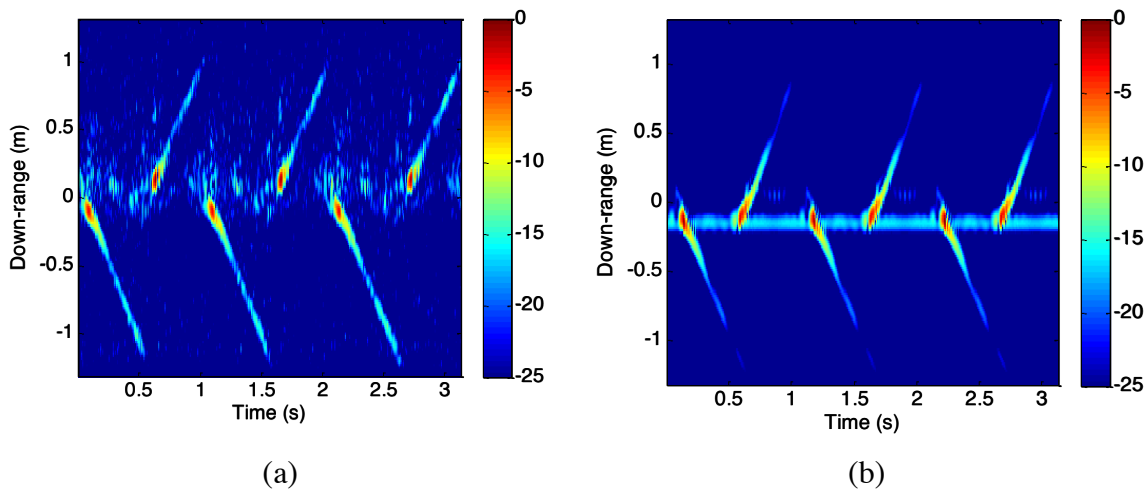


Fig. 3.2 Skystream sinogram. (a) Measurement. (b) Simulation.

3.3.2 Spectrogram

There has been extensive past work on wind turbine Doppler analysis [35-46]. Here, we extract the spectrogram based on the time-domain returns of the UWB radar. By Fourier transforming the measured range profiles from the P410 radar, we obtain the corresponding complex frequency response. The time-varying Doppler behavior of the target can then be examined at a single frequency. Using a STFT along the time axis, we obtain the Doppler frequency versus time plot (or the Doppler spectrogram) at 4.3 GHz. Fig. 3.3 shows the spectrograms obtained using the STFT with a 172 ms Hamming

window, which corresponds to a 20° angular swath. Each spectrogram shows three positive and negative Doppler tracks. The positive Doppler tracks correspond to the leading edge of the blade rotating towards the radar while the negative Doppler tracks correspond to the trailing edge of the blade rotating away from the radar.

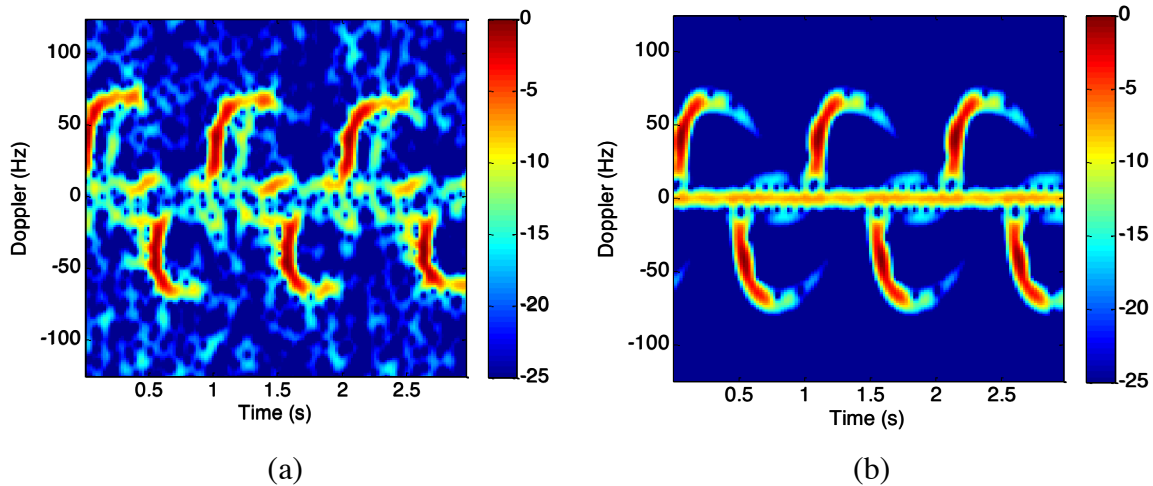


Fig. 3.3 Skystream spectrogram. (a) Measurement. (b) Simulation.

Each track has a straight portion and a curved portion due to the blade shape. The straight vertical portion of the Doppler track, or the Doppler flash, occurs when the straight portion of the blade becomes perpendicular to the RLOS. At this instance, each radial component on the straight portion of the blade lights up in its respective Doppler bin. This is illustrated in Figs. 3.4(a) and 3.4(b). As the blade continues to rotate, the dominant contribution moves to the curved portion of the blade and the return becomes specular (lengthwise). Since the specular point travels towards the tip of the blade as the turbine continues to rotate, it is expected that the Doppler extent would continue to increase—which is seen initially. However, as the turbine continues to rotate, the Doppler extent starts to decrease. This is illustrated in Fig. 3.4(c) where the dashed line represents the tangential motion of the blade and the solid line represents the component that is

parallel to the RLOS. Finally, the static return from the hub of the turbine is seen in simulation but was motion filtered out in measurement. Overall, the qualitative agreement between the two is good, and the Doppler behaviors correspond closely to the scattering mechanisms described in Fig. 3.4.

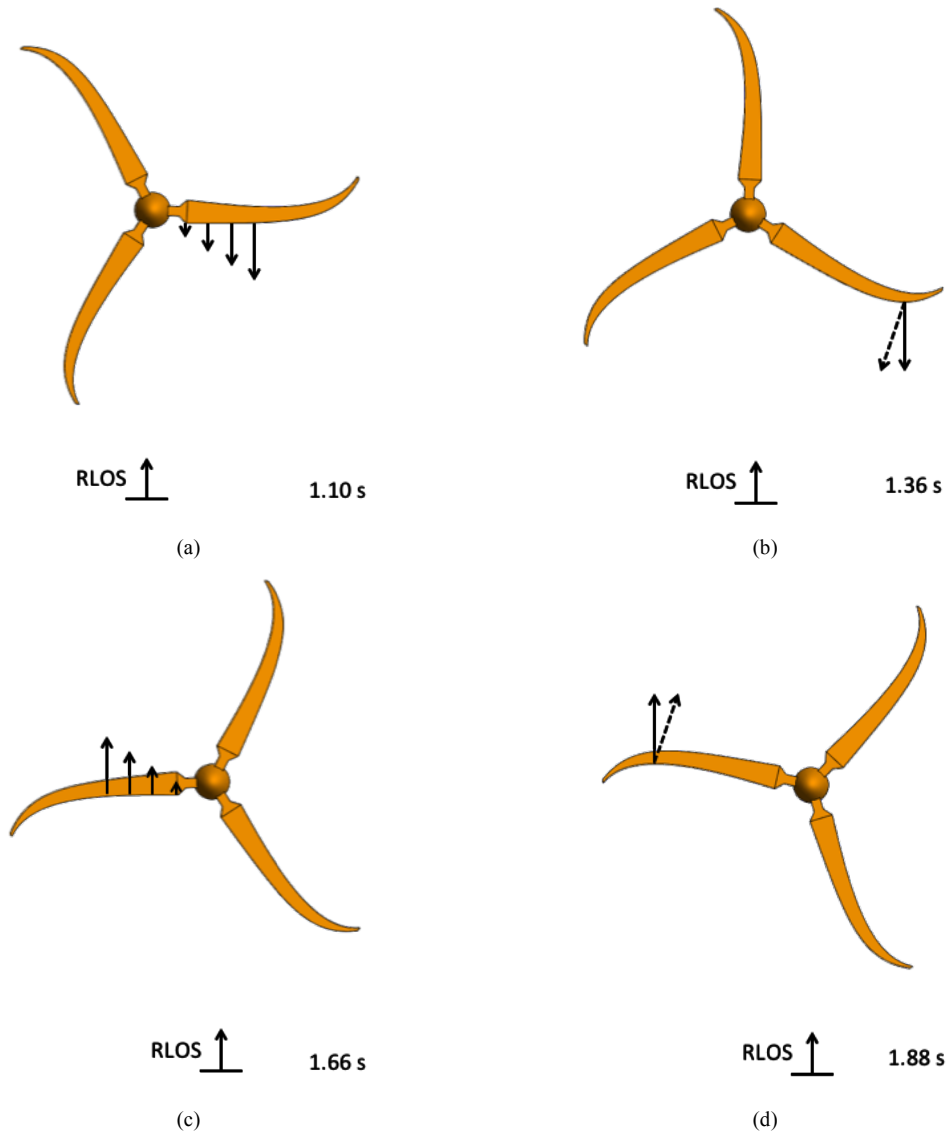


Fig. 3.4 (a) Positive Doppler blade flash. (b) Positive Doppler specular edge contribution. (c) Negative Doppler blade flash. (d) Negative Doppler specular edge contribution.

3.3.3 ISAR Image

Although discussed in the previous chapter, we briefly revisit these expressions in the context of wind turbine imaging. By processing the frequency response versus time data using a 2-D inverse Fourier transform, we can generate a 2-D ISAR image of the wind turbine [5]. If we assume a known constant rotation rate, the ISAR image can be displayed as a down-range vs. cross-range plot. This is illustrated in the following formulation (these expressions were also given in Chapter 2):

$$Image(r, cr) = \iint E^s(f, \phi) e^{jk_x r} e^{jk_y cr} dk_x dk_y \quad (3.2)$$

$$\text{where } \begin{cases} k_x = \frac{4\pi f}{c} \cos \phi \\ k_y = \frac{4\pi f}{c} \sin \phi \end{cases} \quad (3.3)$$

In the above expression, r is the down-range (along the RLOS), cr is the cross-range (perpendicular to the RLOS), f is the frequency, ϕ is the rotation angle of the turbine blades, E^s is the backscattered field as a function of frequency and angle, and c is the speed of light. For measurement, the angle is linearly proportional to the collection time through the angular rotation rate Ω .

We use an angular swath of 20° to generate ISAR snapshots of the wind turbine in both simulation and measurement. As we slide the 20° angular swath along the angular (or time) axis, the following sequence of events can be seen for each blade. First is the blade flash of the leading edge of the blade (Figs. 3.5(a) and 3.5(b)). This is followed by the specular point traveling along the curved portion of the blade towards the tip (Figs. 3.5(c) and 3.5(d)). Next is the blade flash from the trailing edge of the blade a half turn

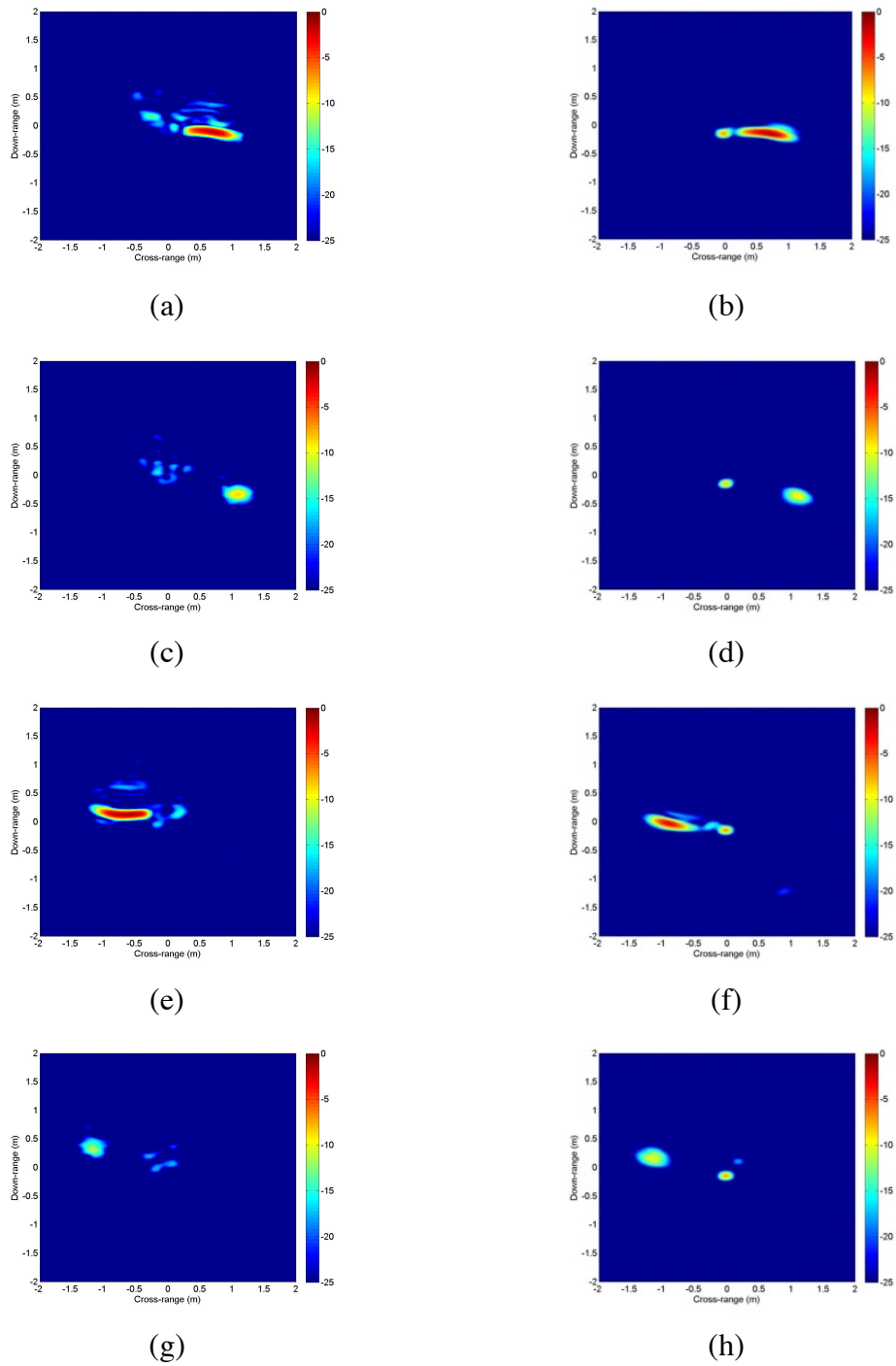


Fig. 3.5 Skystream ISAR snapshots. (a)(c)(e)(g) Measurement. (b)(d)(f)(h) Simulation.

later (Figs. 3.5(e) and 3.5(f)). This is followed by the specular point traveling along the curved portion of the blade (Figs. 3.5(g) and 3.5(h)). This sequence is easily seen in a movie made of many consecutive ISAR frames. The ISAR movies can be found online [65]. Here, we have shown several snapshots that highlight this sequence in Fig. 3.5. The measurement data are presented on the left and the simulated data on the right. There is a steady return near zero down-range and cross-range that is present in simulation but largely absent in the measurement. This corresponds to the static hub return that is motion filtered out in measurement.

3.3.4 360° ISAR Image

While the ISAR images already reveal the key target features, it is also possible to obtain a “complete image” of the wind turbine. This is done using the same formulation as Eq. (3.2) but the data from a full revolution is interpolated onto a uniform k_x - k_y grid using a bilinear interpolation scheme. A 2-D inverse fast Fourier transform is then applied over the entire k -space to generate the wide-angle, 360° ISAR image.

Fig. 3.6(a) shows the resulting 360° ISAR image. A three-blade wind turbine is visible, but the leading edge and trailing edge of each blade have coalesced. This is clear when we compare Fig. 3.6(a) to the simulated results in Fig. 3.6(c), which shows distinct leading and trailing edge features on each blade. Motion compensation is applied to improve the quality of the final image. The necessary non-uniform rotation information in the measurement can be estimated from the sinogram and/or spectrogram. Based on the geometry of the turbine, it can be inferred that there are 120° of rotation between each leading edge flash and the same applies for the trailing edge flashes. This facilitates the modeling of the turbine rotation motion. It was found that a piecewise linear motion model was sufficient. Motion compensation is implemented by extracting the time bins of

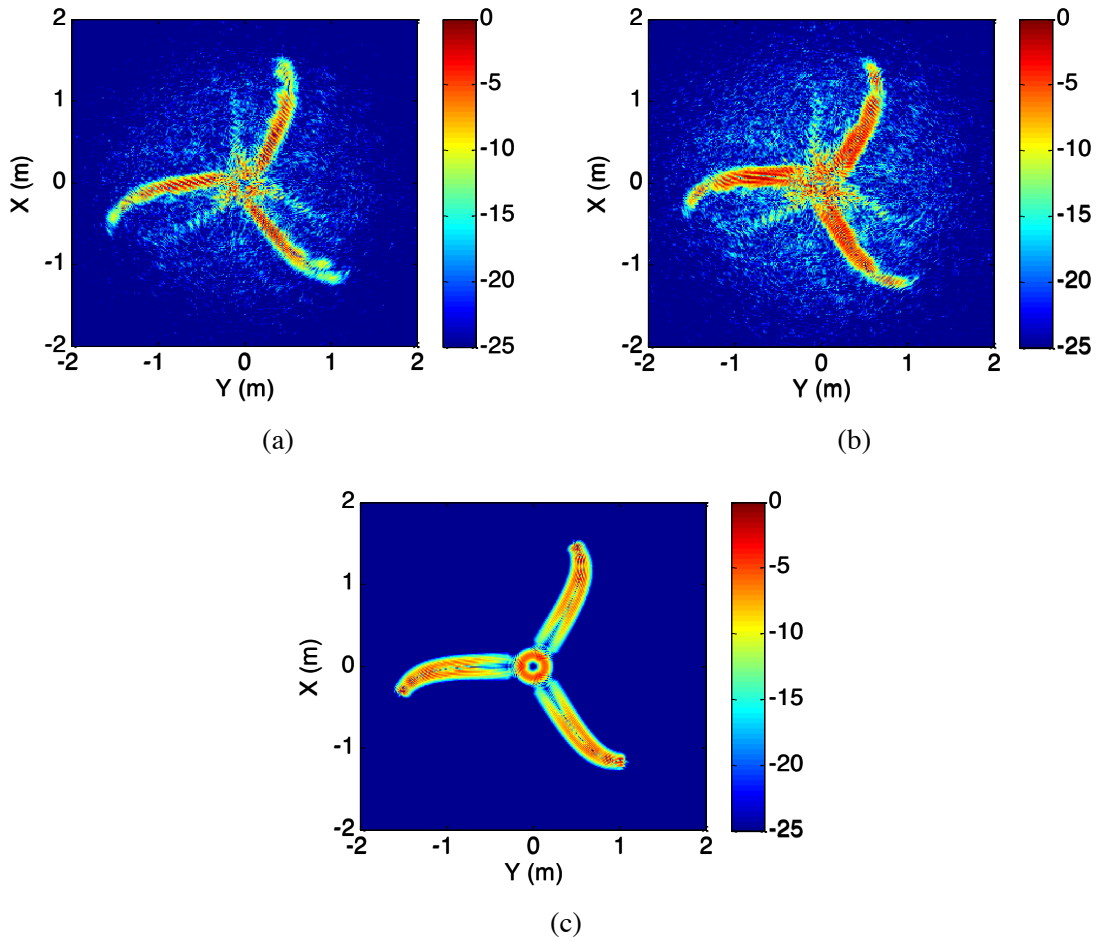


Fig. 3.6 Skystream 360° ISAR image. (a) Measurement without motion compensation. (b) Measurement with motion compensation. (c) Simulation.

the three leading edge blade flashes in the sinogram. These time bins are assigned to 0° , 120° , and 240° respectively. The remaining time bins are then assumed to be equally spaced within the 120° interval. After applying motion compensation to the measured data, better agreement can be seen between the measured image (Fig. 3.6(b)) and the simulated image (Fig. 3.6(c)). In addition to distinctly capturing the outline of the turbine, both the leading and trailing edge of each turbine blade are now distinct. The hub cannot be seen clearly in the measurement image due to the motion filter.

3.3.5 Discussion

Some of the intricacies in the image formation process are discussed. First, the far-field distance of the wind turbine using the standard $2D^2/\lambda$ formula gives a distance far greater than the distance in measurement. To assess near-field effects on the ISAR images, a point-scatterer study is carried out. Here, points on a single curve are used to model each turbine blade and simulated radar data are generated based on the point scatterer model. Using the same far-field ISAR imaging algorithm, we compare the images generated from simulated near-field data at a 27 m distance to those generated from simulated far-field data. Fig. 3.7(a) shows the former image, and Fig. 3.7(b) shows the latter image. The two images are not significantly different, with only a minor “splitting” effect towards the tips of the blades in the former image. Should near-field effects become prominent, a near-field to far-field correction may be required to maintain the correct geometrical shape in the ISAR image. This issue will be discussed later in Sec. 3.4.2.

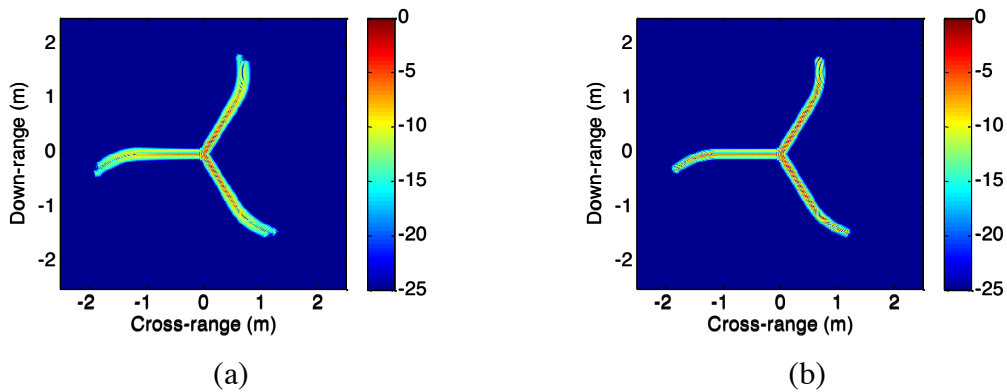


Fig. 3.7 Turbine point-scatterer simulation. (a) Near field. (b) Far field.

Second, there are some faint features seen in the measurement spectrogram and image, but not in simulation. In particular, there are three faint vertical lines in the positive Doppler portion of Fig. 3.3(a). Similarly, there are three corresponding faint lines in the Fig. 3.6(b). We postulate that these are due to multi-bounce effects between the turbine, nacelle, and tower. FEKO geometrical optics simulation (based on the shooting and bouncing ray technique [66]), using a maximum of three ray interactions, was carried out with the inclusion of the tower and nacelle. Fig. 3.8(a) shows the simulation model, and Fig. 3.8(b) shows the resulting image (a motion filter is applied to remove the strong static returns). Additional faint radial features, similar to those found in measurement, are observed.

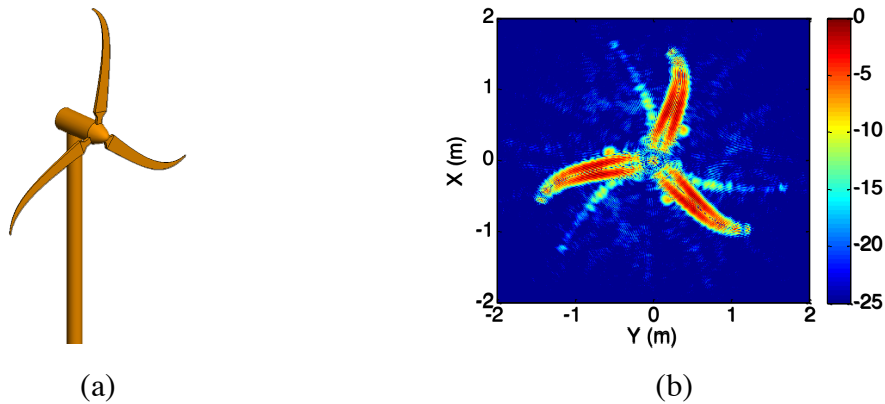


Fig. 3.8 FEKO geometrical optics simulation. (a) Model. (b) Resulting image.

In summary, we have established the measurement and processing techniques necessary to obtain the ISAR image of a wind turbine in-situ. We have also shown that the resulting ISAR image provides detailed information about the scattering phenomenology of the turbine in relation to its geometrical shape.

3.4 SCALING TO LARGER TURBINES

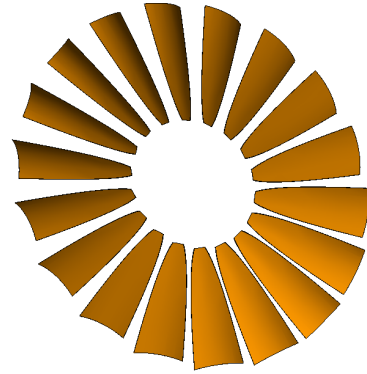
The same methodology can be applied to other wind turbines. However, as the turbine rotor diameter increases, both the maximum down-range extent and Doppler extent of the turbine increase. This poses a significant challenge for measurement since the range profile sampling rate of the P410 radar is limited by the number of range bins measured. It is observed that, for relatively straight-bladed turbines (such as those to be examined in this section), the dominant backscattering occurs during the blade flash and contributions outside the blade flash are almost negligible. The blade flash occurs when the blade is perpendicular to the RLOS and is typically focused in a few range bins near zero down-range. Therefore, only a limited number of range bins centered on the hub need to be captured to account for most of the turbine return in down-range. On the other hand, sufficient sampling in angle is still required in order to achieve unaliased cross-range. This concept will be illustrated on a 5 m diameter windmill before it is applied to a utility-class wind turbine. For these larger wind turbines, motion compensation made negligible improvement to the quality of the final image.

3.4.1 Windmill

In-situ measurement is made at a windmill in Cedar Park, Texas [47]. The eighteen-blade windmill has a rotor diameter of approximately 5 m. Measurement is done at a 45° elevation angle from the radar perspective at a distance of 25 m to the hub. This reduces down-range extent to 3.53 m. The rotation rate is approximately 13 rpm during the collection. The maximum Doppler extent is 170 Hz at 5.3 GHz and is fully captured by the 200 Hz radar sampling rate. Fig. 3.9(a) shows the windmill from the radar perspective. Fig. 3.9(b) shows the simplified FEKO simulation model for the windmill. For this dataset, no motion compensation is found to be necessary.



(a)



(b)

Fig. 3.9 (a) Windmill photo. (b) Simplified simulation model.

The measured and simulated sinograms are shown in Fig. 3.10. There is reasonable agreement between measurement and simulation. The strong periodic return near zero down-range is the flash of a single blade as it becomes perpendicular to the RLOS. There are also 18 faint tracks that extend beyond the blade flash. Each track corresponds to the return from the outer tip of one of the 18 blades. It follows the expected sinusoidal trajectory through the first half of a rotation. Due to the pitch of the blade, the trajectory of the second half of the rotation is much weaker in strength and becomes difficult to see within the 40 dB dynamic range. There should also be faint tracks that correspond to returns from the inner blade tips. However, they are much weaker and are again difficult to see within a 40 dB dynamic range.

Note that we were not able to fully capture the down-range extent of the windmill in measurement due to the need for a narrow range gate (set at 2.63 m) in order to achieve the 200 Hz range profile sampling rate. We have cropped the simulation plot in down-range for a one-to-one comparison with the measurement. It should also be noted

that, within a 25 dB dynamic range, only the blade flashes (which occupy about 25 cm of down-range) are visible.

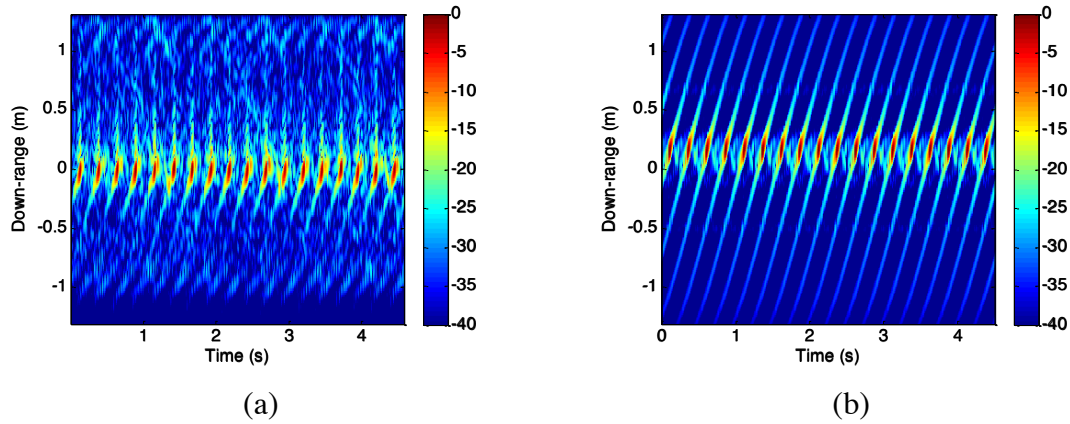


Fig. 3.10 Windmill sinogram. (a) Measurement. (b) Simulation.

Fig. 3.11 shows the spectrograms obtained using the STFT with a 260 ms Hamming window. Both spectrograms show a sequence of prominent negative Doppler flashes, which occur at time instances when the blades become perpendicular to the RLOS while receding away from the radar. By comparison, the positive Doppler returns are much weaker. This confirms the observation made based on the sinograms that each blade is only prominent for half a rotation due to the blade pitch angle. The slight fluctuation in the maximum Doppler extent as a function of time in the measurement is due to the windmill speed fluctuating slightly over the 4.5-second span. The estimated maximum Doppler extent at 4.3 GHz is 138 Hz based on Eq. (3.1) and matches well with the Doppler extent observed in the spectrogram—thus, it has been fully captured in Doppler.

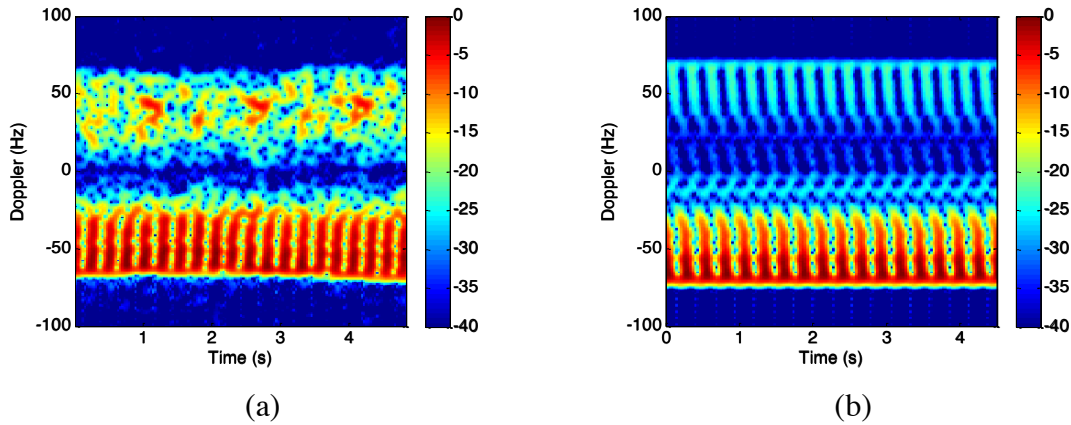


Fig. 3.11 Windmill spectrogram. (a) Measurement. (b) Simulation.

We use an angular swath of 20° to generate ISAR snapshots of the windmill in both simulation and measurement. As we slide the 20° angular swath along the angular (or time) axis, we can see each blade ‘lights up’ as it becomes perpendicular to the RLOS near zero down-range. This is easily seen in a movie made of many consecutive ISAR frames. Here, we have shown several snapshots that highlight the sequence before, during, and after the blade flash in Fig. 3.12. The measurement data are presented on the left and the simulated data on the right. The snapshots going down each column are five equally spaced instances spanning 20° (4° spacing between each snapshot). The maximum blade flash occurs at the middle of the sequence, as shown by Figs. 3.12(c)(h). There are some minor differences between the measurement and simulation. They can be explained by the simplified geometry of the model and the physical optics simulation that ignores higher order interactions.

Focusing on the blade flash in Figs. 3.12(c)(h), we observe two distinct features at zero down-range. Each is a blade flash, with the one on the left much stronger than the one on the right due to the pitch of the blades. At the same time, a faint outline of the outer and inner tips of the other blades can be clearly seen in the simulation. It is less

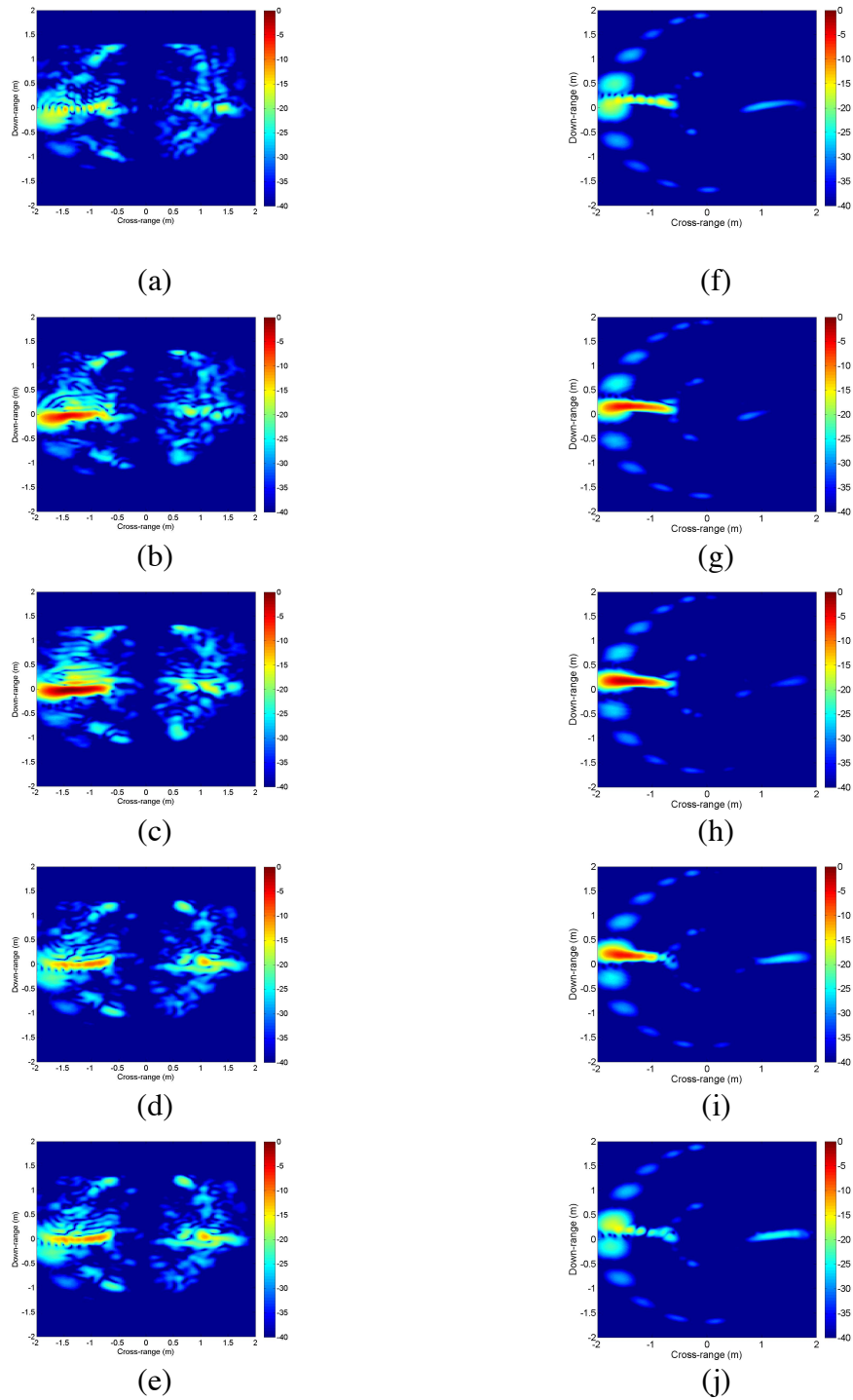


Fig. 3.12 Windmill ISAR snapshots. (a)-(e) Measurement. (f)-(j) Simulation.

apparent in the measurement results. On the other hand, an outline of a middle ring can be noticed in the measurement data. This middle ring can be seen in the Fig. 3.9(a) photo, but was not included in the simulation model. Finally, due to the limited range gate, the entire turbine was not fully captured in measurement. As a result, the image intensity beyond the ± 1.32 m down-range extent is zero. This truncation effect can be noticed in the measurement data.

Fig. 3.13 shows the resulting 360° ISAR images. Fig. 3.13(a) shows the measured ISAR image generated using a limited range gate. Fig. 3.13(b) shows the simulated 360° ISAR image with sufficient sampling to fully capture the windmill in down-range. The windmill has been fully captured in both measurement and simulation and there is good agreement between them. Again, the minor differences between simulation and measurement can be attributed to the simplified geometry and the physical optics simulation that ignore higher-order interactions. Overall, it has been shown that a straight-bladed turbine can be fully imaged in measurement even with a limited range gate.

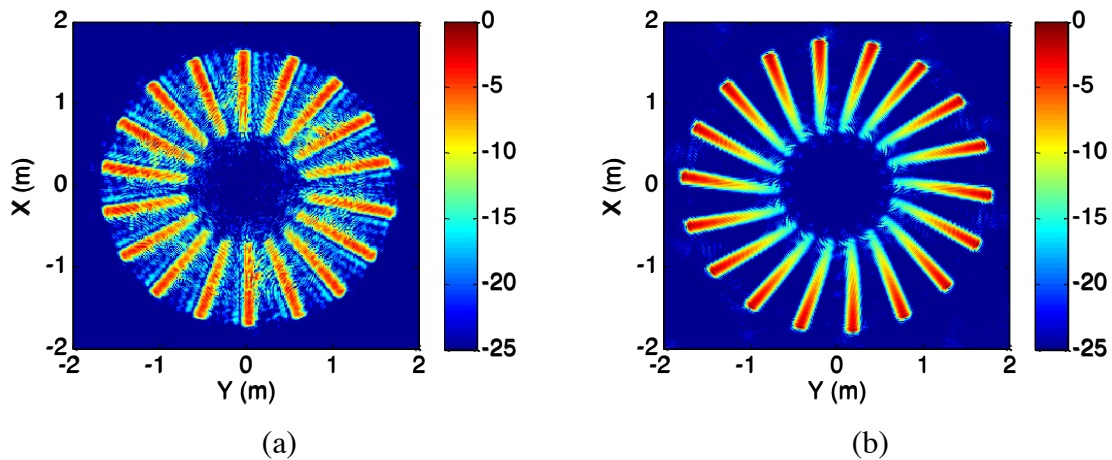


Fig. 3.13 360° ISAR image of a windmill. (a) Measurement. (b) Simulation.

3.4.2 Utility-Class Wind Turbine

Next, we apply this methodology to a utility-class wind turbine. In-situ measurement is carried out in West Texas. The wind turbine measured is a 1.7 MW General Electric turbine. Based on the manufacturer's specs, the distance from the ground to the hub is 80 m. The turbine rotor diameter is 100 m and each blade is 49 m long. The rotation rate was roughly 9 rpm during data collection. There are two major challenges to overcome in this measurement. First is the large Doppler extent of the turbine. The maximum Doppler extent of the turbine rotating at 9 rpm is more than 3000 Hz at 5.3 GHz at edge-on incidence (90° elevation angle). Second, due to a built-in software range limit on the P410 radar, the starting range gate must be less than 75 m. To partially alleviate the first issue, we switch to the previous generation Time Domain radar (P400), which supports an Ethernet connection that can sample up to 1500 Hz with range bins that span 1.76 m. To circumvent the second issue, a telescopic extension pole is used to elevate the radar by roughly 8 m. As a result, our setup involved mounting the radar and a single broadband horn on a telescopic extension pole. A single horn antenna is used for both transmit and receive through the use of a circulator (MCLI CS-16-50). Finally, the

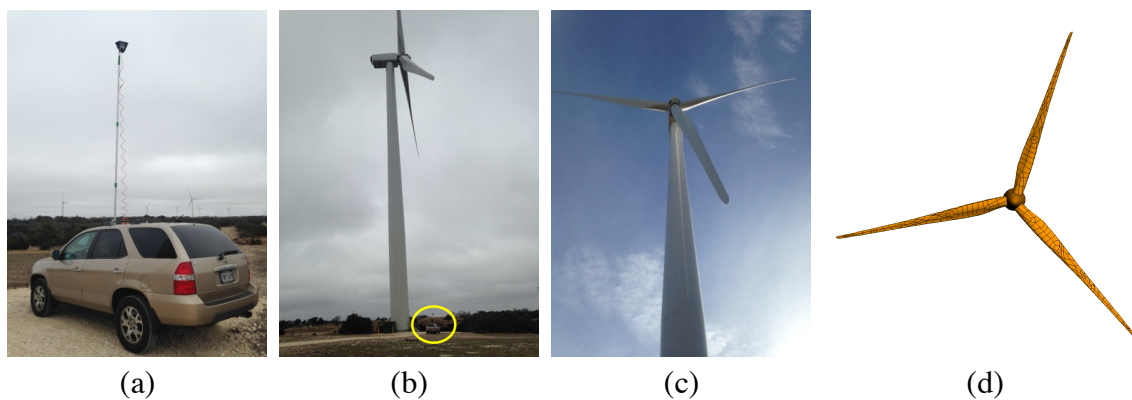


Fig. 3.14 Utility-class wind turbine. (a) Measurement setup. (b) Measurement at base of wind turbine. (c) Wind turbine from radar perspective. (d) Simplified simulation model.

radar is connected to a laptop via a long Ethernet cable. Measurement data are collected from the base of the wind turbine. Fig. 3.14(a) shows the measurement setup on a sports utility vehicle. Fig. 3.14(b) shows the measurement at the base of the wind turbine with the vehicle highlighted. Fig. 3.14(c) shows the turbine from the radar perspective. Note that each blade has a straight leading edge and a kink in the trailing edge.

At such a close distance from the radar to the turbine, near-field effects are significant and must be carefully addressed. We first note that due to the close-in setup, the tip of the blade is farther in range than its base. Therefore, using a 1.76 m range gate, only the inner portion of the blade is captured in the measurement. An interesting consequence of this effect is that the maximum Doppler rate of the collected data is reduced and falls within the 1500 Hz sampling rate of the P400 radar. Therefore, it becomes possible to collect range profiles at sufficient sampling to avoid any aliasing in the final ISAR image. Secondly, because the collected near-field data are mismatched to the ISAR imaging algorithm, which is based on the far-field assumption, the resulting ISAR image will be distorted.

There are two ways to overcome this effect. One is to modify the imaging algorithm to account for the near-field distance. This can be accomplished through a matched filter/backprojection algorithm [67]. However, the image formation time is usually much longer since an FFT cannot be used. Another approach is to apply a near-field to far-field transformation (NFFFT) to transform the collected near-field data to the far field [68, 69], after which the same far-field FFT-based imaging algorithm can be used. We adopt the latter approach here, where the Vaccaro-Mensa NFFFT [68] is applied. A point-scatterer simulation is used to illustrate the effectiveness of this approach. Near-field data are simulated at a distance of 80 m using a collection of point scatterers. Fig. 3.15(a) shows the resulting image generated from the FFT-based imaging

algorithm. It has been shown in [39] that near-field effects cause tilting in the blade flash in the spectrogram. This tilting can be observed in the resulting ISAR image and manifests itself by creating a cross-over between the leading edge and trailing edge of the turbine blade (this is a severe case of the splitting observed in Fig. 3.7). Fig. 3.15(b) shows the resulting image generated from far-field data where the leading and trailing edges of the turbine blade are appropriately aligned.

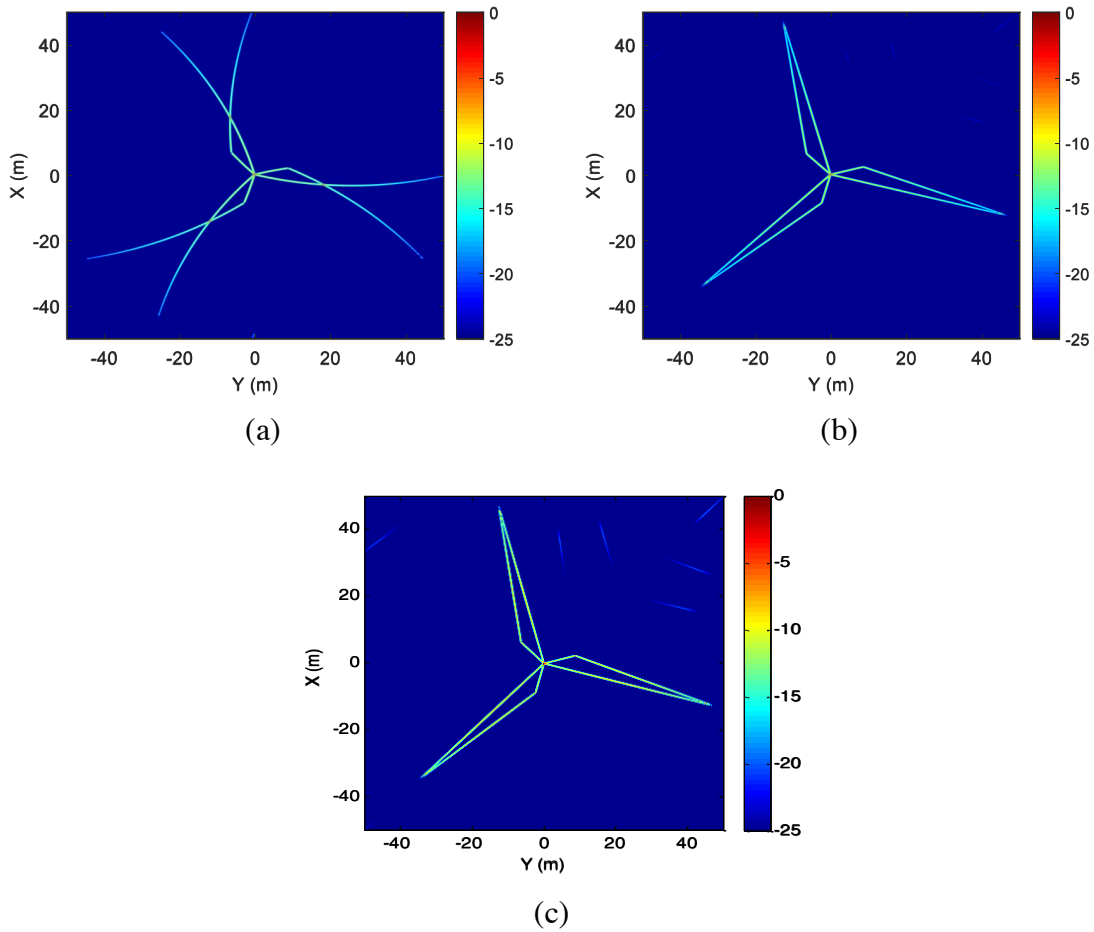


Fig. 3.15 Utility-class turbine point-scatterer simulation. (a) Near field. (b) Far field. (c) NFFFT applied to near field.

Next, we apply the NFFFT to the near-field data using the following formulas [68, 69] (the derivation of these formulas is discussed in the Appendix):

$$E^{s,ff}(f, \phi) = \sum_{\phi=-\phi_{half}}^{\phi_{half}} E^{s,nf}(f, \phi) e^{-j4kr \sin^2(\frac{\phi}{2})} \Delta\phi \quad (3.4)$$

$$\text{where } \begin{cases} \phi_{half} = \phi_{ext} + \phi_{win} \\ \Delta\phi = \frac{\lambda}{4r(2\phi_{ext} + \phi_{win})} \end{cases} \quad (3.5)$$

where r is the distance from the radar to the center of rotation, $k = 2\pi f/c$, $\phi_{win} = \sqrt{3\lambda/r}$, $\phi_{ext} = \tan^{-1}(R_{rotor}/r)$, and R_{rotor} is the turbine rotor radius. After an NFFFT is applied to the near-field data, the resulting image is shown in Fig. 3.15(c). It is nearly indistinguishable from Fig. 3.15(b), demonstrating the effectiveness of the NFFFT.

The NFFFT is applied to the measurement data from the utility-class turbine. Fig. 3.16(a) shows the resulting sinogram over one revolution of the turbine. There are six vertical lines in the measured sinogram that correspond to the six blade flashes captured within the 1.76 m range gate. Fig. 3.17(a) shows the measured spectrogram at 4.3 GHz generated by using the STFT with a Hamming window of 175 ms (10° angular swath). The positive Doppler flash is relatively straight and corresponds to the blade flash observed from the straight leading edge of the blade. The negative Doppler flash is kinked and corresponds to the blade flash observed from the kinked trailing edge of the blade. The resulting 360° ISAR image is shown in Fig. 3.18(a). No motion compensation is found to be necessary. The final ISAR image clearly reveals the scattering contribution from the relatively straight leading edge as well as that from the kinked trailing edge of the turbine blade. Only the inner portion of the turbine blades (up to about 25 m) is

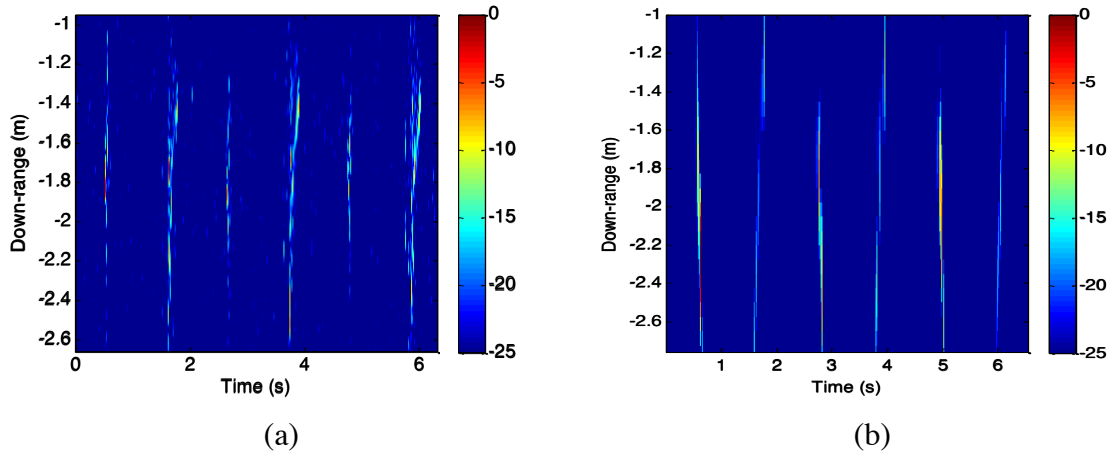


Fig. 3.16 Utility-class turbine sinogram. (a) Measurement. (b) Simulation.

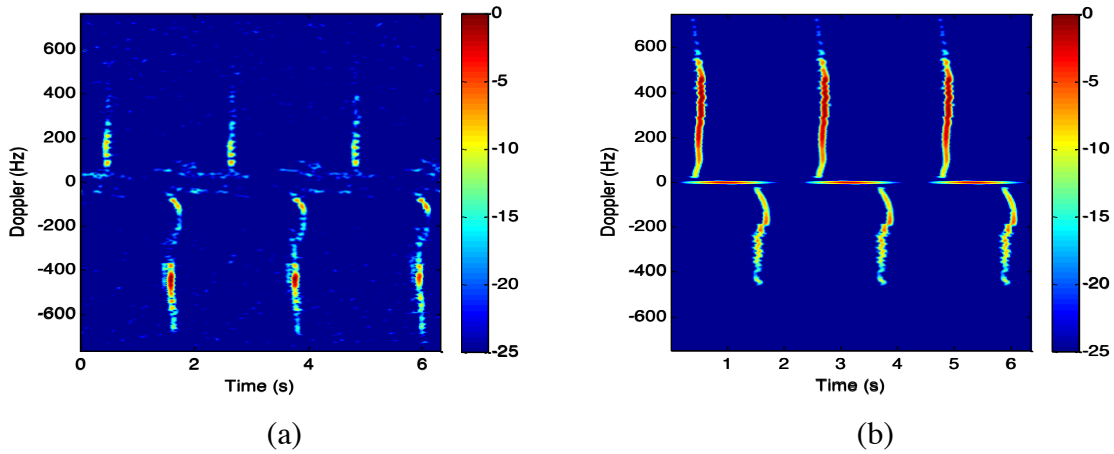


Fig. 3.17 Utility-class turbine spectrogram. (a) Measurement. (b) Simulation.

captured in the data due to the range gate used in the measurement. Consequently, there is no aliasing in the final image.

Simulation is carried out to corroborate the measurement results. Fig. 3.14(d) shows the simplified turbine model used in simulation. This model was obtained online (GrabCAD) and is only a generic utility-class wind turbine CAD model. In order to save

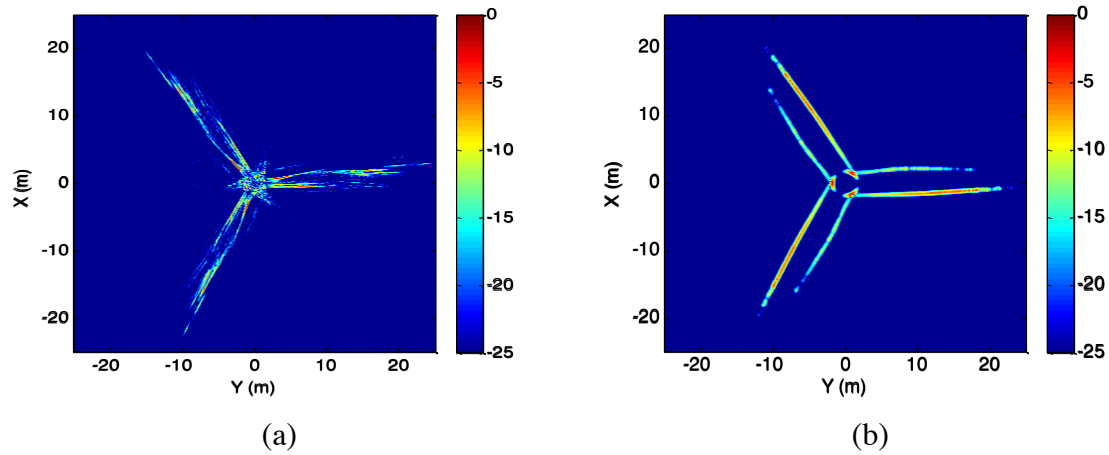


Fig. 3.18 Utility-class turbine 360° ISAR image. (a) Measurement. (b) Simulation.

computation time, at the cost of some numerical accuracy, the FEKO large-element PO solver is used. To further increase simulation speed, only 500 MHz of bandwidth is used. While the range resolution is reduced as a result, the same phenomenology is captured. The following frequency and angular steps are used: $\Delta f = 5$ MHz and $\Delta\phi = 0.02^\circ$. The same set of processing steps is applied to the near-field simulation data. First, the data are range-gated to the 3.20 m about the hub region. Next, the NFFFT is applied to transform the data to the far field. Figs. 3.16(b), 3.17(b), and 3.18(b) show respectively the sinogram, spectrogram, and 360° ISAR image based on simulated data. In Fig. 3.16(b), the same six blade flashes seen in Fig. 3.16(a) can also be seen. The differences in amplitude can be accounted for through differences between the CAD model and the physical turbine. Comparing Fig. 3.17(b) to Fig. 3.17(a), the amplitude differences are more evident. Measurement shows the negative Doppler more prominently than the positive Doppler whereas simulation has the opposite trend. This discrepancy is also reflected in the final ISAR images of Figs 3.18(a) and 3.18(b). The measurement shows the trailing edge more prominently whereas simulation shows the leading edge more

prominently. The geometry differences between the CAD model and the physical turbine are more evident here. In particular, the base of the turbine blade in the CAD model is much thicker. Nonetheless, the key scattering features between measurement and simulation are similar.

3.4.3 Updated Measurement Setup

In September, 2015, Time Domain Corporation released their next-generation radar, the PulsON 440 (P440). In comparison to the P410 radar, the P440 radar has the starting range gate limit extended to 120 m and the Ethernet port reinstated. Consequently, the measurement setup can be simply placed on the ground without the need for an extension pole. Fig. 3.19(a) shows the new measurement setup, and Fig. 3.19(b) shows the resulting 360° ISAR image from measurement taken at the base of the wind turbine. The same scattering phenomenology can be seen in Fig. 3.19(b) and 3.18(a). There are some small differences between the two figures. The most prominent is the different RCS levels along the leading edge and trailing edge of the turbine blades between the two images. While both measurements were done at the base of the wind

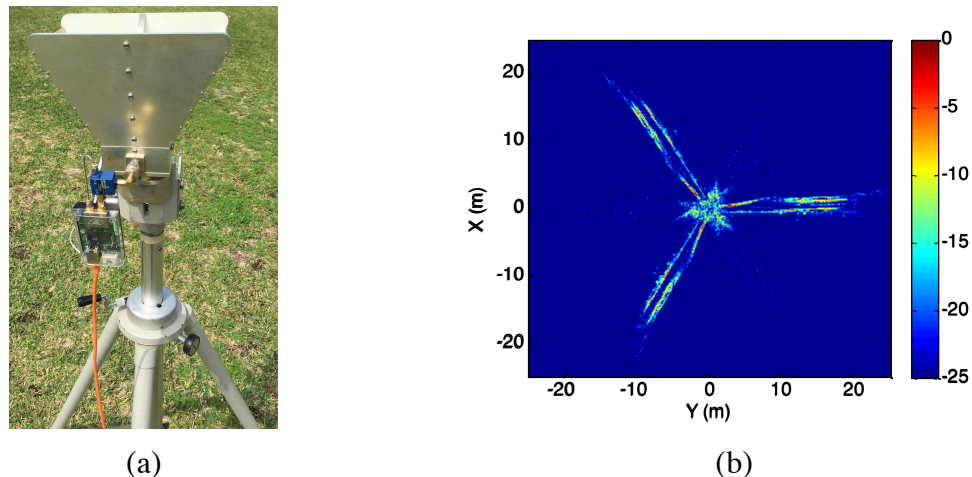


Fig. 3.19 P440 measurement. (a) Measurement setup. (b) 360° ISAR image.

turbine, several factors may be slightly different between the two measurements. These include turbine yaw angle, turbine blade pitch, and measurement incident angle. Each of these factors could affect the RCS levels along the turbine blade.

3.5 CONCLUSION

In this chapter, we have developed the measurement and processing methodologies to capture the in-situ ISAR image of an operating wind turbine. The methodologies were first tested and validated on a small wind turbine using an ultra-wideband radar. Motion compensation and image formation algorithms were implemented to generate a well-focused ISAR image. Results were compared to those generated using the physical-optics simulation, and good agreement between measurement and simulation was observed. It was shown that the resulting ISAR images provided revealing geometrical insight on the blade scattering phenomenology that is not as apparent in either the range profile or Doppler spectrogram alone. The same methodologies were then applied to a larger 18-blade windmill and a 1.7 MW utility-class wind turbine. In the latter case, additional near-field effects due to the maximum range limit of the radar were encountered. They were corrected using a near-field to far-field transform, and the inner portion of the turbine blades was successfully imaged. Potential applications for this work include clutter mitigation, radar signature reduction, and structural health monitoring of wind turbines. First, matched filters may be constructed based on measured data for filtering out turbine clutter. Second, ISAR images can reveal spatial information on portions of the blade that give rise to the strongest scattering, which could be useful in the design of stealthy turbine blades [70, 71]. Finally,

radar imaging may potentially be used for monitoring motion anomalies and/or lightning damage of turbine blades for structural health monitoring.

Chapter 4: ISAR Imaging of a Vertical-Axis Wind Turbine⁴

4.1 INTRODUCTION

In the previous chapter, the radar signatures of horizontal-axis wind turbines (HAWT) were examined in detail. Recently, the US Department of Energy is considering vertical-axis wind turbines (VAWT) as a potential candidate for off-shore wind power generation [48]. Some of the potential advantages of a VAWT over its HAWT counterpart include better scalability to large sizes and mechanical simplicity for service and maintenance. From the radar perspective, it becomes important to evaluate how the radar signatures of a VAWT differ from those of the more commonly seen three-blade HAWT. Figs. 4.1(a) and 4.1(b) show a HAWT and VAWT, respectively.

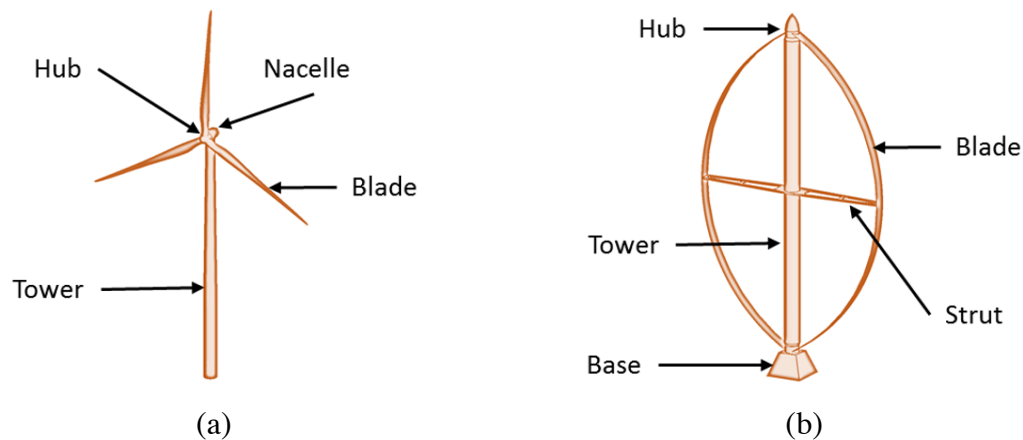


Fig. 4.1 Two types of wind turbines. (a) Horizontal-axis wind turbine. (b) Vertical-axis wind turbine.

In this chapter, we investigate the dynamic radar signatures of a Darrieus-type VAWT. The radar cross section (RCS) of a small helical VAWT was briefly discussed in

⁴ C. J. Li, R. Bhalla, and H. Ling, "Investigation of the dynamic radar signatures of a vertical-axis wind turbine," *IEEE Antennas Wireless Propag. Lett.*, vol. 14, pp. 763-766, 2014. Chenchen Jimmy Li was the primary author for all content in the above publication.

[43]. Our focus here is to examine the time-varying radar features and analyze their associated phenomenology. This information can facilitate the development of clutter filtering algorithms, as in the case of the HAWT [34]. This chapter is organized as follows. As with the HAWT, we start with by validating measurement with PO simulation on a small turbine. A 1.5 m model of a Darrieus-type turbine is constructed and investigated. The scattering physics behind the observed features from the blade, strut, and tower structures is discussed. After validating PO simulation with measurement for the small model, PO simulation of a 112 m tall Darrieus wind turbine is carried out at 1.5 and 3 GHz to predict the resulting signatures. The results are compared with those of a three-blade HAWT. Lastly, effects from a conducting ground plane are examined in connection with the operation of these turbines over water.

4.2 MEASUREMENT AND SIMULATION SETUP

Measurement backscattered data are collected using S_{11} measurement from a vector network analyzer and a Ku-band standard gain horn (Narda 4609, 12-18 GHz) from 12-15 GHz. A simplified model of a Darrieus-type wind turbine, seen in Fig. 4.2(a), is constructed and measured. The model is 1.5 m tall (an electrical size of $\sim 75 \lambda$ at 15 GHz) and 0.9 m in diameter. The blades and strut are constructed using foam and covered in aluminum tape, and a wooden rod is used as the tower. The model is placed on a turntable to rotate for a complete revolution. The measurement is done at near-zero elevation angle.

Simulated backscattered data are generated using the PO with shadowing solver in FEKO. An approximate model created in FEKO with PEC, seen in Fig. 4.2(b), is used. Edge diffraction and material effects are not included in the simulation. These effects are

expected to change only the strength but not the behavior of the predicted features. A plane wave source from 12-15 GHz is assumed for the excitation. To provide a sufficient down-range window without aliasing, 41 frequency points are computed. To simulate the rotating turbine, the incident azimuth angle is varied from 0° to 360° . The result is the radar signature as a function of angle (or time). The angular sampling is chosen to be 0.3° to provide a sufficient cross-range (or Doppler) window without aliasing.

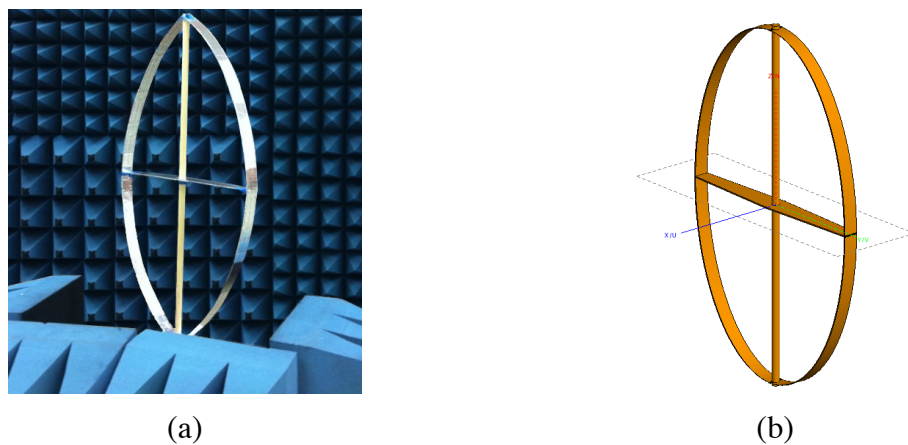


Fig. 4.2 Simplified Darrieus-type turbine model. (a) Measurement. (b) FEKO.

4.3 MEASUREMENT AND SIMULATION RESULTS

The dynamic signatures from the measured and simulated backscattered data versus time (or turbine rotation angle) are post-processed into sinograms, spectrograms, and ISAR images. The turn-table rotation rate is 830 seconds per revolution. Vertical polarization is used for both transmit and receive. The measured data are not calibrated in terms of absolute RCS level, but the same dynamic range is kept for simulation and measurement.

The measured and simulated sinograms are shown in Fig. 4.3. The range profile is obtained through the inverse Fourier transform of the frequency response with a Hamming window. Four key features are observed in the sinograms. The first two are the sinusoidal trajectories labeled as (i) and (ii) in Fig. 4.3(a). The associated mechanisms are the returns from the rotating blades that are shown in Fig. 4.4(a). Due to the curvature of the blades in elevation, the scattering from each blade is specular in elevation and only the region denoted by the dashed red circle contributes to each feature. As the blades rotate, they form two sinusoidal tracks in the sinogram. Along each track, a strong return occurs at the range of -0.5 m. This flash occurs when the front face of the blade is perpendicular to the RLOS. The next feature is the horizontal line at zero down-range and labeled as (iii) in Fig. 4.3(a). The associated mechanism is the return from the tower (shown in Fig. 4.4(b)). Mounting and physical imperfections of the wooden tower caused minor fluctuations in the static tower return. The final feature is due to the return from the strut. However, this feature overlaps with the blade returns in the sinogram. It is most prominent when the strut is perpendicular to the RLOS, as labeled by (iv) in Fig. 4.3(a).

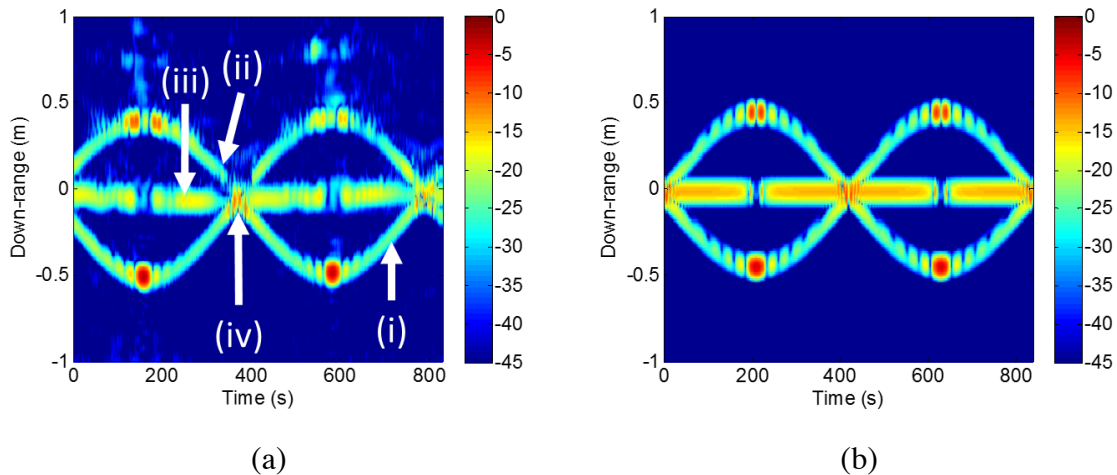


Fig. 4.3 Sinogram of simplified turbine model. (a) Measurement. (b) Simulation.

In addition to these four noted features, when one of the blades rotates to the front (most negative in down-range), shadowing of the tower and rear blade occurs. This can be clearly seen in both measurement and simulation. Overall, PO simulation is able to capture the dominant target features in the measurement. The only noticeable difference is the weak, range-delayed (beyond 0.5 m) multiple scattering returns seen in the measurement but not in the PO simulation. It is localized in angle only around where the tower and rear blade are shadowed.

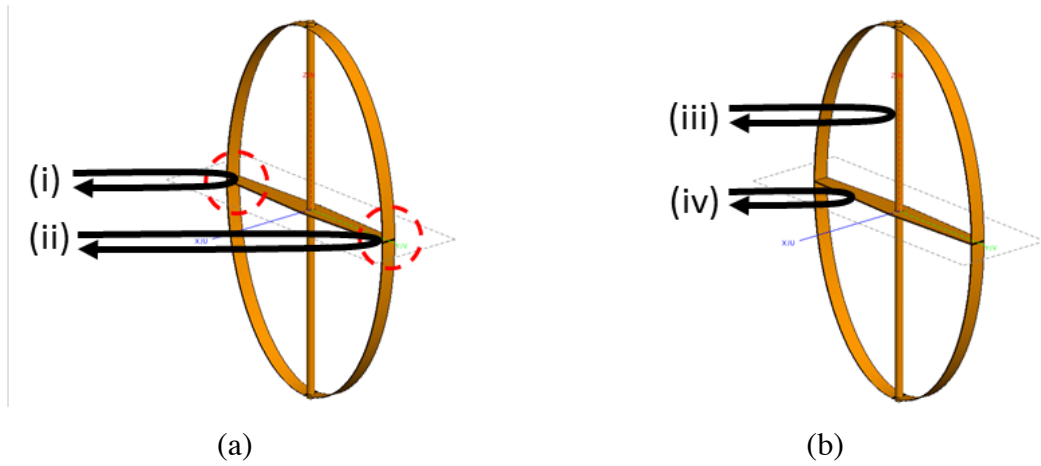


Fig. 4.4 Scattering mechanisms. (a) Blade returns. (b) Tower and strut returns.

The time-dependent Doppler behavior of the target is also examined in the form of a spectrogram. Using the STFT with a 29 s (equivalently 13°) Hamming window in time at a fixed frequency, the spectrogram is obtained. Fig. 4.5(a) shows the spectrogram at 13.5 GHz from measured data. The rotation rate of the turn-table is 0.0076 radians per second. As a result, the maximum Doppler extent is ± 0.31 Hz (based on $f_D = 2R\Omega/\lambda$ where R is the radius of the turbine blade, Ω is the rotation rate, and λ is the wavelength at 13.5 GHz). Four key features are noted. The first two are the sinusoidal trajectories

labeled as (i), (ii). The associated mechanisms are the returns from the highlighted areas on the rotating blades shown in Fig. 4.5(a). When one of the blades rotates to the front, a strong blade flash is observed. At this angle, the blade motion is perpendicular to the RLOS and the flash appears in the zero Doppler bin. Next is the horizontal line at zero Doppler and labeled as (iii). The associated mechanism is the static return from the tower. The final feature is the region labeled as (iv) due to the strut. The strut return is only prominent when the strut is perpendicular to the RLOS. At this angle, all the radial components light up in their respective Doppler bins. Comparing the measurement in Fig.

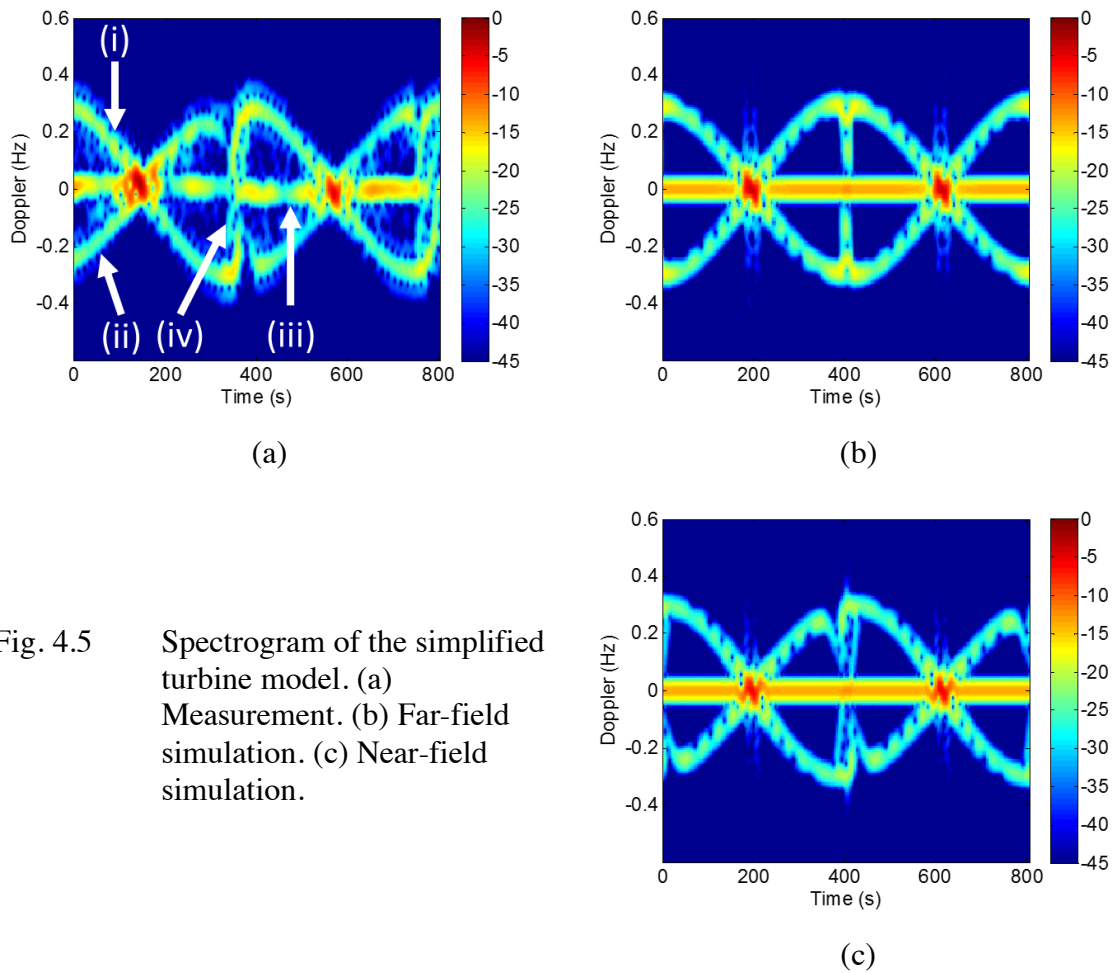


Fig. 4.5 Spectrogram of the simplified turbine model. (a) Measurement. (b) Far-field simulation. (c) Near-field simulation.

4.5(a) to the simulation in Fig. 4.5(b), we see that the strut features in the two spectrograms do not agree that well. This is due to the near-field effect in the measurement where the radial components of the strut are not perpendicular to the RLOS simultaneously but exhibit different temporal delay. This results in the flash being tilted [39]. To confirm this, a near-field simulation is shown in Fig. 4.5(c). It shows the same tilting in the strut flash as measurement. Additionally, simulation is carried out for the horizontal polarization case and the signatures are found to be the same as the vertical polarization results.

Finally, ISAR images are generated using the k -space formulation. Each ISAR snapshot is generated using a 12.7° angular swath. This angular window is chosen based on the narrow-band, small-angle approximation shown in the second part of Eq. (2.8) to achieve an equal down-range and cross-range resolution of 5 cm (without windowing). A sequence of ISAR snapshots are shown in Fig. 4.6. Good agreement can be seen between measurement and simulation. Again, we identify the four key scattering features in these images. In Figs. 4.6(a) and 4.6(c), the spot in the center of the image is the static tower return and is labeled (iii). The two spots to the side of the tower return are the two blade returns and are labeled (i) and (ii). The blade returns rotate around the tower return as the wind turbine rotates. In Fig. 4.6(d), the prominent feature is the strut return that occurs when the strut is perpendicular to the RLOS and is labeled (iv). In Fig. 4.6(b), one of the turbine blades is in front of the rest of the turbine. As mentioned previously, a particularly strong blade return is observed due to the blade flash at this angle. Due to shadowing, the scattering features in the rear are weakened. Finally, the faint features that are observed further in down-range (beyond 0.5 m) are due to multiple scattering. They are absent in the PO simulation result of Fig. 4.6(f), as expected.

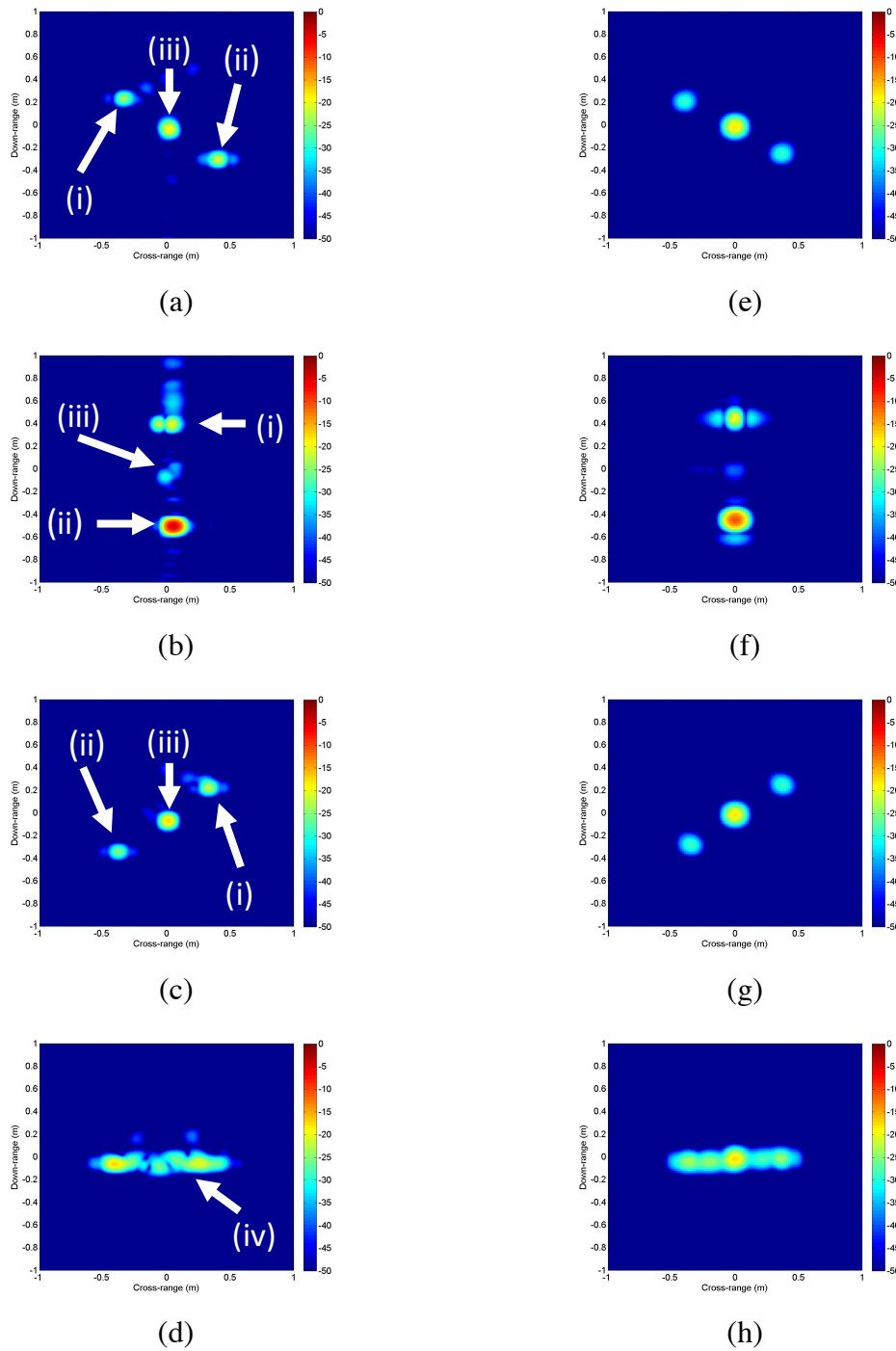


Fig. 4.6 ISAR snapshots of the simplified turbine model. (a)-(d) Measurement. (e)-(h) Simulation.

4.4 FULL-SIZE TURBINE SIMULATION

The previous results have shown that PO with shadowing is sufficient to capture most of the key dynamic radar signatures of a VAWT. Next, the full-size turbine is investigated using FEKO simulation. The complete structure is 112 m tall and 60 m in diameter and was previously shown in Fig. 4.1(b). To emphasize the dynamic signatures, the static portions of the structure are removed for the simulation. The blades are 100 m in height (an electrical size of $\sim 1000 \lambda$ at 3 GHz). With simulation validated against measurement for a 75λ model, we expect the high-frequency prediction method (PO) to be even more accurate for the larger, 1000λ model (equivalently higher frequency). To save computation time, at the cost of some numerical accuracy, the large-element PO method in FEKO is used. Horizontal polarization is used for transmit and receive at 0° elevation. We examine the spectrogram at two key frequencies of interest: 1.5 GHz (long range surveillance) and 3 GHz (weather, air-traffic control, marine navigation). For comparison, we also simulate a 112 m tall HAWT turbine shown in Fig. 4.1(a). The blades are 38 m long. Again, the static portions are removed from the model. The rotation rate is set to 10 rpm for both turbines. The results are shown in dBsm.

The simulated spectrograms for the VAWT at 1.5 GHz and 3 GHz, obtained using a 0.22 s (equivalently 13°) time window, are shown in Figs. 4.7(a) and 4.7(b), respectively. The results at 1.5 and 3 GHz show a similar set of features with a factor-of-two difference in Doppler extent. With the tower removed, there are only three scattering mechanisms. The sinusoidal trajectories labeled as (i) and (ii) correspond to the blade returns. When a blade rotates in front, the face of the blade becomes perpendicular to the RLOS and a blade flash is observed (the strong region around zero Doppler). The negative Doppler trajectories are weaker due to the blade shape and pitch (different from the 75λ model blades that were front-back symmetric). Lastly, the vertical line labeled as

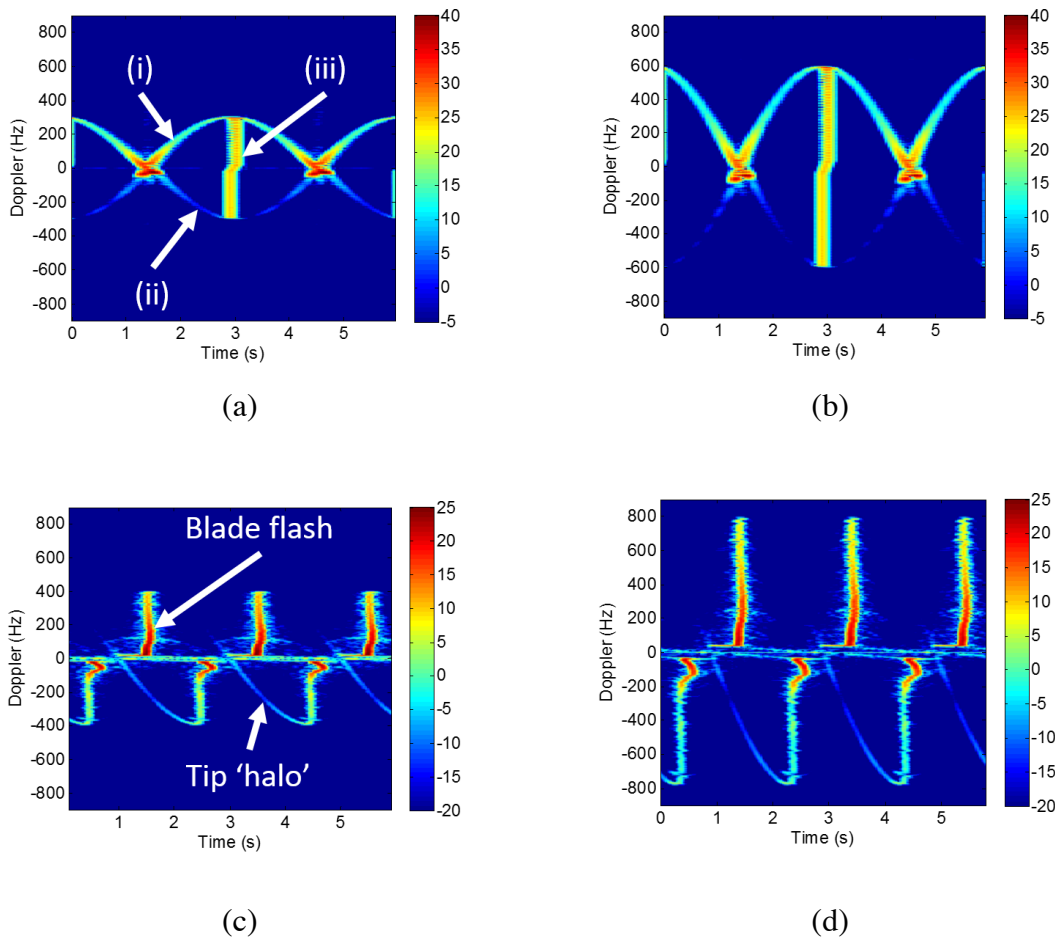


Fig. 4.7 Full-size turbine spectrogram. (a) VAWT 1.5 GHz. (b) VAWT 3 GHz. (c) HAWT 1.5 GHz. (d) HAWT 3 GHz.

(iii) corresponds to the strut flash when the strut becomes perpendicular to the RLOS. Due to the tapering in the strut, the positive and negative Doppler flashes are not concurrent.

Figs. 4.7(c) and 4.7(d) show the spectrograms for the HAWT under edge-on incidence at 1.5 GHz and 3 GHz respectively. The key scattering features of a HAWT comprise of strong blade flashes and weak tip ‘halos.’ These features have been examined closely in the previous chapter and will not be elaborated here. Instead, we

compare the differences between the dynamic features of the VAWT and those of the HAWT. First, the three positive and three negative blade flashes in the HAWT are replaced by one two-sided strut flash in the VAWT. Second, the weak sinusoidal tip halos of the blades in the HAWT are replaced by the stronger blade specular return in the VAWT. Finally, the maximum Doppler extent of the HAWT is dependent on the yaw angle of the turbine (which is dictated by the wind direction) with respect to the radar. The turbine gives rise to a maximum Doppler spread from an edge-on view but near-zero Doppler at a frontal view. On the other hand, the Doppler extent of the VAWT is independent of the wind direction since it rotates about a vertical axis. Note that the Doppler extents of both types of turbines are elevation angle dependent.

4.5 GROUND-BOUNCE EFFECTS

Simulation with the inclusion of an infinite PEC ground plane is performed to investigate the time-varying features that arise from turbine-ground interactions. This could be an important effect for close off-shore wind turbines, where the ground bounce returns from a calm sea surface are expected to be strong, or for an airborne radar. The radar signatures of a HAWT in the presence of a PEC ground have already been investigated in [72]. It was shown that the ground bounce contributions are delayed in dwell time relative to the direct path. Using image theory, we simulate the four separate scattering components for a VAWT at a 20° elevation using horizontal polarization at 1.5 GHz. Fig. 4.8 shows the four components: the direct path, two single-bounce paths, and the double-bounce path. Higher order interactions are ignored in this construct.

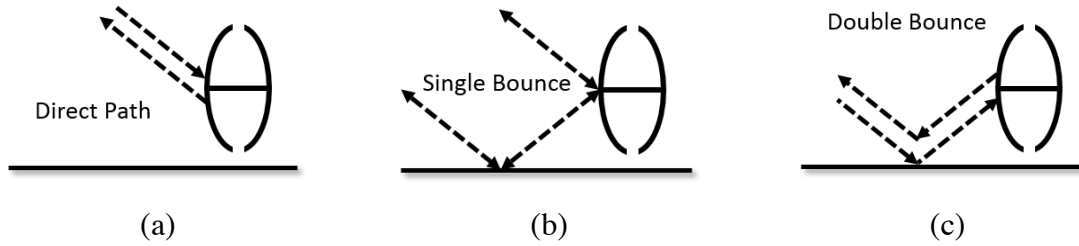


Fig. 4.8 Vertical-axis wind turbine with ground bounce. (a) Direct path. (b) Two single-bounce paths. (c) Double-bounce path.

Due to the symmetry of the structure, the direct path and double-bounce path spectrograms are identical and the sum is shown in Fig. 4.9(a). There are some notable differences from the 0° elevation case. The Doppler extent of each feature has been reduced by $\cos(20^\circ)$ and the Doppler extent of the blade returns have been further reduced due to a shift in the specular region. The strut flash (iii) is also weaker. Additional features, labeled as (iv), are observed due to the visibility of the four strut holes. Each of the four holes exhibits a flash when perpendicular to the RLOS and a faint sinusoidal specular trajectory as the strut rotates. Next, the two single-bounce spectrograms are identical and the sum is shown in Fig. 4.9(b). The single-bounce path exhibits a corner reflector effect and the returns are similar to the 0° elevation angle case with additional features from the strut holes. Fig. 4.9(c) shows the sum of all four components. It is interesting to note that the total return at non-zero elevation in the presence of ground is as strong as the direct return at zero elevation. In contrast to the HAWT case, the blade and strut flashes of all four components occur at the same instance in dwell time.

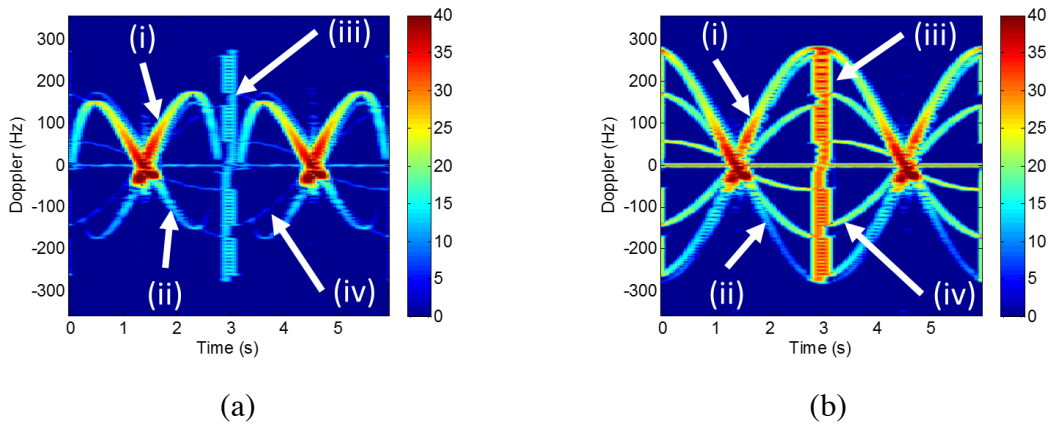
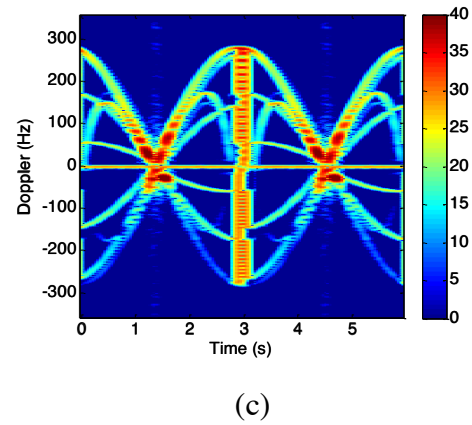


Fig. 4.9 Spectrogram of the full-size turbine with ground at 1.5 GHz. (a) Direct path and double-bounce contributions. (b) Two single-bounce contributions. (c) Sum of all four contributions.



4.6 360° ISAR IMAGE

For the sake of completeness, we also present the simulated 360° ISAR image of a full-size vertical-axis wind turbine. Fig. 4.10(a) shows the resulting ISAR image, generated by large-element PO simulation, using the same frequency band as the Time Domain UWB radar. Again, the four key scattering features can be identified in the ISAR image. Fig. 4.10(b) highlights the portions of the wind turbine that give rise to the associated scattering features.

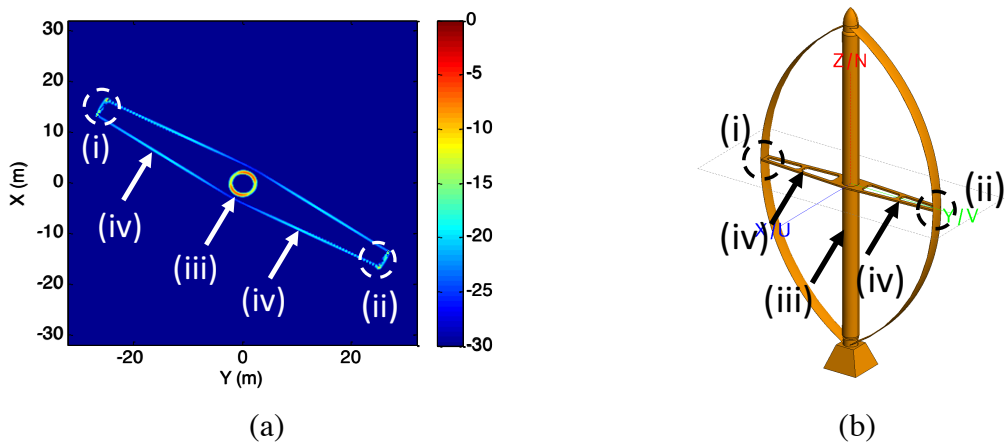


Fig. 4.10 (a) Full-size VAWT 360° ISAR image. (b) Associated regions.

4.7 CONCLUSION

In this chapter, the dynamic radar signatures of a VAWT have been investigated. First, measurement and PO simulation were carried out for a 1.5 m model to validate the PO prediction. The backscattered data in frequency and angle were post-processed to form the sinogram, spectrogram, and ISAR imagery. The scattering physics behind the observed features from the blade, strut, and tower structures was discussed. It was shown that PO was sufficient to capture the key scattering features of a VAWT. Subsequently, simulation of a 112 m tall Darrieus-type wind turbine was carried out at 1.5 GHz and 3 GHz and the resulting signatures are compared with those of a three-blade HAWT. Lastly, ground effects from a conducting ground plane were examined.

Chapter 5: Wide-Angle ISAR Imaging of Vehicles⁵

5.1 INTRODUCTION

Due to its all-weather, 24/7 capability, radar is a possible alternative to optical cameras for vehicle sensing in traffic monitoring and perimeter security applications. In addition to range and Doppler information, it is possible to generate a two-dimensional radar image of a vehicle using the synthetic aperture formed by the relative motion between the vehicle and radar. SAR imaging of stationary ground vehicles from airborne sensors has already been a subject of extensive investigations in the past [49-52]. Using SAR data, it has been shown that automated classification of ground vehicles is feasible. ISAR imaging of moving vehicles from a stationary ground sensor may also be realized under the proper conditions. Potential applications include vehicle classification for perimeter security and traffic monitoring for intelligent transportation systems [53]. Since the vehicle motion is unknown, blind motion compensation is needed to generate a well-focused image [54, 55]. To simplify the process, a small angular swath is usually used to form each image, even though wide-angle imaging may offer better resolution and richer geometrical features. In [56], 360° ISAR imaging was carried out to obtain a high-resolution image. However, the measurement was done on a turntable. In this chapter, we carry out in-situ, high-resolution ISAR imaging of moving vehicles from a stationary ground radar, with the aim of addressing two questions: (1) How well can motion compensation achieve a focused ISAR image under the wide-angle scenario, and (2) how well can wide-angle ISAR images reveal vehicle features.

To address these questions, we start by examining the “best-case” scenario where the vehicle position is known (also called cooperative imaging). This is done through the

⁵ C. J. Li and H. Ling, “Wide-angle ISAR imaging of vehicles,” in *Proc. European Conference on Antennas and Propagation*, Lisbon, Portugal, pp. 1-2, Apr. 2015.

Chenchen Jimmy Li was the primary author for all content in the above publication.

use of two additional Time Domain UWB transceivers, which can also be used as ranging radios. Thus, we bypass the challenging blind wide-angle motion compensation and first establish the imaging principles. To establish viability for vehicle classification, several different classes of vehicles are examined. The ranging radio data are used to carry out coarse motion compensation in order to establish a baseline wide-angle ISAR image. Next, fine motion compensation is applied using a local minimization of the image p -norm to generate more focused images. In this way, we are able to address our two objectives under the best-case scenario. Subsequently, we proceed to the realistic scenario and apply a blind motion compensation scheme based on the collected radar data only.

5.2 COOPERATIVE IMAGING

In-situ measurement is carried out using a P410 radar placed approximately 20 m from the side of a road. A single broadband horn is used for the radar for both transmit and receive through the use of a circulator. Vertical polarization is used on transmit and receive. The range profile vs. dwell time data are collected as each test vehicle drives by at low speed. The sampling rate for consecutive range profiles is set to 25 Hz. To gather ground truth position data, two additional P410 transceivers with omni-directional antennas (Time Domain's Broadspec UWB Antenna) are used as ranging radios. One is mounted on top of the vehicle (at approximately the geometrical center), and the other is placed next to the measurement radar. Fig. 5.1(a) illustrates the measurement scenario, and the inset figure shows the measurement collection setup that includes the horn, one of the ranging radios, and the P410 radar connected to a laptop via USB. Four test vehicles are shown in Fig. 5.1(b). The upper-left is a mid-size sports utility vehicle (SUV), the

upper-right is a mid-size sedan, the lower-left is a full-size truck, and the lower-right is a subcompact car.

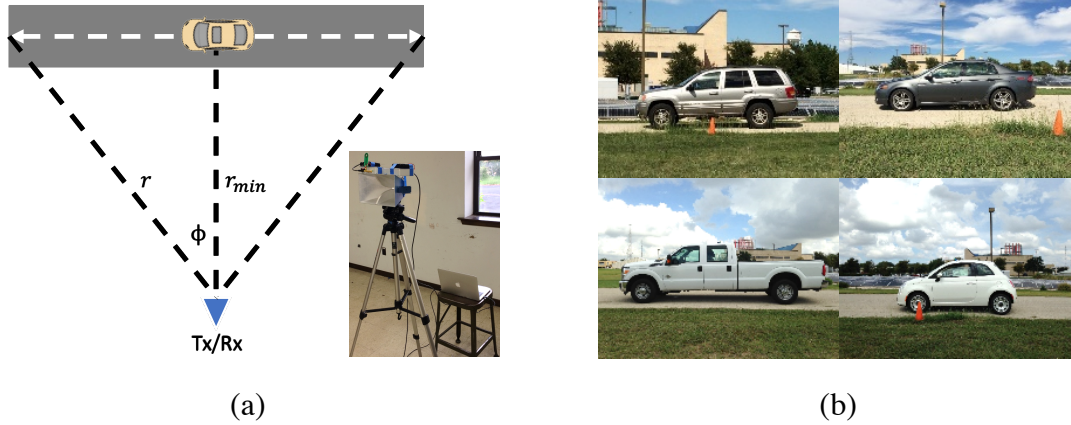


Fig. 5.1 Vehicle cooperative measurement synopsis. (a) Measurement scenario and collection setup. (b) Test vehicles.

One set of the collected range profiles vs. time is shown in Fig. 5.2(a). Significant range migration is observed due to the translational motion of the vehicle. Thus, to apply the same imaging formulation from previous chapters, we must remove the translational motion to retain only the rotational motion. By using the data collected from the ranging radii, coarse range alignment is implemented. Now, the location of the ranging radius (that was placed on the geometrical center of the vehicle) is in the same range bin for each range profile and is effectively the center of rotation for the target. Next, a wide-angle ISAR image is generated using the same procedure used for 360° ISAR imaging of wind turbines, except not all 360° are filled. The measurement angle is found from r and r_{min} as $\phi = \cos^{-1} r/r_{min}$ through the geometry in Fig. 5.1(a), where r is the range between the ranging radii. The k -space is only partially filled due to the limited bandwidth and measured angles. By assuming vehicle symmetry, the right half of the k -space can be mirrored to the left half. The resulting k -space data are shown in Fig. 5.2(b).

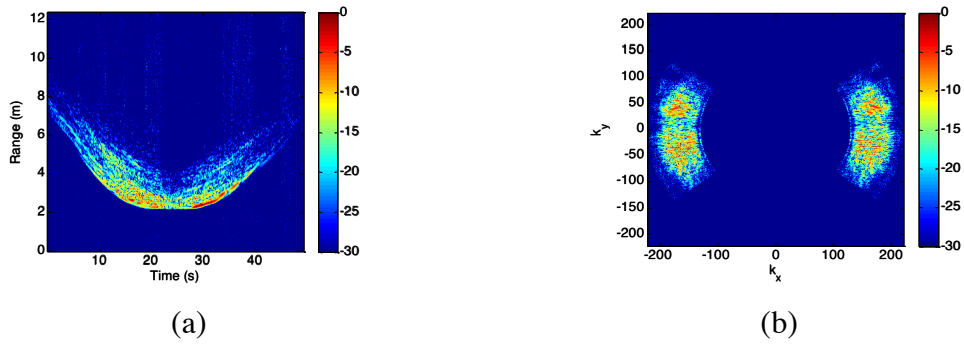


Fig. 5.2 Vehicle cooperative measurement. (a) Measured range profiles. (b) k -space data.

The resulting baseline ISAR images are shown in Fig. 5.3. In addition, a white outline of the top-view of each vehicle is provided below the image for reference. An outline of each vehicle can be discerned in the ISAR images, and a clear distinction can

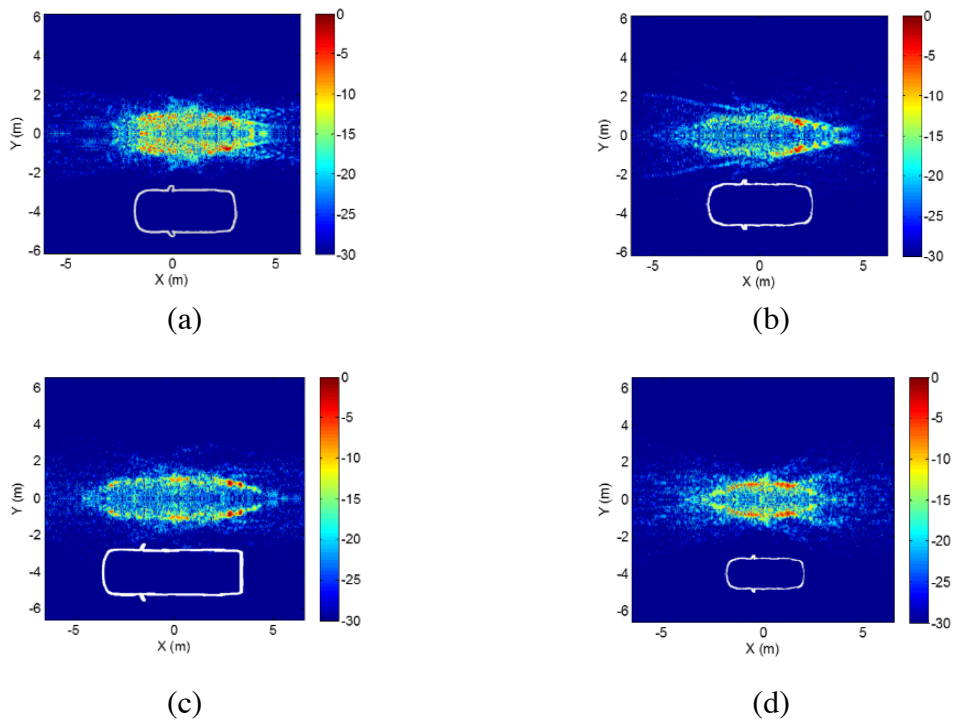


Fig. 5.3 Baseline images. (a) SUV. (b) Sedan. (c) Truck. (d) Subcompact.

be made between the mid-size, full-size, and subcompact vehicles. However, the images are not well focused. Significant smearing of features can be observed in the cross-range (or X) dimension, and considerable image intensity lies outside the vehicle footprint. This is believed to be due to the limited accuracy and low refresh rate of the ranging radio. Note, we have switched the convention from previous chapters such that X is now the cross-range dimension and Y is now the range dimension.

To correct for the phase errors still present in the coarse range-aligned data, we apply fine motion compensation to the ISAR images through a p -norm minimization. We model the vehicle range as a polynomial and apply a local optimizer to search for the motion parameters that minimize the p -norm of the image intensity. The p -norm of a matrix A is defined as:

$$\|A\|_p = \left(\sum_{n=1}^N \sum_{m=1}^M |A_{n,m}|^p \right)^{1/p} \quad (5.1)$$

Typically, $0 \leq p < 1$ is used to measure image sparsity [73]. Fig. 5.4 shows the focused images after the local search and motion compensation. Here, $p = 0.8$ and a 12th order polynomial is used to model the vehicle range. The resulting images are significantly more focused than those in Fig. 5.3. Of note, the vehicle shapes are slightly curved lengthwise that differs from its actual geometrical shape. This feature is particularly pronounced in the long truck shown in Fig. 5.4(c). It is likely the result of near-field effects, which become more prominent for a larger vehicle. A NFFFT [68] may be applied, similar to what was done in Chapter 3, to correct this effect. Overall, the results show that the final images are well focused and correspond closely to the physical dimensions of the vehicles.

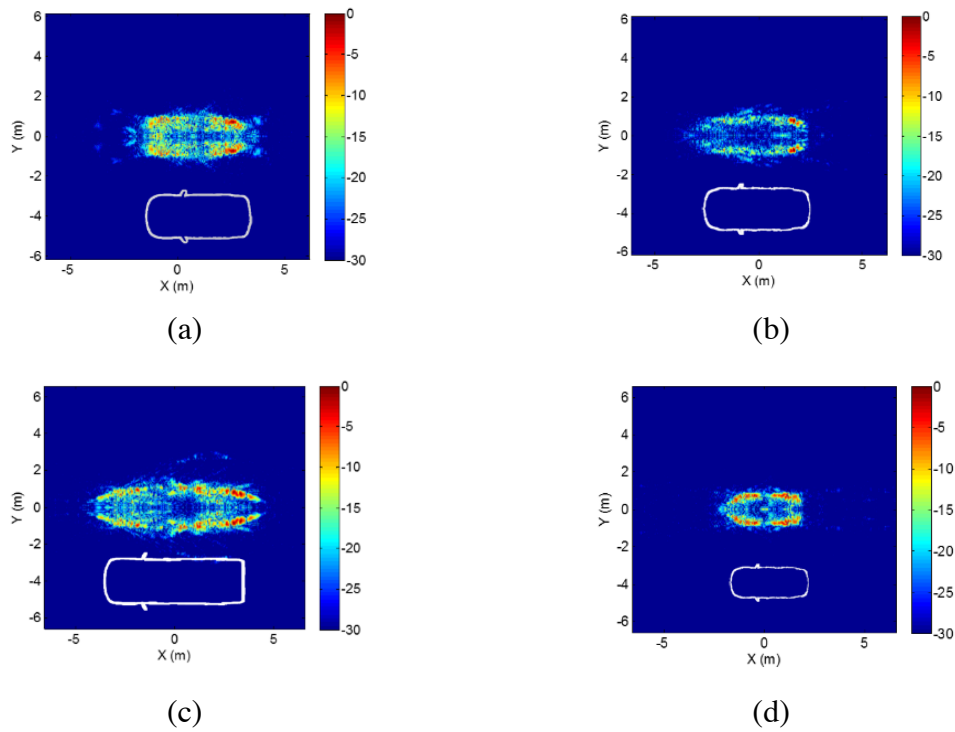


Fig. 5.4 Focused images. (a) SUV. (b) Sedan. (c) Truck. (d) Subcompact.

5.3 NON-COOPERATIVE IMAGING

Next, we investigate the realistic imaging scenario where the ranging radio data are not available and the vehicle range will need to be estimated from the measured range profile data. Due to the lack of persistent scatterers over the wide angular aperture, conventional narrow-angle ISAR focusing techniques are not applicable, since they usually assume the availability of such scatterers. However, it may be possible to estimate the vehicle geometrical center based on the measured range extent of the vehicle. Our proposed method is to align the RCS centroid of the range profiles. This estimate will replace the ranging radio data during coarse motion compensation. We test

this method on a mid-size sedan. Fig. 5.5(a) shows the measurement setup, now without the ranging radio. Fig. 5.5(b) shows the measurement vehicle.



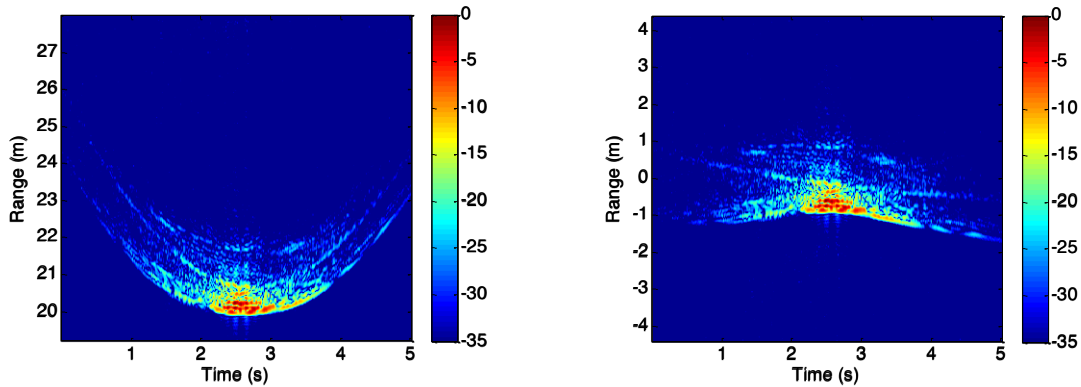
(a)



(b)

Fig. 5.5 Vehicle non-cooperative measurement synopsis. (a) Measurement collection setup. (b) Test vehicle.

Fig. 5.6(a) shows the collected raw range profiles, and Fig. 5.6(b) shows the range profiles after alignment to the RCS centroid. The measurement angle is estimated using



(a)

(b)

Fig. 5.6 Vehicle non-cooperative range alignment. (a) Raw range profile. (b) Aligned range profile.

the same inverse cosine relation, but r is now the range to the RCS centroid.

The resulting image, after coarse motion compensation, is shown in Fig. 5.7(a). An outline of the vehicle can be discerned in the ISAR image. However, better focusing is desirable. Again, we perform fine motion compensation using p -norm minimization. Here, a 3rd-order motion model is used:

$$r(t) = \sqrt{r_{\min}^2 + (a_1 t + a_2 t^2 + a_3 t^3)^2} \quad (5.2)$$

We search for the optimal a_1 , a_2 , and a_3 that minimize the p -norm, where $p = 0.8$. It was found that by driving the vehicle at a higher speed (approximately 20 mph), both the coarse and fine motion compensation performed better. The vehicles were previously driven slowly to accommodate for the ranging radio sampling rate. At higher speeds, a 3rd-order motion model was found to be sufficient. The resulting image, after fine motion compensation, is shown in Fig. 5.7(b). The image is now well focused. Note the red spot

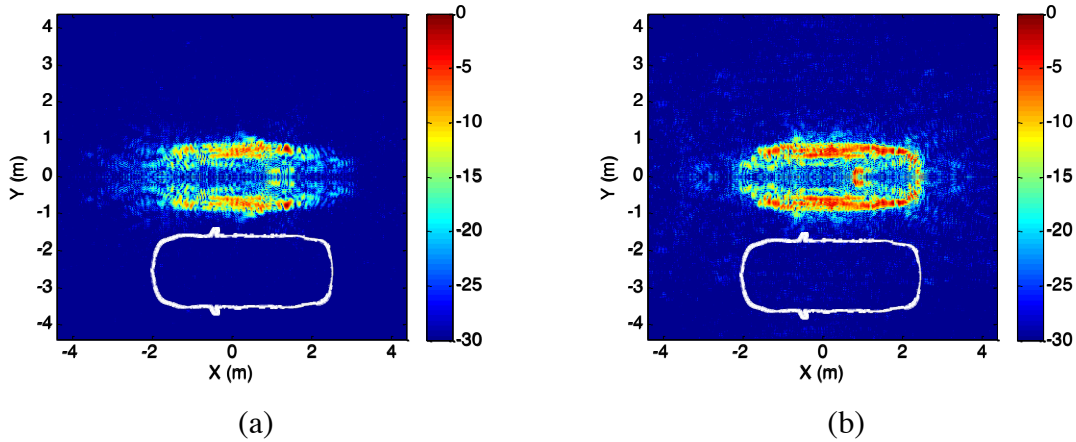


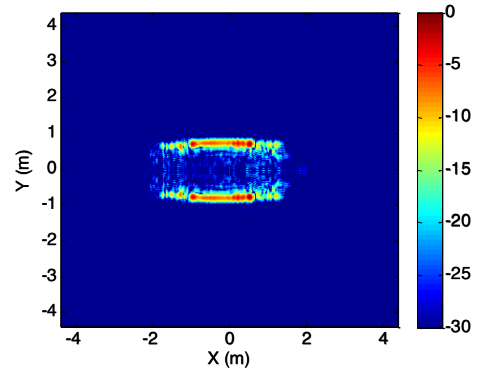
Fig. 5.7 Vehicle non-cooperative final images. (a) After coarse motion compensation. (b) After fine motion compensation.

on the roof of the vehicle slightly below $Y = 0$ in Fig. 5.7(b). This is due to two side-by-side (for increased angular coverage) corner reflectors that were placed on the roof of the vehicle. The focusing of this target in the final image further validates the result. Since we have mirrored the data in k -space, the spot also appears on the other side of the vehicle.

Finally, we examine vehicles in a real-world scenario. We place the measurement setup on the side of the road inside J. J. Pickle Research Campus and observed vehicles as they drove by. We present the resulting images of three different classes of vehicles: a subcompact, mid-size sedan, and large truck. Fig. 5.8 shows a photo of each vehicle and their resulting ISAR image. The images are well focused and reveal a clear distinction between the different-sized vehicles. It is noted that target features in the front and rear of the vehicles are lacking. Observing the vehicles over a wider angular swath could reveal more of these features. In the current data set, we were able to collect up to a 70° angular swath. Another topic is image focusing of very large vehicles, such as buses or eighteen-wheelers. Distortion to the geometrical shape of these large vehicles was noticed in reconstructed images. This may be resolved using a near-field to far-field transform or a near-field backprojection algorithm. Finally, in practice, there are additional considerations that need to be taken into account. One is when multiple nearby vehicles are in the scene. In this case, separation of these vehicles into separate targets and the effects of multiple scattering between these vehicles on the resulting image require further investigation.



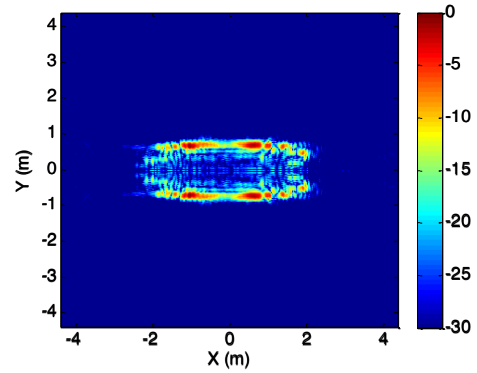
(a)



(b)



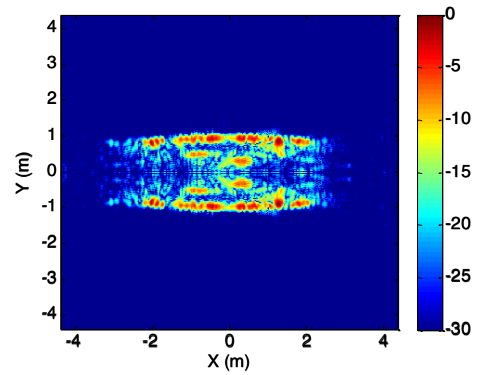
(c)



(d)



(e)



(f)

Fig. 5.8 Wide-angle ISAR imaging of different vehicles. (a) Subcompact photo. (b) Subcompact ISAR image. (c) Mid-size sedan photo. (d) Mid-size sedan ISAR image. (e) Large truck photo. (f) Large truck ISAR image.

5.4 CONCLUSION

In this chapter, wide-angle ISAR imaging of vehicles was investigated for potential applications in vehicle classification. First, baseline ISAR images were obtained in the cooperative measurement scenario with a ranging radio. The images showed a clear distinction between different-sized vehicles. The images were then further focused through motion compensation using a p -norm minimization. The resulting images were well focused and corresponded closely to the physical dimensions of the vehicles. Subsequently, we investigated the non-cooperative imaging scenario. In this case, the vehicle range was estimated based on range profile centroid. Again, p -norm minimization was then applied to further focus the images. The resulting images, in the non-cooperative scenario, were also well focused and corresponded closely to the physical dimensions of the vehicles. Thus, we have shown that motion compensation can achieve well-focused ISAR images under the in-situ, wide-angle scenario and that the resulting images are able to reveal the outline of the vehicle.

Chapter 6: Wide-Angle ISAR Imaging of Small Consumer Drones⁶

6.1 INTRODUCTION

There has been much recent interest in the use of small drones for aerial photography, surveying, mapping, and package delivery. The proliferation of these small drones has raised much recent interest in their regulation and monitoring [57-60, 74-77]. A potential way to detect and identify drones is to use ground-based radar. Analogous to the previous chapter, an ISAR image of a small drone can be generated by observing the drone as it flies across the measurement scene. However, there are several additional challenges that need to be overcome in order to obtain a wide-angle ISAR image of a small consumer drone: (i) the small size and low reflectivity of the plastic body may result in a very low radar cross section, (ii) the spinning blades of the drone may result in significant dynamic signature features similar to other rotorcraft [77, 82, 83], and (iii) the potentially unsteady flight of a typical drone may complicate motion compensation, making image formation more challenging.

To address the first two challenges (and decouple them from the third challenge), we conduct laboratory measurements of several small consumer drones and examine their radar signatures versus frequency, aspect, polarization, etc. The radar signatures are presented in the form of ISAR images, as they provide not only information about the strength of the radar cross section of a target, but also the spatial locations of the dominant scattering on the drone. While ISAR imaging is a standard technique for radar diagnostics and larger military drones have been extensively studied [78-81], we believe this is the first ISAR measurement study for these consumer-type drones. To address the third challenge, we leverage our understanding of turbine and vehicle ISAR imaging

⁶ C. J. Li and H. Ling, "An investigation on the radar signatures of small drones," accepted for publication in *IEEE Antennas Wireless Propag. Lett.*, 2016.

Chenchen Jimmy Li was the primary author for all content in the above publication.

from previous chapters in order to carry out in-situ, high-resolution ISAR imaging of small drones from a stationary ground radar.

This chapter is organized as follows. First, we examine the drones in a controlled, laboratory setting. The measurement setup is first described before the resulting ISAR images are presented and the scattering features are discussed. We begin with a baseline scenario before deviating from this scenario to illustrate the effects of frequency, aspect, polarization, dynamic blade rotation, camera mount, and drone types. Afterwards, we proceed to the in-situ measurement. The measurement setup and motion compensation algorithm are first described before the resulting ISAR images are presented.

6.2 LABORATORY MEASUREMENT SETUP AND POST-PROCESSING

Multi-frequency, multi-aspect, monostatic backscattered data are measured from a drone mounted on a turntable in the laboratory. Fig. 6.1(a) shows the measurement setup. A vector network analyzer (Agilent N5230A) is used to collect S_{11} data. Depending on the frequency range, either a Ku-band standard gain horn (Narda 4609, 12-18 GHz) or a dual-ridged horn (TDK HORN-0118, 1-18 GHz) is used. Background subtraction is used to reduce the horn input mismatch and background clutter. Fig. 6.1(b) shows one of the target drones, the DJI Phantom 2 [84], with zero azimuth angle (AZ) and zero elevation angle (EL) defined as the frontal view. Data are collected at two frequency bands, 12-15 GHz and 3-6 GHz. A 3 GHz bandwidth is chosen to provide higher resolution.

We briefly review the post-data processing since it has been covered in previous chapters. The sinogram (i.e. range profiles vs. aspect) is obtained through the inverse Fourier transform of the frequency response at each aspect after a Hamming window is applied. A 2-D ISAR image of the drone is obtained by using the k -space formulation



Fig. 6.1 (a) Drone ISAR collection setup. (b) DJI Phantom 2 with GoPro camera [84].

presented in Chapter 2. Since the collected data are uniformly sampled in frequency and angle, a polar reformatting is applied to interpolate the data onto a uniform k_x - k_y grid first. The ISAR image can then be obtained via a 2-D IFFT of the backscattered field. A 2-D Hamming window is applied to the interpolated data before the IFFT to reduce image sidelobes. Each ISAR snapshot is obtained using a 12.7° angular swath for the data from 12-15 GHz and 38.1° for the data from 3-6 GHz. These angular windows are chosen to achieve an equal down-range and cross-range resolution of 5 cm (without windowing). Finally, an 18 cm-radius calibration sphere is measured to calibrate the results in terms of absolute RCS in dBsm.

6.3 MEASUREMENT RESULTS: DJI PHANTOM 2

6.3.1 Baseline Scenario

First, we examine the results for a baseline scenario, viz. DJI Phantom 2 from 12-15 GHz with the blades stationary, without a camera mounted, using vertical polarization

on transmit and receive, and azimuth scan at zero elevation angle. The resulting sinogram is shown in Fig. 6.2(a). It can be seen that the majority of the backscattered signal is confined within a 35 cm range extent. This agrees with the diagonal width of the drone. Additional returns beyond 17.5 cm in down-range are likely due to multiple scattering, but they are not prominent.

Figs. 6.2(b)-(f) show the ISAR images at $AZ = 8^\circ, 45^\circ, 90^\circ, 135^\circ,$ and 172° , respectively. These angles are defined by the central AZ angle of each angular window. Thus, Fig. 6.2(b) is the ISAR image at 8° to the left of the exact frontal view. The geometrical outline of the drone in its proper orientation is overlaid onto each ISAR image for comparison. In addition, the highest RCS level is marked in each figure. Note that due to the small size of the drone, there are fewer than 7 resolution cells in either the down-range or cross-range dimensions over the drone. Through the sequence of images, five main scattering mechanisms are revealed. The strongest scattering feature is shown in Fig. 6.2(d) where the AZ angle is at 90° (or the broadside view of the drone). Here, the strongest scattering is located at the center of the drone and can be attributed to the battery pack of the drone, which is a rectangular cuboid with a “bulge” at the tail end, as shown in the geometrical outline. At the broadside view, the largest surface area of the battery pack is perpendicular to the radar line of sight (RLOS). At -9.3 dBsm, this is the highest RCS level over all azimuth angles. Overall, the battery pack return is prominent at the cardinal angles and much weaker elsewhere. The four other scattering mechanisms are due to the four drone motors. Their returns are visible except when shadowed. The full ISAR movie can be found online [85]. It is clear that the ISAR images are more insightful than the sinogram since they reveal the 2-D spatial locations of the scattering features.

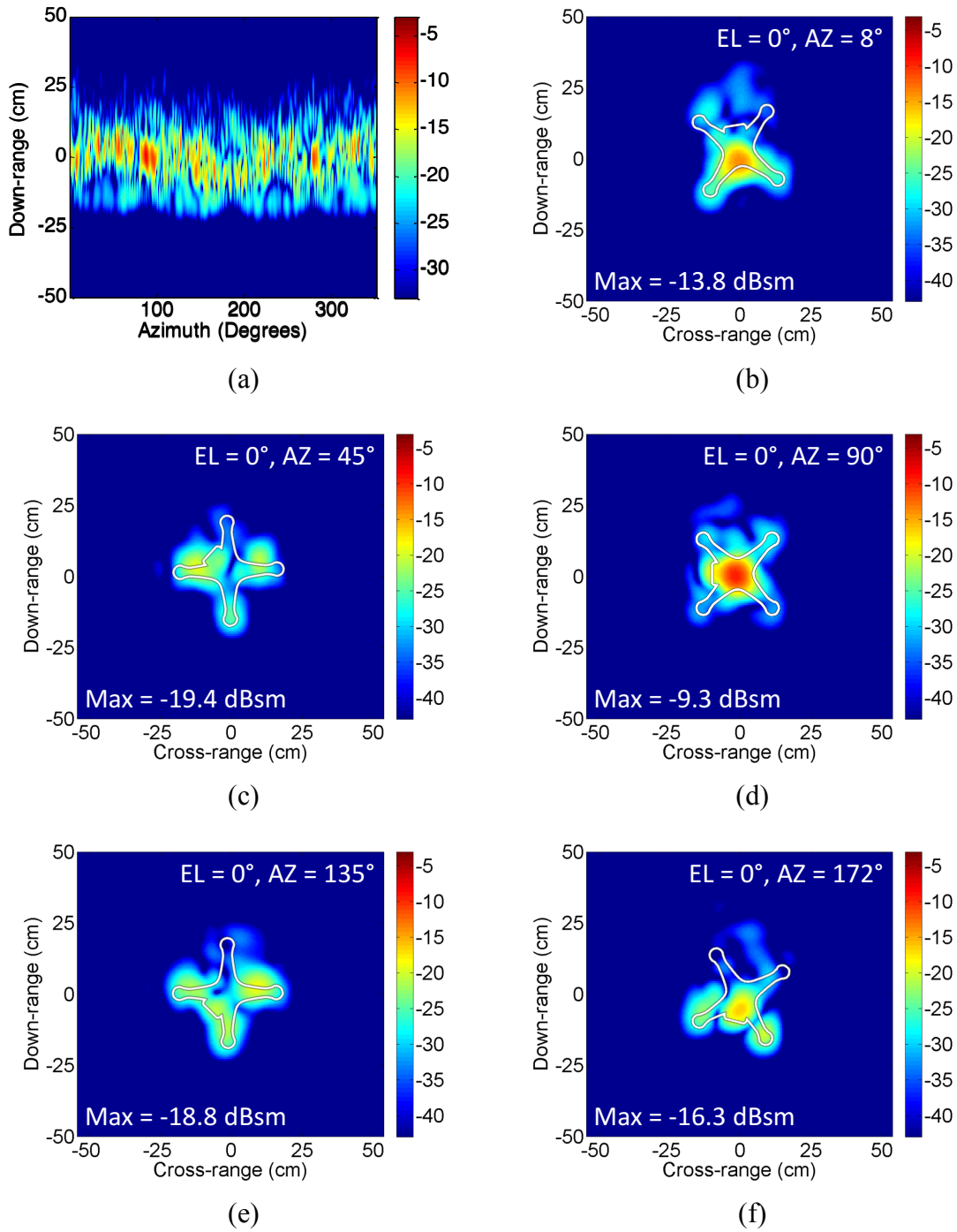


Fig. 6.2 DJI Phantom 2 baseline scenario. (a) Sinogram. (b)-(f) ISAR image at 8° , 45° , 90° , 135° , 172° respectively.

6.3.2 Effect of Rotating Blades

Next, we deviate from the baseline scenario by repeating the measurement with the plastic blades rotating at their minimum speed (which does not create sufficient lift for flight). There are no observable differences from the baseline scenario in either the sinogram or the ISAR images over all azimuth angles. A side-by-side ISAR image comparison with the baseline scenario at 102° AZ is shown in Fig. 6.3 to illustrate this observation. Thus, the spinning blades do not create any noticeable dynamic features in the radar signature within the 40 dB dynamic range. This is consistent with the fact that the stationary blades were not visible in the ISAR images in the static-blade scenario. It should be noted that these blades can be seen in a continuous-wave (CW) Doppler measurement using the VNA, where the drone is stationary and only the blades are spinning. Nonetheless, the blade returns are faint. They could be enhanced if the plastic blades are replaced with carbon-fiber blades.

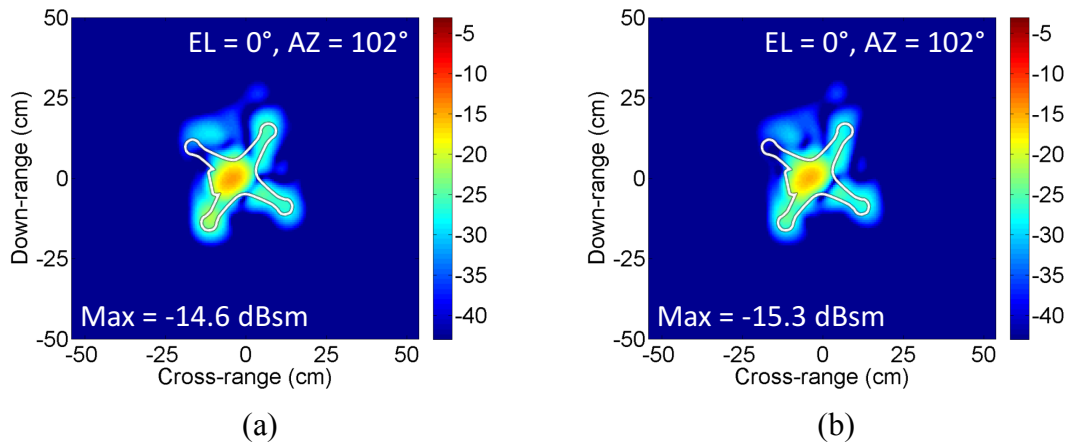


Fig. 6.3 Effect of rotating blades. (a) Baseline scenario (static blades). (b) Rotating blades scenario.

6.3.3 Effects of Polarization

We change the polarization from vertical to horizontal on transmit and receive. A side-by-side ISAR image comparison with the baseline scenario at 6° AZ is shown in Fig. 6.4. By switching to horizontal polarization, the return strength from the battery pack has decreased but the return strength from the drone motors have increased. Of note, the plastic blades (stationary or spinning) of the drone are still not visible under horizontal polarization.

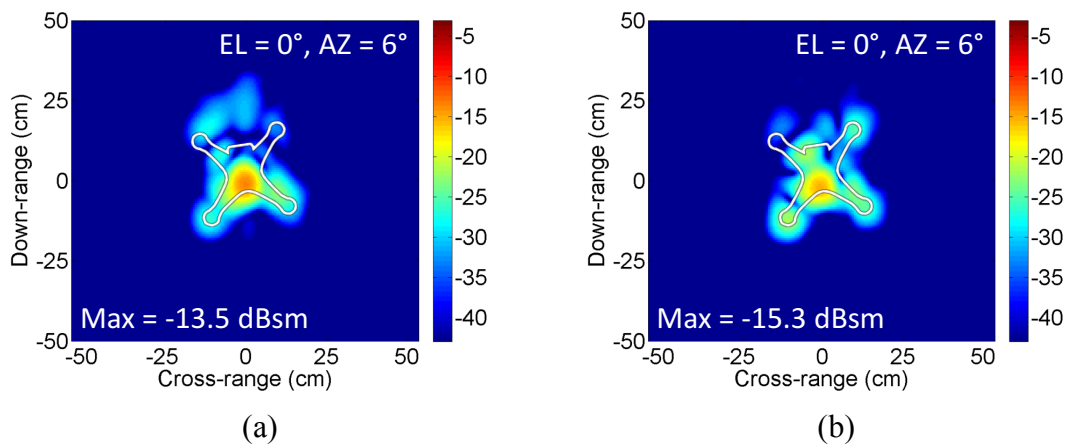


Fig. 6.4 Effects of horizontal polarization. (a) Baseline scenario (vertical polarization). (b) Horizontal polarization scenario.

6.3.4 Effects of Mounted Camera

Next, we mount a GoPro HERO4 camera to the base of the drone. A side-by-side ISAR image comparison with the baseline scenario at 60° AZ is shown in Fig. 6.5. The camera return is indicated by the arrow in Fig. 6.5(b). In fact, this aspect is where the mounted camera is most prominent. For most azimuth angles, it is found that the results are not significantly different from those of the without-camera case. The camera is

mounted below the battery pack. Thus, its return, in general, will coalesce with the battery pack returns when illuminated at a zero elevation angle.

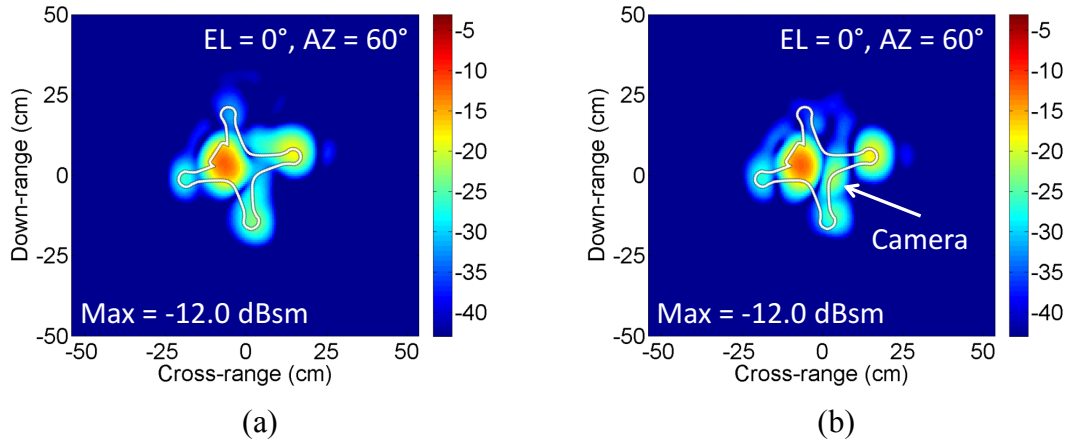


Fig. 6.5 Effects of a mounted camera. (a) Baseline scenario (no camera). (b) Mounted camera scenario.

6.3.5 Effects of Frequency Change

Next, we change the frequency range in the measurement from 12-15 GHz to 3-6 GHz. A side-by-side ISAR image comparison with the baseline scenario at 194° AZ is shown in Fig. 6.6. The maximum RCS in Fig. 6.6(b) has decreased by 10.3 dB in comparison to Fig. 6.6(a). When averaged over all azimuth angles, the maximum RCS level is 11.6 dB lower at the 3-6 GHz band in comparison to that at 12-15 GHz band. Multiple scattering also appears more prominent at the lower frequency band.

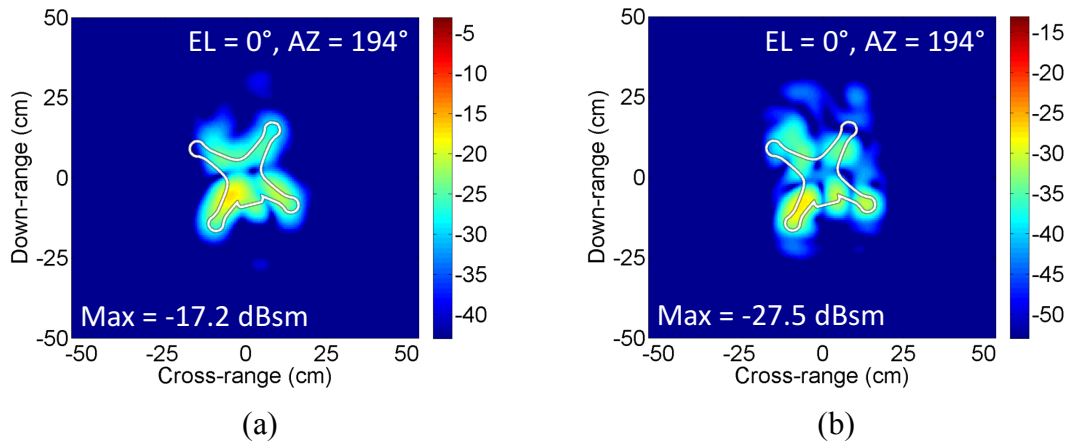


Fig. 6.6 Effects of frequency change. (a) Baseline scenario (12-15 GHz). (b) 3-6 GHz scenario.

6.3.6 Elevation Scan

Finally, an elevation scan of the drone is collected at the zero azimuth angle at 12-15 GHz. Vertical polarization is used on transmit and receive. Fig. 6.7(a) shows an ISAR image with the angular window centered at -90° EL. This corresponds to the scenario where the radar observes the drone flying by directly overhead and results in a side-view

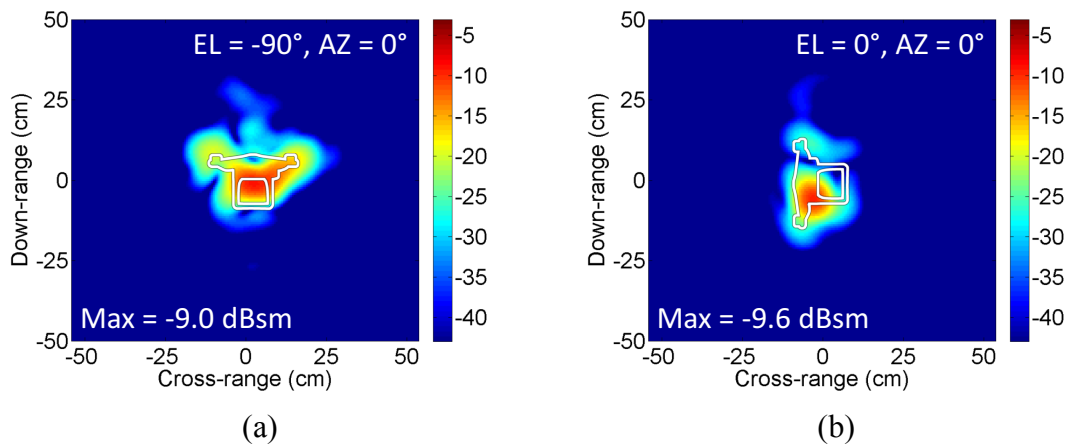


Fig. 6.7 Elevation scan. (a) ISAR image centered at -90° elevation. (b) ISAR image centered at 0° elevation.

image of the drone. Fig. 6.7(b) shows an ISAR image with the angular window centered at 0° EL. Unlike the previous azimuth-scan scenarios where the length and width of the drone are captured, these elevation-scan images capture the length and height of the drone.

6.4 MEASUREMENT RESULTS: LARGER DRONES

Next, we examine two larger drones: the 3DR Solo (shown in Fig. 6.8(a) with a 46 cm diagonal width [86]) and the DJI Inspire 1 (shown in Fig. 6.8(d) with a 56 cm diagonal width [87]). We present the results of each at both the 12-15 GHz and 3-6 GHz band, using vertical polarization on transmit and receive, azimuth scan at zero elevation angle, and with the blades stationary.

The resulting ISAR images for the 3DR Solo at broadside are shown in Figs. 6.8(b) and 6.8(c) for 12-15 GHz and 3-6 GHz, respectively. Again, the geometrical outline of the drone in its proper orientation is overlaid onto each ISAR image for comparison. The ISAR image shows that the dominant returns are due to the drone battery pack and its four motors. It is clear from the image that the Solo is larger than the Phantom 2. The maximum RCS shown at the broadside view, -14.1 dBsm, is the maximum RCS level over all azimuth angles. Interestingly, despite the larger size, this is about 5 dB lower than the Phantom 2. This may be attributed to the different shape of the Solo and its battery pack. Similar to the Phantom 2, the overall RCS is weaker by approximately 10 dB in the 3-6 GHz band in comparison to that at 12-15 GHz. Multiple scattering also appears more prominent in the lower band.

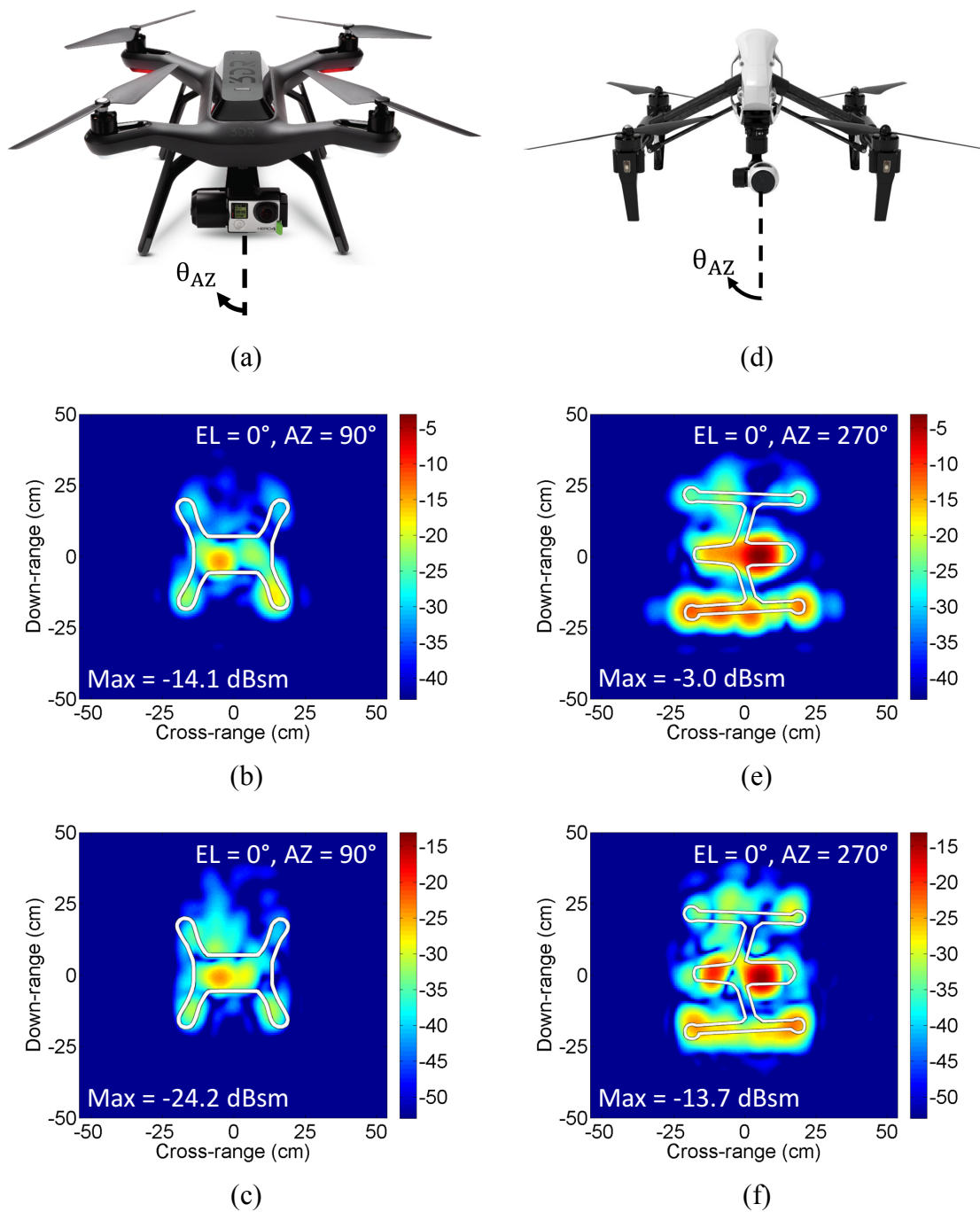


Fig. 6.8 (a) 3DR Solo [86]. (b) Solo ISAR image at 90° (12-15 GHz). (c) Solo ISAR image at 90° (3-6 GHz). (d) DJI Inspire 1 [87]. (e) Inspire 1 ISAR image at 270° (12-15 GHz). (f) Inspire 1 ISAR image at 270° (3-6 GHz).

The ISAR images of the DJI Inspire 1 at broadside are also shown in Fig. 6.8. Fig. 6.8(e) shows the result for 12-15 GHz, and Fig. 6.8(f) shows the result for 3-6 GHz. In this case, in addition to the drone battery pack and rotor motors, the horizontal frame of the Inspire 1 has a large contribution to the drone return. The large size of the drone is also reflected in the ISAR images. The maximum RCS at the broadside view, -3 dBsm, is again the highest RCS level over all azimuth angles and is due to the drone battery pack. Analogous to the other two drones, in the 3-6 GHz band, the overall RCS has decreased by about 10 dB and multiple scattering is more prominent.

In summary, we have addressed the first two challenges posed in the introduction. First, while the overall RCS of these small drones are low, the resulting ISAR images still revealed the size and geometrical outlines of each drone. Second, it has also been shown that the plastic drone blades do not contribute a significant return (while stationary or spinning) in comparison to the rest of the drone body.

6.5 IN-FLIGHT MEASUREMENT

To address the third challenge, we proceed to in-situ measurement using the Time Domain radar. The target is a DJI Phantom 3 Advanced [88]. The exterior shape of the Phantom 3 is nearly identical to that of the Phantom 2. The main advantage of the Phantom 3 Advanced over the Phantom 2 is that the flight logs, which include Global Positioning System (GPS) coordinates and altitude, can be extracted from the drone. Additionally, in the Phantom 3 Advanced, GPS is combined with the Global Navigation Satellite System (GLONASS) to achieve higher accuracy than GPS alone. The availability of the flight logs provides a ground truth for motion compensation. Thus, we

compare the ISAR images generated through blind motion compensation with the images generated using GPS-assisted motion compensation.

6.5.1 In-Flight Measurement Setup

In-situ, in-flight measurements of a small consumer drone are taken using the P440 radar on the ground. A single dual-ridged horn (TDK HORN-0118, 1-18 GHz) is used for both transmit and receive through the use of a circulator. Vertical polarization is used on transmit and receive. Range profiles are collected as the Phantom 3 (without camera) is flown in a straight line, at approximately 9 m away from the radar, across the measurement scene. The sampling rate for consecutive range profiles is set to 100 Hz. Three different flight paths are taken in order to generate both an azimuth and elevation scan of the drone. The azimuth scan is generated by flying the drone horizontally across the measurement scene at a low height. Two elevation scans are generated by observing the drone as it flies directly overhead the radar and by observing the drone during takeoff. Fig. 6.9 shows the measurement setup with the measurement equipment on the left and the Phantom 3 Advanced on the right. Note, the measured data are not calibrated in terms of absolute radar cross section level but are instead normalized to the maximum value.



Fig. 6.9 Drone in-flight measurement setup.

6.5.2 Image Formation

As with Chapter 5, we apply motion compensation in two parts. First, coarse motion compensation is applied to align the magnitude of the range profiles. This is done using the same methodology from the previous chapter. One set of collected range profiles are shown in Fig. 6.10(a). The range profiles, after coarse range alignment are shown in Fig. 6.10(b).

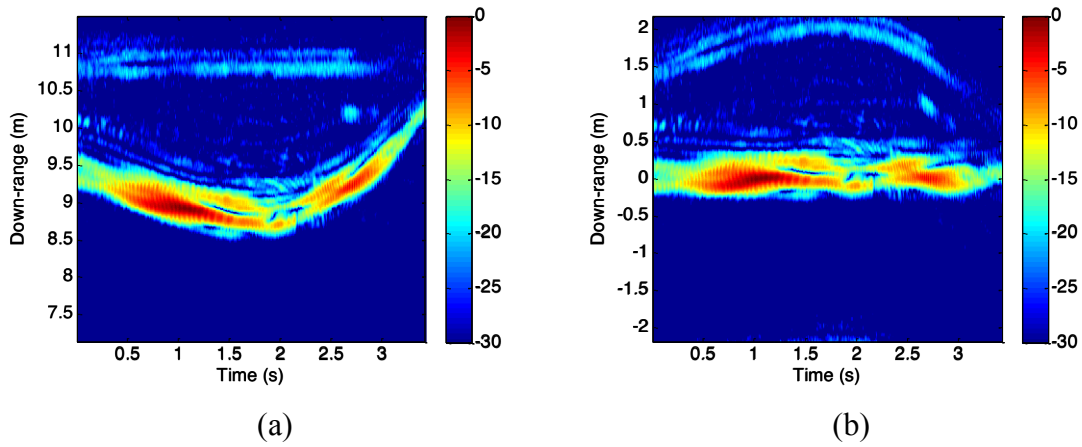


Fig. 6.10 Drone in-flight range profiles. (a) Before coarse motion compensation. (b) After coarse motion compensation.

After the coarse motion compensation, fine motion compensation is applied. The spectrogram at the center frequency, after coarse alignment, is shown in Fig. 6.11(a). Examining the spectrogram, there is a single dominant feature that is fairly persistent. This allows for alignment using the Doppler information [6, 11]. Although it is possible to use the same methodology from the previous chapter for fine motion compensation, we found the following approach produced better results:

$$A(n) = \sum_{n=1}^N f_d(n)\Delta t \quad (6.1)$$

$$E_{aligned}^s(n, f) = E^s(n, f)e^{-j2\pi A(n)\frac{f}{f_c}} \quad (6.2)$$

where $A(n)$ is the alignment offset of the n th time bin, $f_d(n)$ is the value of the Doppler frequency of the dominant feature in the n th time bin, and Δt is the time sampling interval (in this case 10 ms). The above equations align the Doppler of the RCS centroid. Since the Doppler is the derivative of range, we can integrate the Doppler to obtain the necessary fine range alignment. The spectrogram before and after fine motion compensation are shown in Fig. 6.11. After both coarse and fine range alignment, ISAR snapshots are formed using a 26° angular swath to achieve equal down-range and cross-range resolution in the image.

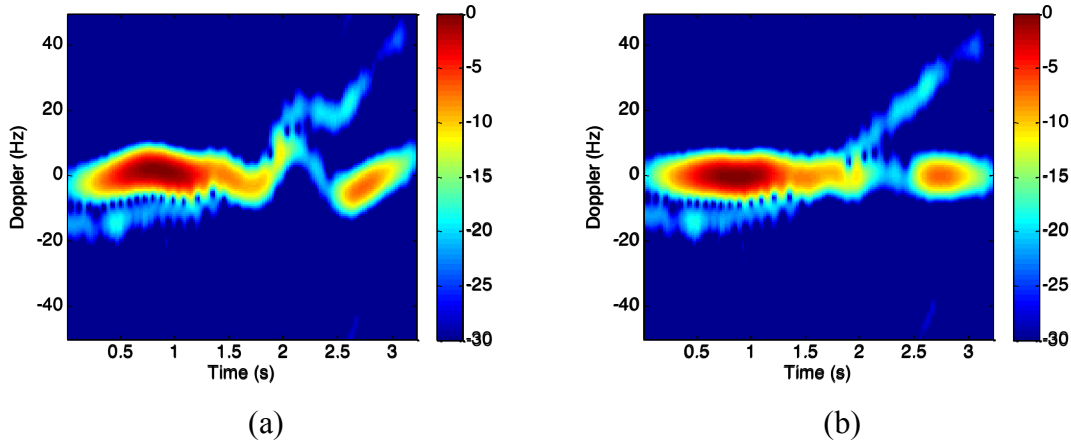


Fig. 6.11 Drone in-flight spectrogram (a) Before fine motion compensation. (b) After fine motion compensation.

For the GPS-assisted motion compensation, alignment is performed by calculating the relative distance between the radar and the drone for each instance in time. In order to obtain the relative distance from the flight logs, the drone is placed at the location of the radar prior to flight. Thus, the coordinates of the radar are known.

6.5.3 Results: Azimuth Scan

The drone is flown horizontally across the measurement scene at approximately 1.8 m above the ground. The resulting imaging plane is similar to the azimuth scan from the laboratory measurement at 0 EL. There are two minor differences between the laboratory measurement and the in-situ measurement. First, there is a slight elevation angle since the dual-ridged horn rests on the tripod at approximately 1.5 m above the ground. Second, the drone tilts slightly forward during flight. The resulting ISAR images are shown in Figs. 6.12(a)-(c). The ISAR images generated using GPS-assisted motion compensation are also shown in Figs. 6.12(d)-(f). The geometrical outline of the drone in its proper orientation is overlaid onto each ISAR image for comparison.

Comparing the two sets of ISAR images, the blind motion compensation appears to perform better than the GPS-assisted motion compensation. The ISAR images after blind motion compensation are slightly more focused, and the drone remains in the center of the ISAR image. Due to inaccuracies in the GPS, the target in the ISAR images after GPS-assisted motion compensation may be shifted from the center (which is particularly evident in Fig. 6.12(f)). Overall, while the resulting images were well focused in cross-range, the narrower bandwidth (compared to laboratory measurement) of the radar and the limited number of distinct scatterers on the drone make it challenging to accurately discern the shape of the drone.

6.5.4 Results: Elevation Scan

The drone is observed by the radar over two different flight paths. First, the drone is observed as it is flown directly overhead the radar. This captures an image similar to that of Fig. 6.7(a). Second, the drone is observed as it takes off from the ground. This captures an image similar to that of Fig. 6.7(b). The resulting ISAR images are shown in Fig. 6.13, where Fig. 6.13(a) is from the overhead flight and Fig. 6.13(b) is from the

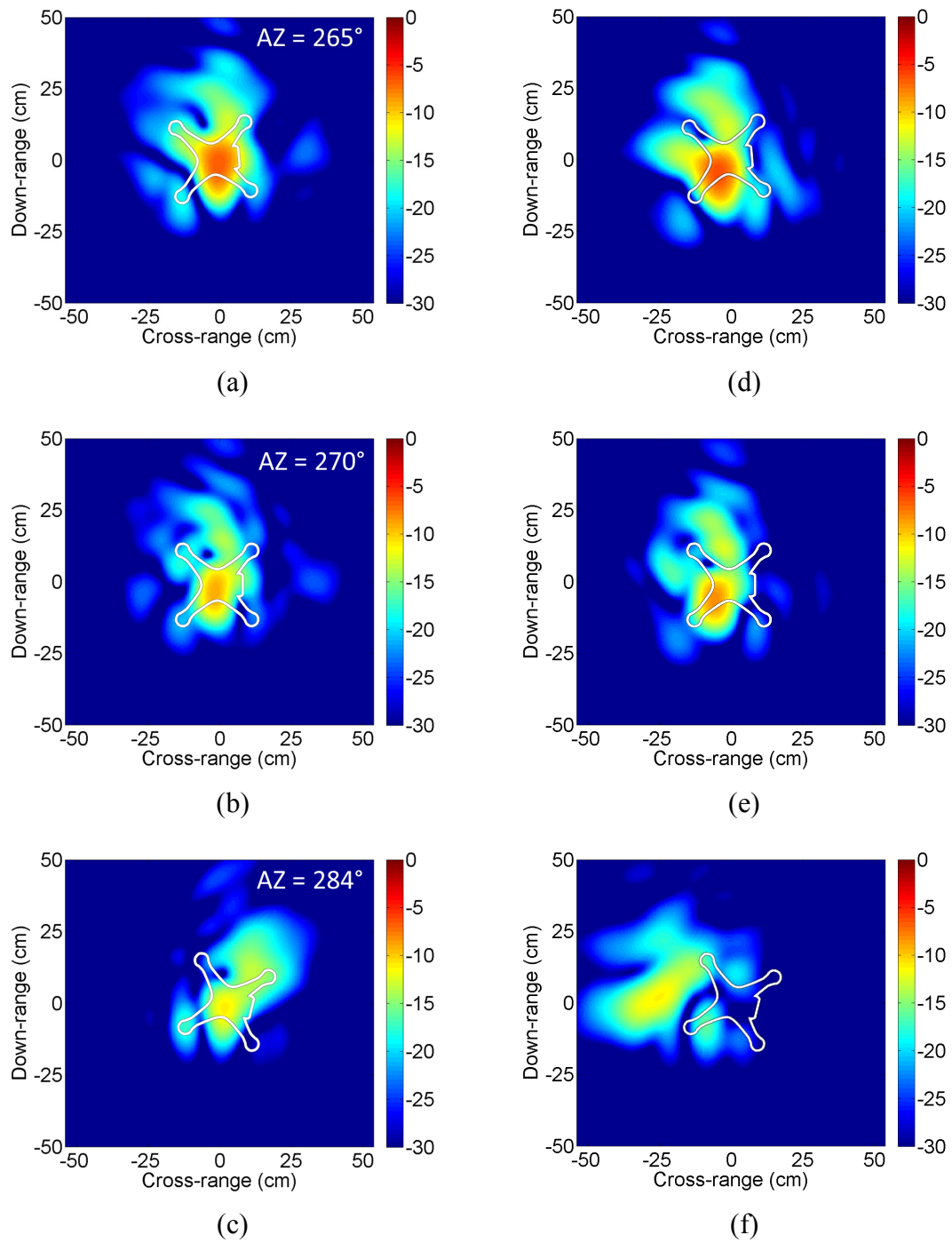


Fig. 6.12 In-flight ISAR images: azimuth scan. (a)-(c) Blind motion compensation. (d)-(f) GPS-assisted motion compensation.

takeoff. For comparison, the GPS-assisted images are also shown in Figs. 6.13(c)(d). Again, the geometrical outline of the drone in its proper orientation is overlaid onto each ISAR image for comparison. Again, the blind motion compensation performs better than the GPS-assisted motion compensation. In Fig. 6.13(c) in particular, due to GPS inaccuracies, the GPS-assisted motion compensation was unable to generate a focused image. Akin to the azimuth scan results, the in-situ ISAR images are focused but it is challenging to discern the shape of the drone. Of note, the Phantom 3 is 18 cm tall and 25

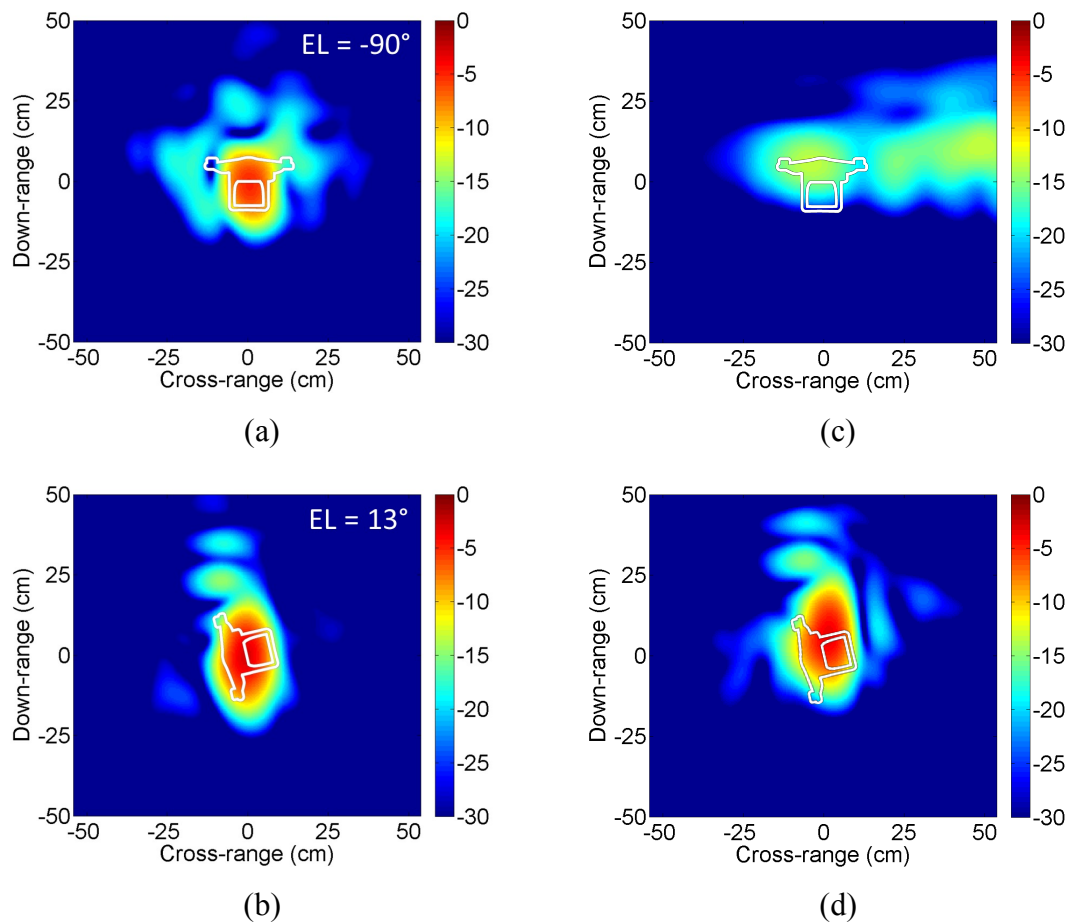


Fig. 6.13 In-flight ISAR images: elevation scan. (a)(b) Blind motion compensation. (c)(d) GPS-assisted motion compensation.

cm wide from the side view. Thus, the target is roughly only 3 range cells wide in either dimension due to the 2 GHz bandwidth of the radar.

6.5.5 Inspire 1 Measurement

Finally, we present the in-situ ISAR images of an Inspire 1 in flight. Blind motion compensation is used to form the two azimuth scan ISAR images in Fig. 6.14. A comparison between Fig. 6.14(a) and Fig. 6.8(f), which was formed based on turn-table data, shows the striking similarity between the two images. The size difference between the Inspire 1 and Phantom 3 is also clearly reflected in the ISAR images.

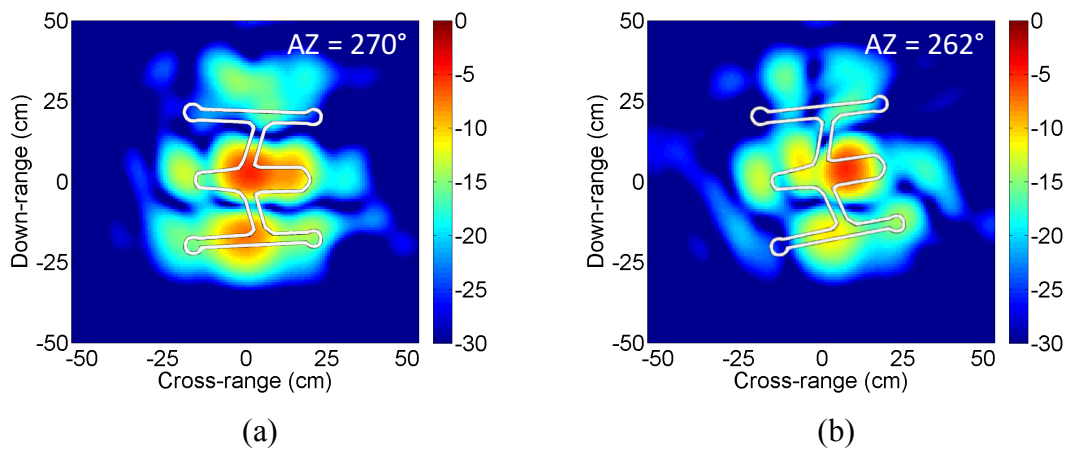


Fig. 6.14 In-flight ISAR images of Inspire 1. (a) AZ = 270°. (b) AZ = 262°.

6.6 CONCLUSION

In this chapter, we have presented a measurement study of the radar signatures of several consumer drones. The results show that the non-plastic portions of the drones (battery pack, motors, carbon fiber frame, etc.) dominate their radar signatures. It has also been shown that the plastic drone blades do not contribute a significant return (while stationary or spinning). While the overall radar cross section level is low, the resulting

laboratory ISAR images reveal the size and geometrical outlines of each drone. Subsequently, we generated the ISAR images of consumer drones in flight using a stationary ground radar. Due to the narrower bandwidth of the radar and the limited number of distinct scatterers on the drone, in-situ identification of the drone is more challenging. However, preliminary in-situ measurement data show that classification based on the radar images of these drones may be feasible.

Chapter 7: Wide-Angle SAR Imaging Using a Small Consumer Drone^{7,8}

In this chapter, we depart from the theme of the previous chapters on generating an ISAR image of a moving target from a stationary UWB radar. Instead, we take advantage of the portable and lightweight Time Domain UWB radar and mount it on a small consumer drone to carry out aerial SAR imaging of the ground.

7.1 INTRODUCTION

There has been much recent interest in the use of small drones for aerial photography. This raises the possibility of using such small drones for aerial SAR imaging, which can offer complementary information to optical imagery. The use of large unmanned aerial vehicles (UAV) for SAR imaging is, of course, well established [89-91]. The use of low-cost portable drones for radar imaging could open up other potential applications in scientific, agricultural, environmental, and structural health monitoring. In this work, a low-cost SAR system mounted on a small consumer drone is developed and demonstrated. The imaging system is comprised of a UWB radar connected to an on-board single-board computer. The radar is remotely controlled from a laptop on the ground through a Wi-Fi connection. The setup is mounted on the bottom of the small drone (see Fig. 7.1). By flying the drone across the measurement scene, range profiles are collected continuously across different look angles of the scene. The data are then post-processed via motion compensation into focused SAR images. Both the side-looking and the downward-looking SAR scenarios are presented.

⁷ C. J. Li and H. Ling, "Synthetic aperture radar imaging using a small consumer drone," in *Proc. IEEE Antennas Propag. Int. Symp.*, Vancouver, Canada, pp. 685-686, Jul. 2015.

⁸ C. J. Li and H. Ling, "High-resolution, downward-looking radar imaging using a small consumer drone," presented at *IEEE Antennas Propag. Int. Symp.*, Fajardo, Puerto Rico, Jun. 2016.

Chenchen Jimmy Li was the primary author for all content in the above publications.

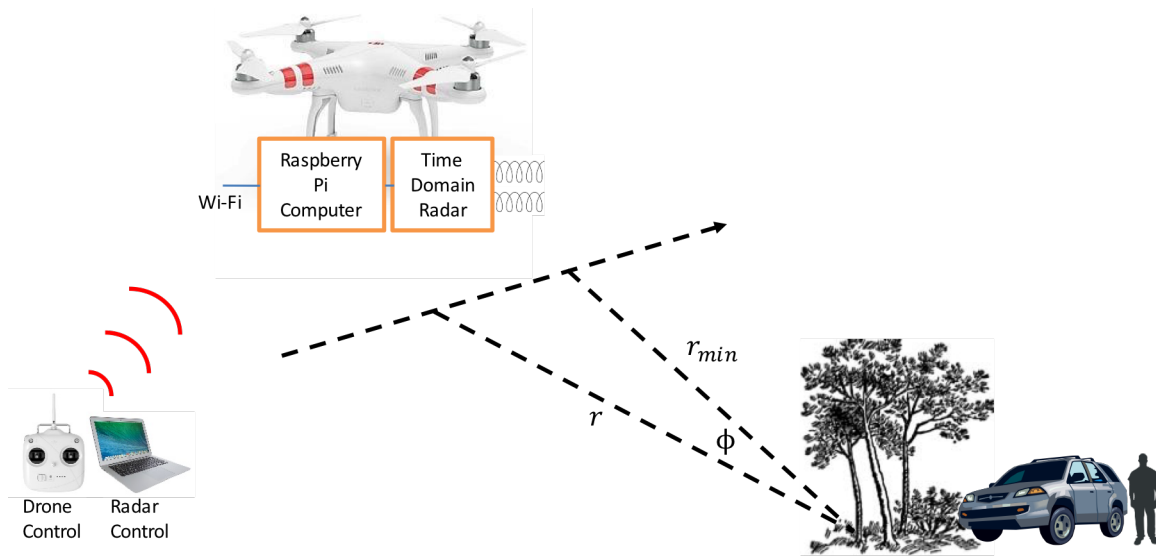


Fig. 7.1 Drone-SAR system and measurement setup.

7.2 SIDE-LOOKING SAR MEASUREMENT SYNOPSIS

The system consists of the P410 radar, two antennas, a single-board computer with Wi-Fi capability, and a consumer drone. Two 5-turn helix antennas are used for transmit and receive. The radar sampling rate for consecutive range profiles is set at 20 Hz to provide sufficient pulse integration and range coverage. The radar is controlled via a Raspberry Pi Model B with a Wi-Fi dongle and is given instructions from a laptop over Wi-Fi. The entire system (including batteries and cables) weighs less than 300 g and is mounted to a DJI Phantom 2 drone. Range profiles are collected by flying the drone across the scene in a straight line (at approximately 2 m above the ground). The closest approach, r_{min} , is approximately 7.5 m. Fig. 7.1 shows a diagram of the measurement setup. Range profiles are collected over a distance of approximately 8 m or 60° of angular swath. Fig. 7.2 shows two photos of the drone-SAR system from two different perspectives.

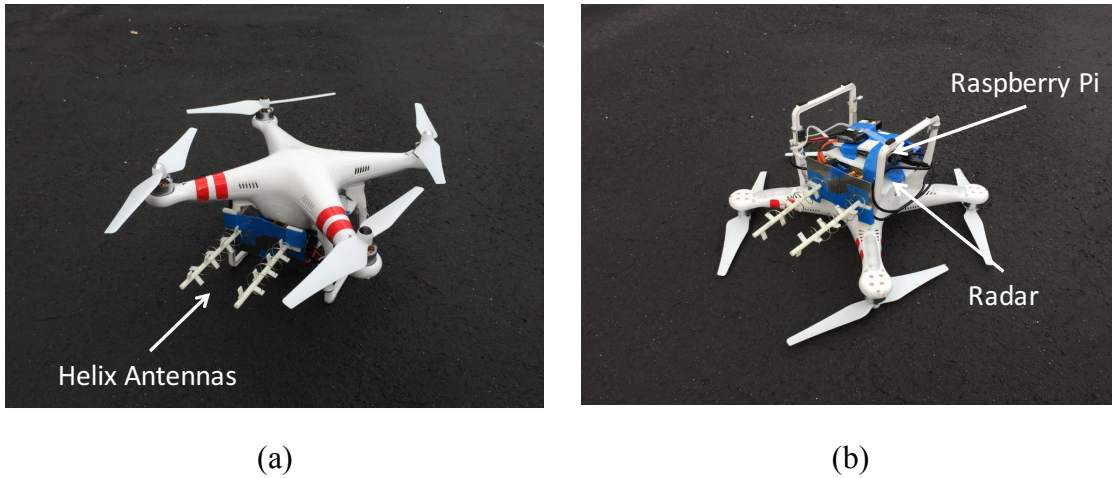


Fig. 7.2 Drone-SAR system on the Phantom 2 drone. (a) Top-down view. (b) Belly-up view.

To replace the bulky horns used in previous measurements, two 5-turn helix antennas were designed for a center frequency of 4.3 GHz. The mold was created using 3-D printing, and 18-AWG wire was used to create the helix. One right-hand circularly polarized and one left-hand circularly polarized helix are constructed to account for the polarization reversal upon reflection. Each helix is mounted on an aluminum ground plane. Fig. 7.3(a) shows the measured reflection coefficient, and Fig. 7.3(b) shows the

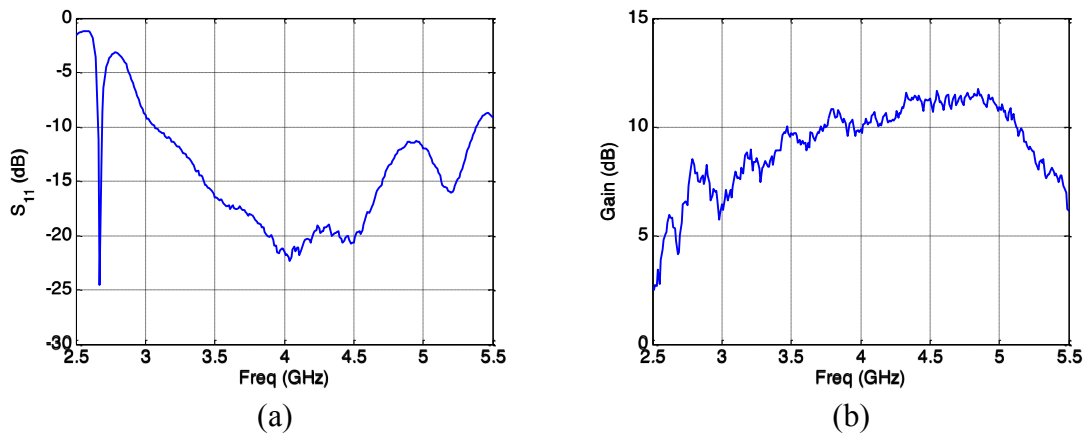


Fig. 7.3 Helix antenna measurement. (a) Reflection coefficient. (b) Gain.

measured gain of the helix. Finally, the measured two-way 3 dB beamwidth is roughly 15° .

7.3 IMAGE FORMATION

For calibration and testing, four trihedrals (16 cm per side) are placed on the ground in a rhombus configuration with 3 m diagonals. Fig. 7.4 shows a photo of the scene. Fig. 7.5(a) shows the measured range profiles vs. flight time. The four tracks in the plot correspond to the four trihedrals in the scene. As expected, the tracks exhibit significant range migration due to the wide collection angular swath. Fig. 7.5(b) shows the simulation result based on a point-scatterer model under a constant velocity flight. The same range tracks are observed. To form an image from the data, translational motion compensation is carried out by alignment to a prominent point-scatterer [2]. Fig. 7.5(c) shows the range profiles after range alignment to the closest trihedral. The center of rotation is now located at the closest scatterer. Again, good agreement with the aligned simulated range profiles in Fig. 7.5(d) is observed. Next, we perform rotation motion compensation to focus the scatterers located away from the rotation center. To



Fig. 7.4 Drone-SAR measurement scene with 4 trihedrals.

accomplish this, we estimate the azimuth angle of the radar with respect to the rotation center and then apply k -space imaging (as discussed earlier in Chapter 2). To relate measurement time with the azimuth angle ϕ , we assume the flight path is straight and use the relationship $\phi = \cos^{-1}(r_{min}/r)$, where r is the range at each instance in time, and r_{min} is the minimum range (see Fig. 7.1).

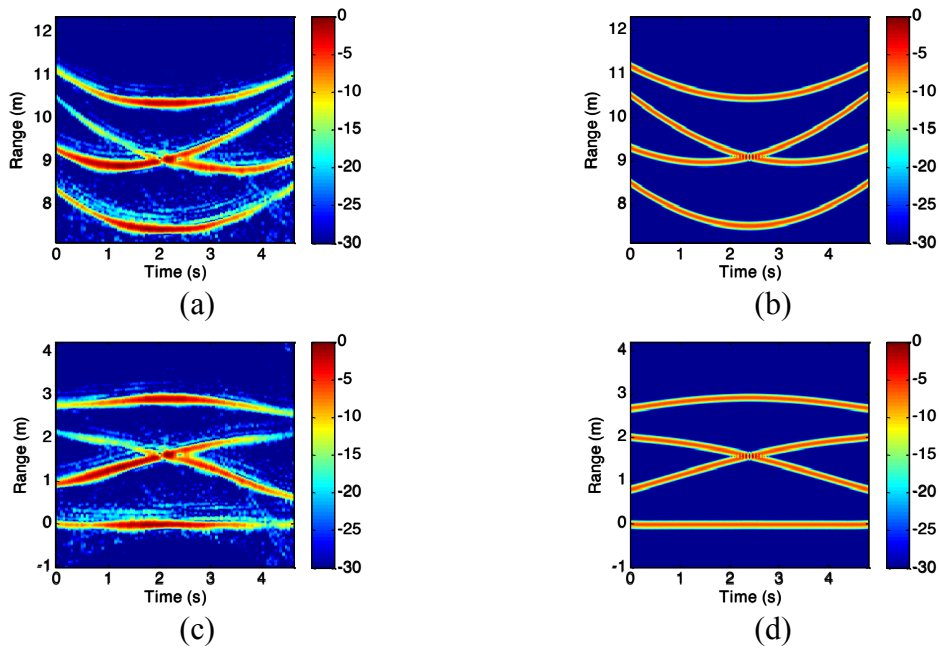


Fig. 7.5 (a) Measured range profiles vs. flight time from 4 trihedrals on the ground collected from the drone-SAR. (b) Simulated range profiles based on a point-scatterer model and constant velocity flight. (c) Aligned measured range profiles. (d) Aligned simulated range profiles.

7.4 SIDE-LOOKING SAR RESULTS

Fig. 7.6(a) shows the resulting SAR image based on the simulated point-scatterer data shown in Fig. 7.5(d). Three of the point-scatterers are well focused but the farthest point-scatterer exhibits some cross-range smearing. This is verified to be caused by near-

field effects due to the closeness of the targets from the radar. Next, as an intermediate step, we mount the drone on a rail and smoothly move it along the measurement path. The resulting image is shown in Fig. 7.6(b). There is good agreement with the simulation; three of the trihedrals are well focused while the farthest trihedral exhibits some cross-range smearing. Finally, Fig. 7.6(c) shows the resulting SAR image from the drone flying along the measurement path. Other than the closest reference trihedral, the other trihedrals are less focused compared to Fig. 7.6(b) since the drone flight is not as smooth. Nonetheless, four trihedrals in their correct locations can be seen in the SAR image.

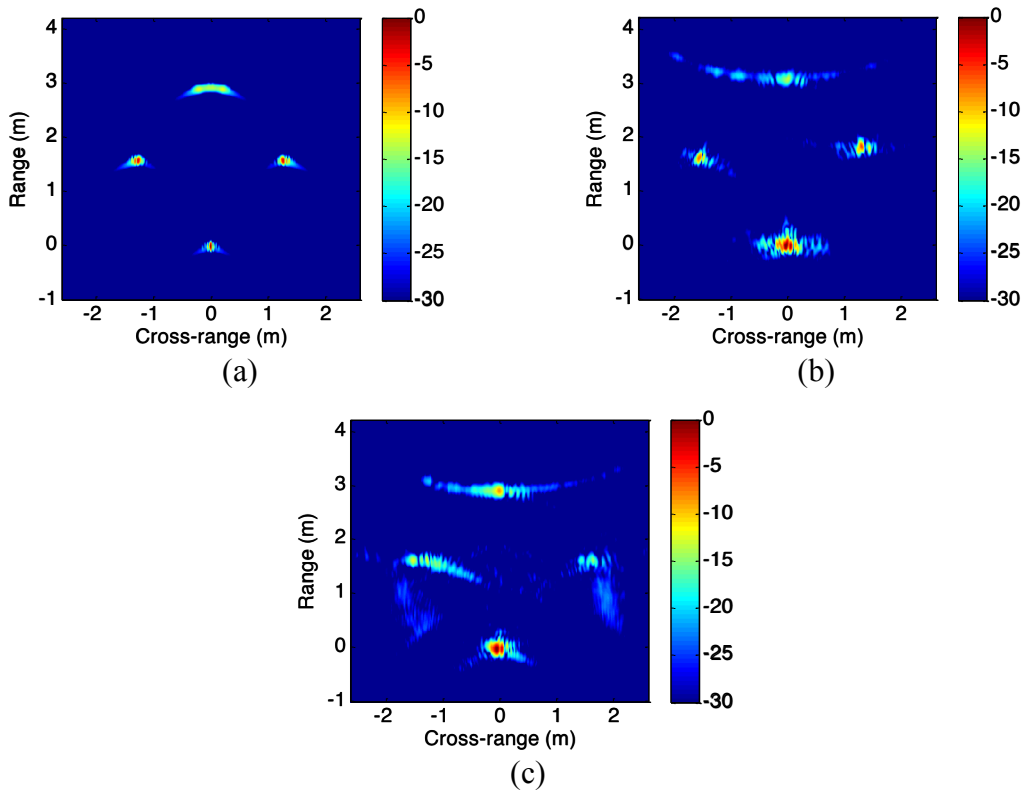


Fig. 7.6 (a) Simulated SAR image. (b) Measured SAR image with drone on rail. (c) Measured drone-SAR image.

One solution to correct the near-field effect is implementing the same NFFFT as done with the utility-class wind turbine. However, the NFFFT requires the data to be

uniformly sampled in angle. Since the measured data is not uniformly sampled in angle, interpolation would be required before a NFFT. An alternative approach is to use a near-field backprojection algorithm [67]. Here, we have implemented near-field backprojection using the following:

$$SAR(r, cr) = \frac{1}{NM} \sum_{n=1}^N \sum_{m=1}^M E_s(x_n, f_m) \times e^{j \frac{4\pi f_m}{c} \sqrt{(cr-x_n)^2 + (r+y_o)^2 + z_o^2}} \quad (7.1)$$

where r is range, cr is cross-range, x_n is the n^{th} position of the drone flight path, y_o is the distance of the closest approach, and z_o is the height of the drone flight. Fig. 7.7 provides an illustration of this scenario. In essence, for each range, cross-range pixel in the SAR image, we calculate the distance from the radar and phase compensate the measured scattered field data. By summing this over all frequencies and angles, we arrive at the final image.

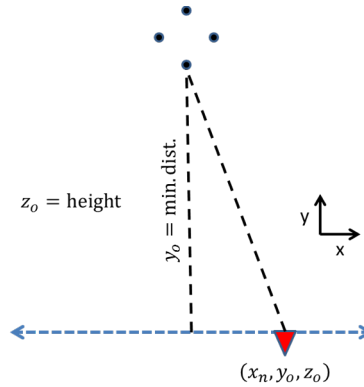


Fig. 7.7 Measurement scenario for near-field backprojection.

The resulting near-field corrected SAR images are shown in Fig. 7.8. It is seen from Fig. 7.8(a) that image blurring due to the near-field effect has been removed. This correction is also carried over to the measurement data in Figs. 7.8(b) and 7.8(c). Again,

there is good agreement between the rail-SAR, and the drone-SAR results are slightly more blurred since the drone flight is not as smooth.

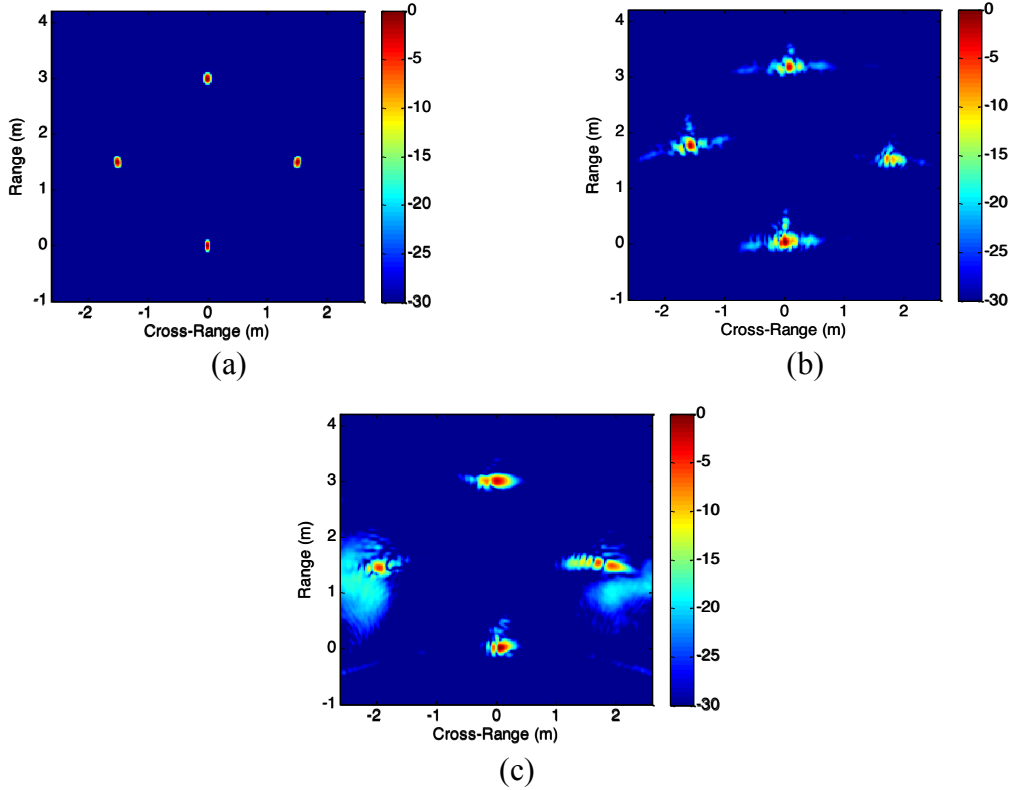


Fig. 7.8 SAR images after near-field backprojection. (a) Simulated. (b) Rail-SAR. (c) Drone-SAR.

SAR images of other targets can also be formed by flying radar on the drone across the measurement scene. Here, we form SAR images of a parked vehicle from two different perspectives. A trihedral is left in the scene for reference. Fig. 7.9(a) shows a photo of one orientation of the vehicle, and Fig. 7.9(b) shows the resulting SAR image. Fig. 7.9(c) shows a photo of the vehicle in another orientation, and Fig. 7.9(d) shows the resulting SAR image. The focused point in front is the reference trihedral. In agreement with Chapter 5, the predominant contribution comes from the side panel of the car in Fig.

7.9(b). However, if the orientation of the side panel is tilted relative to the radar, such as in the case of Fig. 7.9(d), other features of the vehicle become more visible.

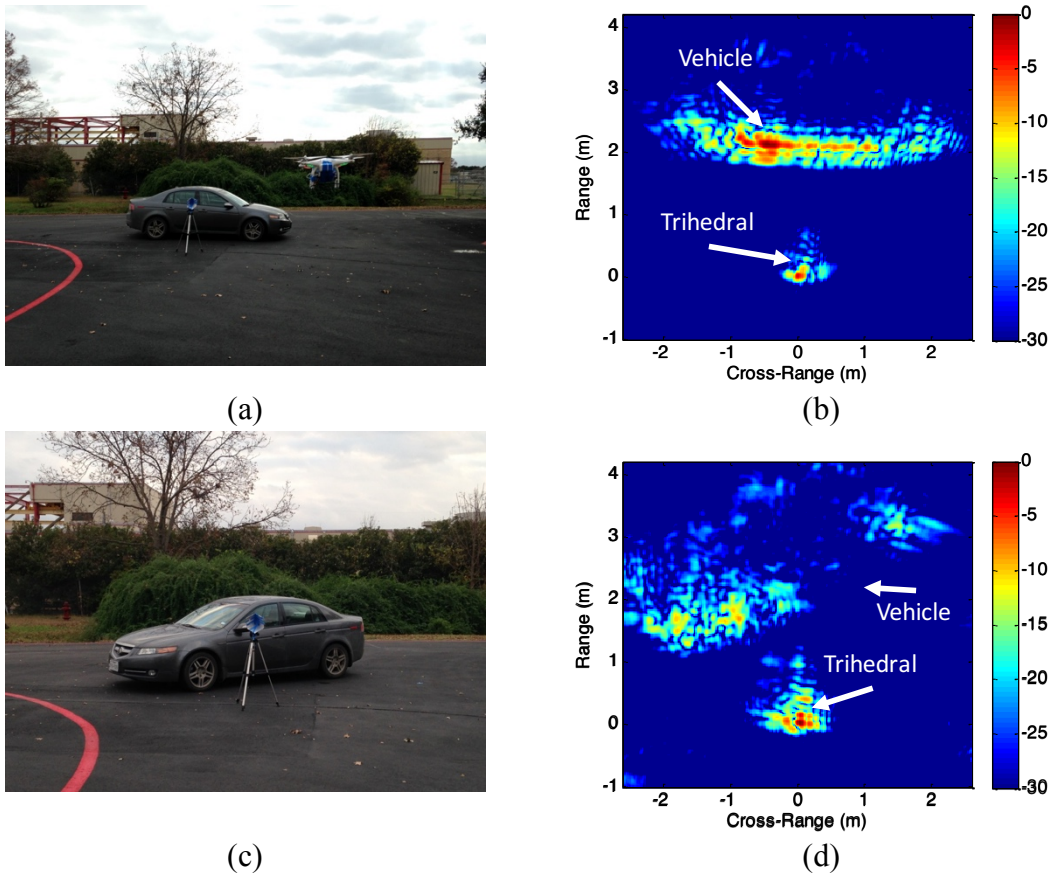


Fig. 7.9 Drone-SAR image of a vehicle. (a) Photo of orientation 1. (b) SAR image of orientation 1. (c) Photo of orientation 2. (d) SAR image of orientation 2.

7.5 DOWNWARD-LOOKING SAR MEASUREMENT SYNOPSIS

For situations where a drone can fly directly over the scene of interest, the downward-looking mode should also be feasible. In this section, an optical and radar system are combined to operate concurrently in the downward-looking mode while mounted on a small drone. The system is the same as before, but now the helix antennas

are pointed downward. Furthermore, the on-board, single-board computer has been upgraded to the Raspberry Pi 2 and an optical camera has been added. By flying the drone directly overhead the measurement scene, range profiles are collected in conjunction with optical video. The radar range profile sampling rate and video frame rate are both set at 25 Hz. The results of several sample measurements scenes are presented and discussed.

The measurement system and setup is illustrated in Fig. 7.10 where the range profiles and video are collected by flying the drone directly overhead the measurement scene in the downward-looking mode. Three measurement scenes are examined: a row of six trees, a row of four vehicles in a parking lot, and two humans standing in a parking lot.

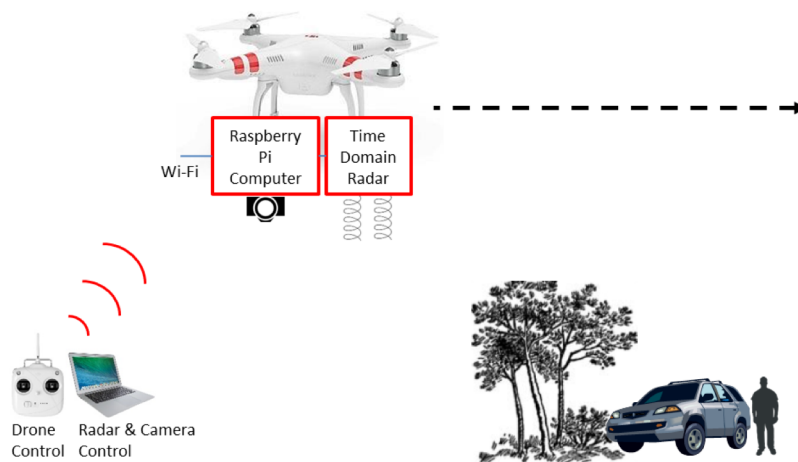


Fig. 7.10 Drone measurement system and setup.

7.6 DOWNWARD-LOOKING SAR RESULTS

A row of six trees of varying heights is surveyed. A side-view of the measurement scene is shown in Fig. 7.11(a), and an aerial snapshot of tree 3 from the drone is shown in

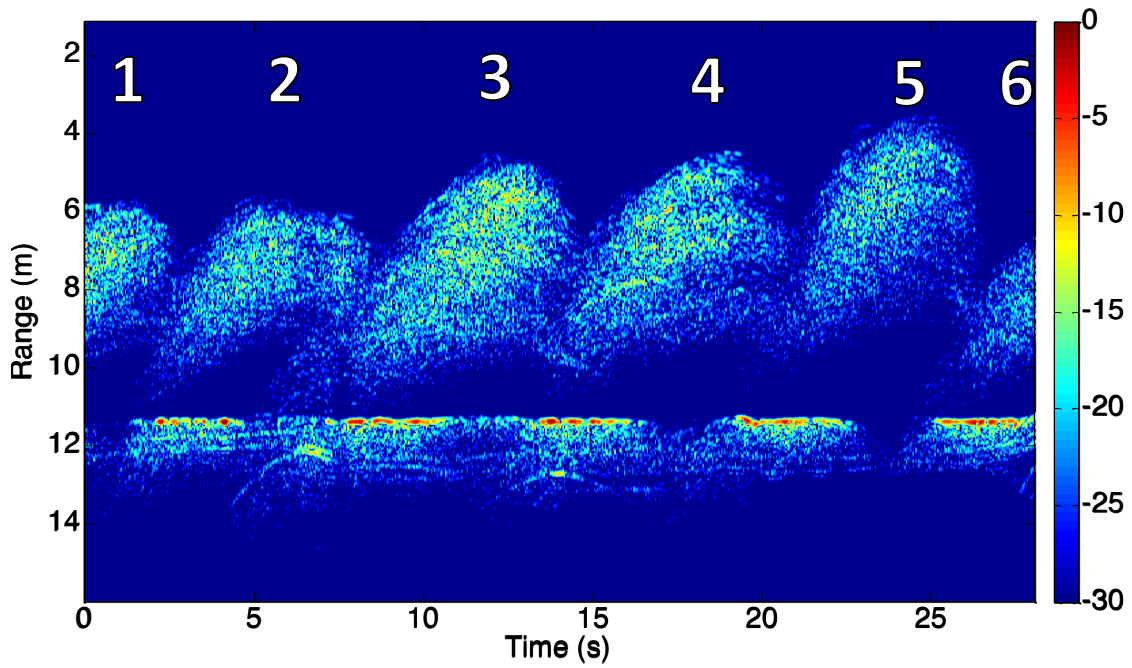
the inset of the figure (where one of the helix antennas is visible). The collected range profiles vs. time are shown in Fig. 7.11(b). Altitude variations during the drone flight are corrected using the ground returns. Due to shadowing from the tree canopies, the ground returns are not persistent. Thus, a smoothing spline is used to curve fit the ground returns and align the range profiles. The ground returns, after alignment, form the horizontal line at about 11.5 m in range. From the range profiles, the tree canopy returns are clearly observed. The height information of each tree follows the same trend as that shown in Fig. 7.11(a). Significant penetration into the tree canopy, on the order of several meters, is observed. Some radar wave penetration into the soil can also be seen.

Next, a row of four different parked vehicles is examined. A side-view of the measurement scene is shown in Fig. 7.12(a), and an aerial snapshot of vehicle 1 is shown in the inset of the figure. Vehicle 1 is a grounds maintenance cart, vehicle 2 is a minivan, and vehicles 3 and 4 are sports utility vehicles. The collected range profiles are shown in Fig. 7.12(b). Here, the ground returns have been aligned at 4.7 m in range. Due to shadowing from each vehicle, the ground returns are not persistent. The height of each vehicle can be determined from the range profiles. In this case, the heights of all four vehicles are roughly the same. For vehicle 1, the track with a vertex at approximately 3 m in range is due to the roof of the cab of the vehicle, while the track with a vertex at approximately 4 m in range is due to the rear bed of the vehicle.

Lastly, two people in different poses are examined. A side-view of the measurement scene is shown in Fig. 7.13(a), and an aerial snapshot of person 2 is shown in the inset of the figure. The collected range profiles are shown in Fig. 7.13(b). The

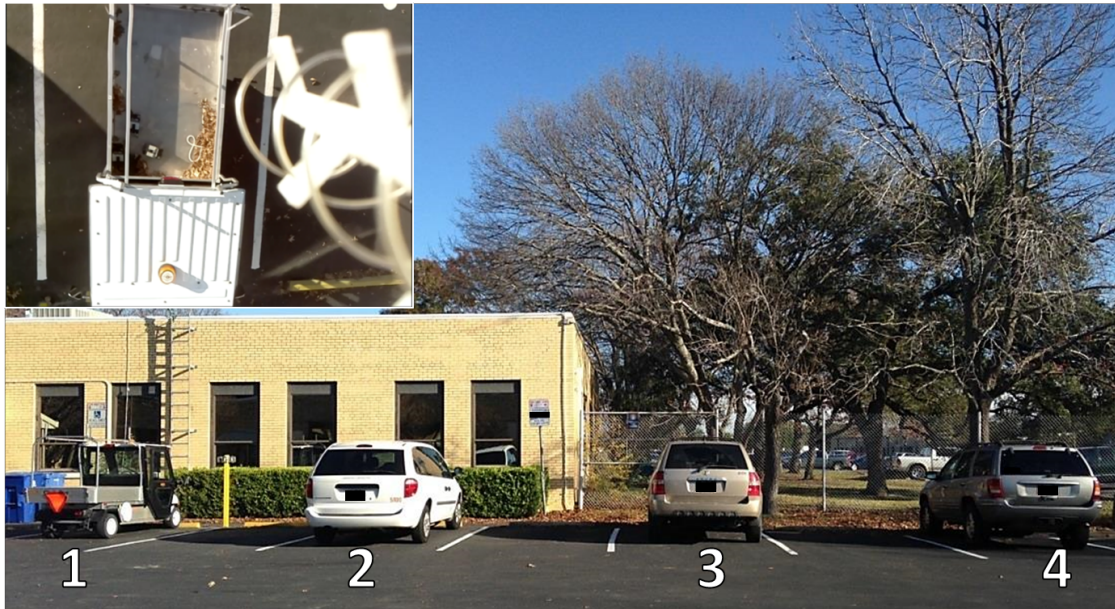


(a)

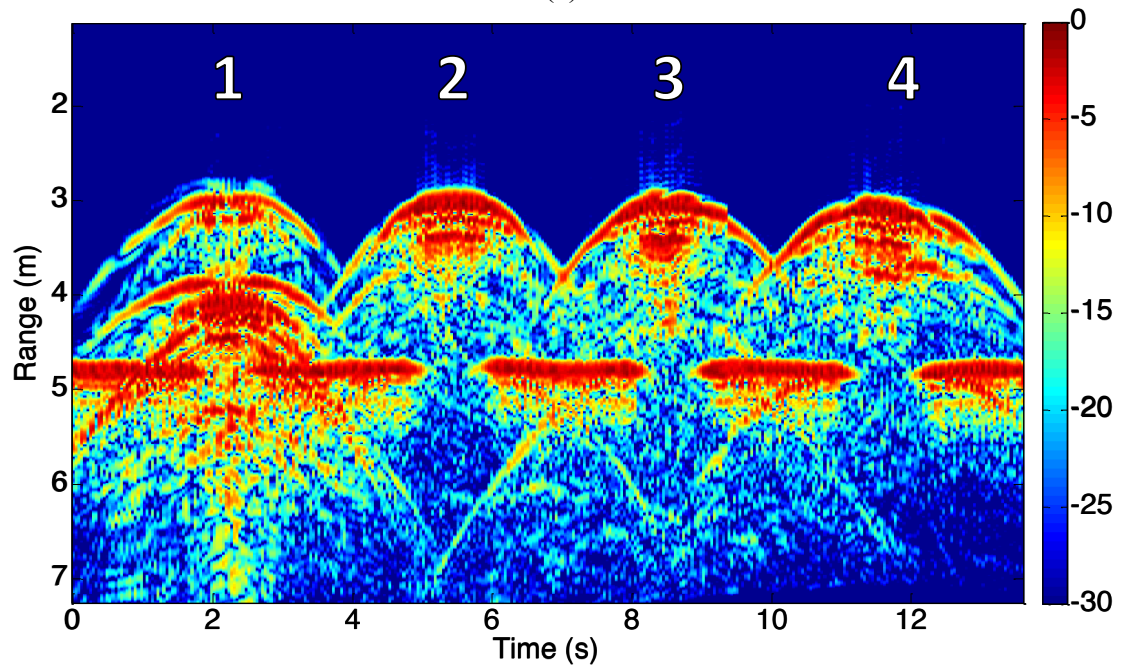


(b)

Fig. 7.11 Measurement of trees. (a) Photograph. (b) Range profiles.



(a)



(b)

Fig. 7.12 Measurement of vehicles. (a) Photograph. (b) Range profiles.

ground returns, which are persistent throughout in this case, have been aligned at 5.2 m. The two tracks that have a vertex around 3.4 m are due to the head of each person and indicate the height of each person. For person 1, the strong returns about 50 cm below the head return are due to a laptop held at chest level. For person 2, the strong returns about 25 cm below the head return are due to the outstretched arms and shoulders. Overall, the strength of the returns is weaker than that from vehicles.

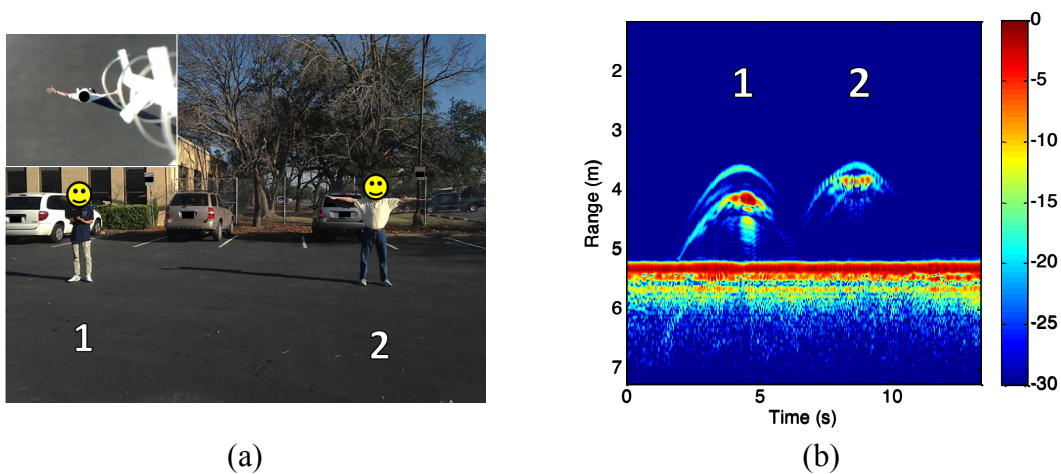


Fig. 7.13 Measurement of humans. (a) Photograph. (b) Range profiles.

Since there is no reference trihedral in the scene, motion compensation needs to be done using positioning information from the drone itself. This may be done by mounting the drone-SAR system to the Phantom 3 Advanced and downloading the GPS data, via USB, after the flight. Thus, it should be possible to further focus the collected range profiles along the flight direction, thus generating a frontal-view SAR image [2]. This is a possible topic for future work.

7.7 CONCLUSION

In this chapter, we have developed a low-cost, drone-based SAR system and demonstrated its SAR imaging performance. The entire system including the radar, the antennas, and a single-board computer fits on a small consumer drone and can be controlled through a Wi-Fi connection. To generate a focused SAR image, accurate motion compensation is required. A focused SAR image of four trihedrals on the ground was formed using drone-collected measurement in the side-looking mode. SAR images of a vehicle, in two different orientations, were also shown. Subsequently, we switched to the downward-looking mode, where concurrent optical and radar data are collected. Three drone-collected measurement sets were shown and discussed. The resulting radar data contain information about the scene that is not always obvious in the optical imagery.

Chapter 8: Conclusion and Future Work

8.1 CONCLUSION

A state-of-the-art UWB radar was used to investigate and demonstrate in-situ, high-resolution radar imaging of dynamic targets. On its own, the high-resolution range profiles collected by the radar can be considered one-dimensional, high-resolution radar images of the target. In this dissertation, we fulfilled the true potential of UWB radar imaging by generating two-dimensional, high-resolution radar images of the target through wide-angle synthetic aperture data collection and processing. Three challenging classes of moving targets were investigated: wind turbines, vehicles, and small consumer drones. In addition to being of current interest, these targets have vastly different sizes. Their electrical sizes ranged from more than one thousand wavelengths to less than five wavelengths at the operating frequency of the radar. As a result, we had to deal with scenarios in which the target was large enough such that the maximum Doppler extent posed sampling rate challenges and scenarios in which the target was small enough such that it posed SNR and image resolution concerns. In such a way, the necessary measurement, simulation, and post-processing methodologies to form focused imagery for these cases were established. High-resolution radar imaging of these targets were then demonstrated and the technical limitations evaluated.

In Chapter 3, the measurement and processing methodologies to capture the in-situ ISAR image of an operating horizontal-axis wind turbine was developed. The methodologies were first tested and validated on a small wind turbine. Motion compensation and image formation algorithms were implemented to generate a well-focused ISAR image. Results were compared to those generated using physical-optics simulation, and good agreement between measurement and simulation was observed. It was shown that the resulting ISAR images provided revealing geometrical insight on the

blade scattering phenomenology that is not as apparent in either the range profile or Doppler spectrogram alone. The same methodologies were then applied to a larger 18-blade windmill and a 1.7 MW utility-class wind turbine. In the latter case, additional near-field effects due to the maximum range limit of the radar were encountered. They were corrected using a near-field to far-field transform, and the inner portion of the turbine blades was successfully imaged.

In Chapter 4, following the horizontal-axis wind turbine work, a vertical-axis wind turbine was investigated. First, measurement and physical-optics simulation were carried out for a 1.5 m model to validate the physical-optics prediction. The underlying scattering physics of the observed features from the blade, strut, and tower structures was discussed. It was shown that physical optics was also sufficient to capture the key scattering features of a vertical-axis wind turbine. Subsequently, simulation of a 112 m tall Darrieus-type vertical-axis wind turbine was carried out. In this case, in-situ measurement was not performed, as these types of structures are presently under consideration for future off-shore wind power generation.

In Chapter 5, wide-angle ISAR imaging of vehicles from a stationary roadside radar was investigated for potential applications in vehicle classification. First, baseline ISAR images were obtained in the cooperative measurement scenario with a ranging radio. The resulting images showed a clear distinction between different-sized vehicles. The images were then further focused through motion compensation using a p -norm minimization. The resulting images were well focused and corresponded closely to the physical dimensions of the vehicles. Subsequently, we investigated the non-cooperative imaging scenario. In this case, the vehicle range was estimated based on the measured range profile centroid. Again, p -norm minimization was applied, and the resulting images were well focused and corresponded closely to the physical dimensions of the vehicles.

In Chapter 6, a laboratory measurement study of the radar signatures of several consumer drones was first performed. The results showed that the non-plastic portions of the drones (battery pack, motors, carbon fiber frame, etc.) dominate their radar signatures. It was also shown that the plastic drone blades do not contribute a significant return (while stationary or spinning). While the overall radar cross section level is low, the resulting ISAR images revealed the size and geometrical outlines of each drone, which could facilitate drone detection and identification. Subsequently, in-situ ISAR imaging of a consumer drone in flight from a stationary radar on the ground was investigated. While the resulting images were well focused in cross-range, the narrower bandwidth (compared to laboratory measurement) of the radar and the limited number of distinct scatterers on the drone make in-situ drone detection and identification, at this time, challenging.

In Chapter 7, we departed from the previous topics of generating an ISAR image of a moving target from a stationary UWB radar. Instead, we took advantage of the portable and lightweight radar and mounted it on a consumer drone to carry out aerial SAR imaging of scenes on the ground. The entire system including the radar, antennas, and a single-board computer fits on a small consumer drone and can be controlled through a Wi-Fi connection. Both the side-looking and downward-looking SAR scenarios were investigated.

Overall, this dissertation investigated the use of a UWB radar for in-situ, high-resolution radar imaging of moving targets and developed the required measurement and processing methodologies to achieve equally high range and cross-range resolution. Each class of targets examined in this dissertation was of considerable current interest, and high-resolution radar imaging showed promising potential applications. Some future work that warrants further investigation is discussed in the following section.

8.2 FUTURE WORK

We have established the methodology to ISAR image a wind turbine in-situ. Small wind turbines were fully captured by the radar but, due to hardware limitations, only the inner portion of the utility-class wind turbine was imaged. Continued improvements to UWB radar technology, in particular to the maximum sampling rate, will allow for these utility-class wind turbines to be fully captured. Alternatively, imaging the wind turbine from the frontal-view could achieve similar results (as the incident angle effectively compresses the maximum Doppler extent of the turbine). There are two additional considerations that should be taken into account when using this approach. First, due to the increased distance, SNR may become an issue. Thus, a larger transmit power may be required. Second, at the frontal view, the validity of the near-field-to-far-field transformation should be more carefully examined.

Since ISAR imaging maps dominant scattering features in a 2-D space, it assists in the understanding of wind turbine scattering phenomenology. This, in turn, can facilitate the development of clutter mitigation algorithms and wind turbines with reduced RCS. For example, it may be possible to construct matched filters based on the sparse features of turbine scattering to de-clutter the return of wind turbine contribution. Similarly, selective treatment of turbine surfaces that give rise to high scattering with radar absorbing materials could result in stealthy turbine structures. Finally, high-resolution ISAR images could be used for structural health monitoring of the wind turbines blades. Wind turbine blades require routine inspection as they are subject to normal wear and tear over its life cycle as well as lightning strike damage. Early detection of cracks and tears is key to prevent catastrophic damage to the turbine. This is currently done through close-up visual inspection by an inspection worker or through the use of optical cameras, during which, the wind turbine is manually stopped. Radar

imaging could provide 24-hour, all-weather monitoring without the need to interrupt the wind turbine from power generation.

We have also established the methodology to ISAR image a vehicle in-situ. Two further improvements could be made. In the results shown, the features in the front and rear of the vehicles are lacking. This can be remedied through data collection over a wider angular swath. Additional features could also be revealed by using a second radar that is displaced in elevation from the first, to carry out interferometry. By comparing the phase of the two SAR images acquired at two different elevation angles, it may allow vehicle height information to be extracted. Thus, 3-D vehicle radar imaging could be achieved. This has potential applications in vehicle classification for perimeter security and traffic monitoring for intelligent transportation systems. Through in-situ measurements of different vehicles, a database may be formed that would facilitate automatic vehicle classification and/or identification. Another particularly interesting application is in the area of self-driving cars [92]. Assistance by a road-side radar that is able to track and subsequently image vehicles in addition to what is already available on the self-driving vehicle can improve reliability and safety.

For small consumer drones, we have successfully generated their ISAR images in laboratory measurement. However, the resulting in-situ images using the UWB radar were less distinctive in capturing the drone shape and size due to the smaller bandwidth. In this case, increasing the pulse bandwidth of the radar should improve results—admittedly, this is subject to emission regulations. Nonetheless, the methodology has been established and the ability to distinguish between two different-sized drones was shown. Therefore, with the continued advancements in UWB radar technology, tracking and subsequent classification of small consumer drones could potentially be achieved.

Finally, the drone-SAR system showed promising results. The most immediate future work is to implement image focusing using the drone's built-in GPS flight data. Once GPS-assisted image focusing is achieved, a low-cost drone-SAR system could open up potential applications in scientific, agricultural, environmental, and structural health monitoring that were cost-prohibitive in the past. The following are some examples. Scientific and environmental monitoring is currently done using SAR systems mounted underneath airplanes or large UAVs. By making repeat flights (along the same path) periodically over many years, the change in radar imagery over time can be investigated. However, each measurement campaign is costly, thus restricting the time interval between flights. SAR imaging using consumer drones could be useful in cases where a higher frequency of repeat flights is desirable. Furthermore, through the use of multiple drones in the air, we are no longer limited to the monostatic scenario and could allow for bistatic or multistatic measurements. It is also well known that SAR imaging could reveal soil moisture content. Therefore, a drone-SAR system could potentially be used to monitor agricultural crops. Finally, consumer drones are an excellent candidate for structural health monitoring, and are already being used to do so via the on-board camera. The addition of a drone-SAR system that operates concurrently with the on-board camera could provide additional information that is not available optically.

Appendix: Near-Field to Far-Field Transformation

In this Appendix, we summarize the formulation of the Mensa and Vaccaro algorithm for near-field to far-field transformation (NFFFT) [68, 69] (we shall denote this as Mensa's algorithm from this point forward). To preface, there are several methods to transform near-field scattering data to far-field scattering data [68, 93, 94]. Mensa's algorithm [68] is chosen in this dissertation because it is easy to implement and can be applied for monostatic data collection. However, the transformation is an approximation. It can be derived using a combination of Huygens' (or equivalence) principle, the stationary phase approximation, and the point-scatterer model. A few simplifying assumptions that are used in the original Mensa formulation are: (i) scalar wave theory, (ii) point-scatterer model of the target scattering with no higher-order scattering, (iii) 1-D angular monostatic RCS data collection in the waterline plane of the target, and (iv) correcting the phase of the near-field data is of primary concern (this results in correcting the location of point scatterers in the final radar image), not the amplitude. While Mensa's algorithm has been described in [68, 69], for clarity, we provide a more detailed description of its derivation here.

The problem geometry is shown in Fig. A.1, where a plane wave field $E^{i,ff}$ is incident on a point scatterer and $E^{s,ff}$ is the observed backscattered far field, both in the directions shown. The objective here is to relate $E^{s,ff}$ to the incident and scattered fields in the near-field region of the target. The final goal is to obtain an expression that allows for transformation of collected near-field RCS data from a near-field source into the far-field RCS data from a far-field source.

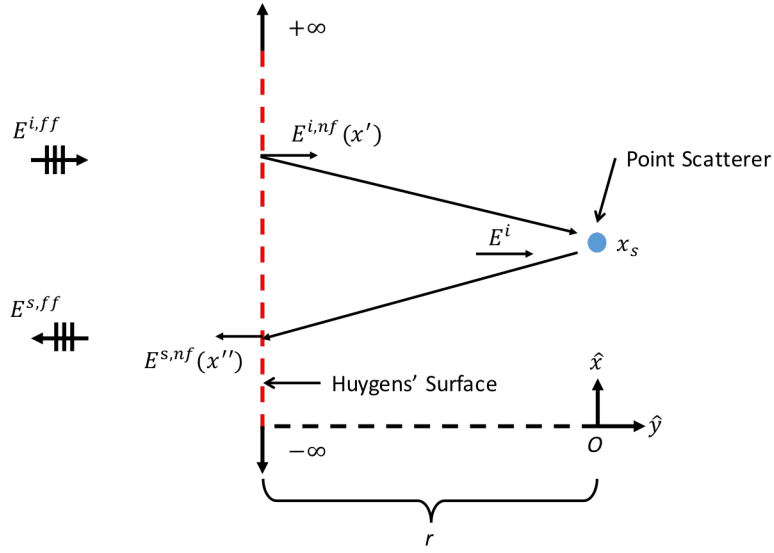


Fig. A.1 Problem geometry for planar Huygens' surface with a single point scatterer.

From Huygens' principle, we can choose a Huygens' surface in the near-field region of the target point scatterer. Now, an equivalent source can be placed on the surface such that the same incident field E^i impinges on the target as that of the original plane wave $E^{i,ff}$. If a planar Huygens' surface at a distance r from the origin O is chosen, the expression that relates E^i to the equivalent source is:

$$E^i = E^{i,ff} = \int_{-\infty}^{\infty} E^{i,nf}(x') e^{-jk\sqrt{r^2+(x_s-x')^2}} dx' \quad (\text{A.1})$$

where $E^{i,nf}(x')$ is the incident plane wave $E^{i,ff}$ observed on the Huygens' surface. Similarly, we can use Huygens' principle to relate $E^{s,ff}$ to the scattered near-field $E^{s,nf}$ observed on the same Huygens' surface due to scattering of E^i by the target.

$$E^{s,ff} = \int_{-\infty}^{\infty} E^{s,nf}(x'') dx'' \quad (\text{A.2})$$

Note that the same phase delay to the far field on the left is shared by all the radiating equivalent point sources on the plane, and thus the extra phase term is suppressed in Eq. (A.2).

Using the point-scatterer model, we can relate the scattered near-field observed on the Huygens' surface to the incident field E^i as:

$$E^{s,nf}(x'') = A^s E^i e^{-jk\sqrt{r^2+(x_s-x'')^2}} \quad (\text{A.3})$$

where the phase factor accounts for the phase delay from the target back to the Huygens' surface, and A^s is the scattering amplitude of the target. Then, by combining Eqs. (A.1-A.3), the scattered far field can be obtained as:

$$E^{s,ff} = \int_{-\infty}^{\infty} e^{-jk\sqrt{r^2+(x_s-x')^2}} dx' \int_{-\infty}^{\infty} e^{-jk\sqrt{r^2+(x_s-x'')^2}} dx'' \quad (\text{A.4})$$

In obtaining Eq. A.4, for simplicity, we have assumed both A^s and $E^{i,nf}$ are unity. The latter is done since the incident plane wave observed on the Huygens' surface is equi-phase and uniform in amplitude everywhere along the planar Huygens' surface. Examining Eq. A.4, we can see that the first integral is the summation of the fields observed along the Huygens' surface radiated to the target, and the second integral is the summation of the fields observed along the Huygens' surface that were radiated back

from the target. To evaluate each integral, the stationary phase approximation [95] is applied and the following closed-form expression is obtained:

$$\begin{aligned}
 E^{s,ff} &\cong e^{-jkr} \sqrt{\frac{2\pi r}{jk}} e^{-jkr} \sqrt{\frac{2\pi r}{jk}} \\
 &\cong e^{-j2kr} \frac{2\pi r}{jk}
 \end{aligned}
 \tag{A.5}$$

The final result in Eq. (A.5) is consistent with what one would expect the far-field backscattering from a point scatterer to be (with an unimportant scaling factor). However, implementing Eq. (A.4) would be an extremely laborious measurement to make. It requires that for each transmit location x' on the Huygens' surface, we collect the scattered field at all receive locations x'' on the same Huygens' surface—essentially measuring the full bistatic response of the target. Thus, a monostatic expression would be preferred.

Next, the monostatic scenario is shown in Fig. A.2. We choose the monostatic collection aperture to be the same as the Huygens' surface in the previous derivation, where the phase delay from the Huygens' surface to the point target is now the same as the phase delay from the point target back to the Huygens' surface. Therefore, the expression for the measured monostatic data along the near-field collection aperture is (again, the scattering amplitude A^s is assumed to be unity):

$$E^{meas}(x) = e^{-j2k\sqrt{r^2+(x_s-x)^2}}
 \tag{A.6}$$

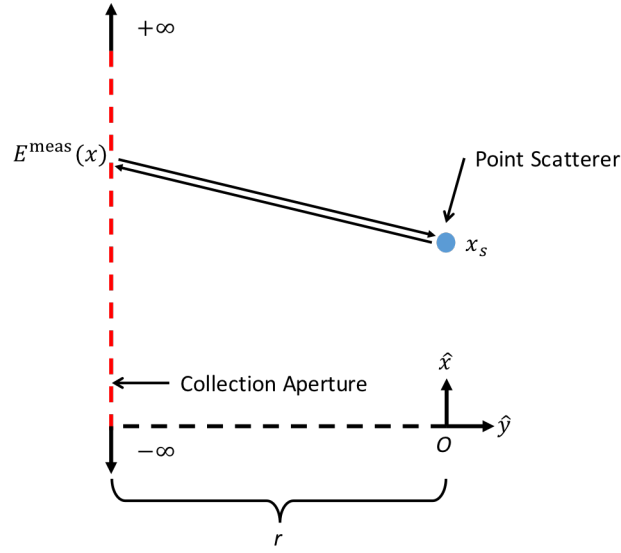


Fig. A.2 Problem geometry for planar aperture under the monostatic scenario.

Mensa's NFFFT algorithm entails integrating the measured monostatic field over the entire collection aperture:

$$E^{s,ff} = \int_{-\infty}^{\infty} E^{meas}(x) dx \quad (\text{A.7})$$

By plugging Eq. (A.6) into Eq. (A.7) and applying the stationary phase approximation, we arrive at:

$$E^{s,ff} = \int_{-\infty}^{\infty} e^{-j2k\sqrt{r^2+(x_s-x)^2}} dx \cong e^{-j2kr} \sqrt{\frac{2\pi r}{j2k}} \quad (\text{A.8})$$

We notice that, with the exception of an unimportant scaling factor, the resulting expression in Eq. (A.8) is the same as Eq. (A.5). The far-field phase, which is of primary

concern, has been recovered in Eq. (A.8). Since Eq. (A.8) comes from Eq. (A.7), and Eq. (A.5) comes from Eq. (A.4), we can conclude that Eq. (A.4), which was derived based on Huygens' principle, can be approximated by integrating the measured monostatic near field over the collection aperture, as shown in Eq. (A.7). This is a key intermediate result of Mensa's algorithm.

To further simplify data collection, a similar derivation can be applied to a circular Huygens' surface instead of a planar surface. Fig. A.3 shows the problem geometry for a circular Huygens' surface. Note, the point scatterer is in the center of the problem geometry for simplicity, but it is not a necessary condition. Now, the field incident on the target can be expressed as the following:

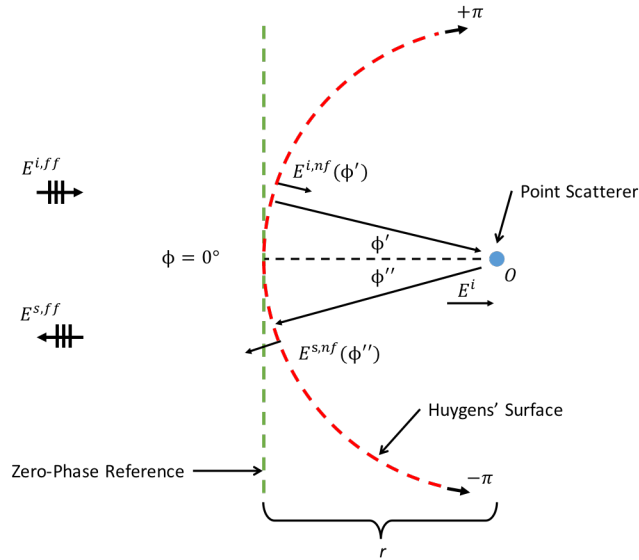


Fig. A.3 Problem geometry for circular Huygens' surface with a single point scatterer.

$$E^i = E^{i,ff} = \int_{-\pi}^{\pi} E^{i,nf}(\phi') e^{-jkr} r d\phi' \quad (\text{A.9})$$

However, unlike the planar Huygens' surface scenario, we cannot assume equi-phase fields to be observed along the circular Huygens' surface. Thus, relative to the zero-phase reference plane shown in Fig. A.3, the field observed on the Huygens' surface is now (with the amplitude set to unity):

$$E^{i,nf}(\phi') = e^{-j2krsin^2\left(\frac{\phi'}{2}\right)} \quad (\text{A.10})$$

Again, we apply Huygens' principle a second time in order to relate $E^{s,ff}$ to $E^{s,nf}$ on the circular Huygens' surface. In this case, the radiating equivalent point sources on the Huygens' surface do not share the same phase delay to the far field on the left, and an extra phase term is needed.

$$E^{s,ff} = \int_{-\pi}^{\pi} E^{s,nf}(\phi'') e^{-j2krsin^2\left(\frac{\phi''}{2}\right)} r d\phi'' \quad (\text{A.11})$$

Using the point-scatterer model (and assuming A^s is unity), we can relate $E^{s,nf}$ to E^i as:

$$E^{s,nf}(\phi'') = E^i e^{-jkr} \quad (\text{A.12})$$

Since we have chosen our circular Huygens' surface such that the point target is at the center, the observed scattered field on the surface is the same regardless of the observation angle. Finally, by combining Eqs. (A.9-A.12) and applying the stationary phase approximation, we obtain the following expression:

$$\begin{aligned}
E^{s,ff} &= \int_{-\pi}^{\pi} e^{-jkr} e^{-j2krsin^2(\frac{\phi'}{2})} r d\phi' \int_{-\pi}^{\pi} e^{-jkr} e^{-j2krsin^2(\frac{\phi''}{2})} r d\phi'' \\
&\cong e^{-jkr} \sqrt{\frac{2\pi r}{jk}} e^{-jkr} \sqrt{\frac{2\pi r}{jk}} = e^{-j2kr} \frac{2\pi r}{jk}
\end{aligned}
\tag{A.13}$$

The final result is the same as with the planar Huygens' surface. This is to be expected since Huygens' principle is equivalent for any arbitrary surface. Overall, Eq. (A.13) shows that a NFFFT can also be performed from the full bistatic measurements on a circular Huygens' surface.

Next, we examine the monostatic scenario shown in Fig. A.14. Here, E^{meas} is simply (again, A^s is assumed to be unity):

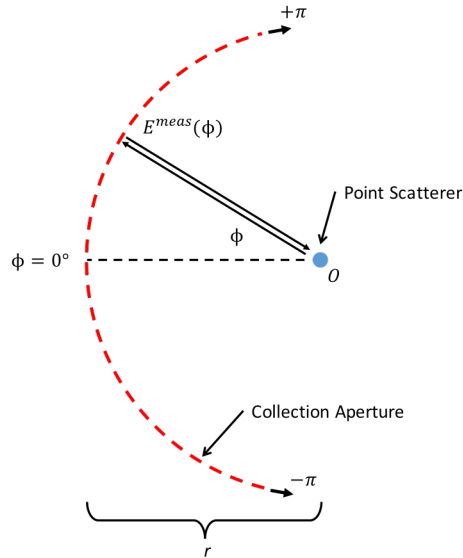


Fig. A.4 Problem geometry for circular aperture under the monostatic scenario.

$$E^{meas}(\phi) = e^{-j2kr} \quad (\text{A.14})$$

Applying Mensa's algorithm, we again integrate the measured monostatic data over the entire aperture. However, unlike the planar aperture case, the data should be weighted by a phase-correcting term:

$$E^{s,ff} = \int_{-\pi}^{\pi} E^{meas}(\phi) e^{-j4kr \sin^2(\frac{\phi}{2})} r \, d\phi \quad (\text{A.15})$$

Substituting Eq. (A.14) into Eq. (A.15) and applying the stationary phase approximation, we arrive at:

$$E^{s,ff} = \int_{-\pi}^{\pi} e^{-j2kr} e^{-j4kr \sin^2(\frac{\phi}{2})} r \, d\phi \cong e^{-j2kr} \sqrt{\frac{2\pi r}{j2k}} \quad (\text{A.16})$$

As with before, the final result using Huygens' principle and the final result using the Mensa's algorithm, after the stationary phase approximation, are the same (except for an unimportant scaling constant). This means the far-field data can be reconstructed by integrating the monostatic data that was collected in a circular arc around the target, as shown by Eq. (A.15). The transform can also be applied to data collected using the inverse scenario, i.e. from a stationary radar and a rotating target.

Finally, some concluding remarks. First, we have shown that the chosen mathematical operation in Eq. (A.15) is an NFFFT that can be performed after collecting only monostatic near-field data along the Huygens' surface. In practice, the integration must be implemented numerically and only a finite integration limit with sufficient

sampling density is required for convergence. Furthermore, more complex targets (such as wind turbines) can be modeled as a collection of discrete point scatterers, and this only changes the required integration limit and sampling density. The details of the last two points were investigated in detail in [69]. Eq. (3.4) in the main body of the dissertation shows a discretized implementation of (A.15). The recommended choices for the integration limit and the sampling density from [69] are adopted.

References

- [1] M. Skolnik, *Introduction to Radar Systems*, 3rd Ed., Boston: McGraw Hill, 2001.
- [2] D. R. Wehner, *High Resolution Radar*, 2nd Ed., Boston: Artech House, 1995.
- [3] J. C. Curlander and R. N. McDonough, *Synthetic Aperture Radar, Systems & Signal Processing*, New York: John Wiley & Sons, Inc., 1991.
- [4] C. A. Wiley, "Pulse Doppler radar methods and apparatus," US Patent 3196436 A, July 20, 1965.
- [5] M. Soumekh, *Synthetic Aperture Radar Signal Processing with MATLAB Algorithms*, New York: Wiley, 1999.
- [6] D. E. Wahl, P. H. Eichel, D. C. Ghiglia, and C. V. Jakowatz, Jr., "Phase gradient autofocus—a robust tool for high resolution SAR phase correction," *IEEE Trans. Aerosp. Electron. Syst.*, vol. 30, pp. 827-835, Jul. 1994.
- [7] D. L. Mensa, *High Resolution Radar Cross-Section Imaging*, Norwood: Artech House, 1991.
- [8] C. C. Chen and H. C. Andrews, "Target-motion induced radar imaging," *IEEE Trans. Aerosp. Electron. Syst.*, vol. AES-16, pp. 2-14, Jan. 1980.
- [9] T. Sauer and A. Schroth, "Robust range alignment algorithm via Hough transform in an ISAR imaging system," *IEEE Trans. Aerosp. Electron. Syst.*, vol. 31, pp. 1173-1177, Jul. 1995.
- [10] Y. Wang, H. Ling, and V. C. Chen, "ISAR motion compensation via adaptive joint time-frequency technique", *IEEE Trans. Aerosp. Electron. Syst.*, vol. 34, pp. 670-677, Apr. 1998.
- [11] V. C. Chen and H. Ling, *Time-Frequency Transforms for Radar Imaging and Signal Analysis*, Norwood: Artech House, 2002.

- [12] J. Wang and D. Kasilingam, "Global range alignment for ISAR," *IEEE Trans. Aerosp. Electron. Syst.*, vol. 39, pp. 351-357, Jan. 2003.
- [13] D. Y. Zhu, L. Wang, Y. S. Yu, Q. N. Tao, and Z. D. Zhu, "Robust ISAR range alignment via minimizing the entropy of the average range profiles," *IEEE Geosci. Remote. Sens. Lett.*, vol. 6, pp. 204-208, Jan. 2009.
- [14] Federal Communications Commission, "Revision of Part 15 of the Commission's Rules Regarding Ultra-Wideband Transmission Systems," *FCC 02-48*, Apr. 2002.
- [15] C. Zhang, A. Fathy, and M. Mahfouz, "Performance enhancement of a sub-sampling circuit for ultra-wideband signal processing," *IEEE Microw. Wireless Compon. Lett.*, vol. 17, pp. 873-875, Dec. 2007.
- [16] D. Lee, J. Sung, and J. Park, "A 16ps-resolution random equivalent sampling circuit for TDR utilizing a Vernier time delay generation," in *Proc. IEEE Nuclear Sci. Symp.*, Portland, OR, Oct. 2003.
- [17] L. Nguyen, D. Wong, M. Ressler, and F. Koeing, "Obstacle avoidance and concealed target detection using the Army Research Lab ultra-wideband synchronous impulse reconstruction (UWB SIRE) forward imaging radar," in *Proc. of SPIE*, vol. 6553, pp. 65530H-1-65530H-8, Apr. 2007.
- [18] Y. Yang and A. Fathy, "Development and implementation of a real-time see-through-wall radar system based on FPGA," *IEEE Trans. Geosci. Remote Sens.*, vol. 47, pp. 1270-1280, May 2009.
- [19] PulsON 410, Time Domain, Huntsville, AL, 2013 [Online]. Available: <http://www.timedomain.com/p400-mrm.php>
- [20] S. Nag, M. A. Barnes, T. Payment, and G. Holladay, "An ultrawideband through-wall radar for detecting the motion of people in real time," in *Proc. SPIE, Radar Sensor Technology and Data Visualization*, 48, vol. 4744, pp. 48-57, 30 July 2002.

- [21] A. R. Hunt, "A wideband imaging radar for through-the-wall surveillance," in *Proc. SPIE, Sensors, and Command, Control, Communications, and Intelligence (C3I) Technologies for Homeland Security and Homeland Defense III*, vol. 5403, pp. 590-596, Sept. 2004.
- [22] Y.-J. Ren, C.-P. Lai, P.-H. Chen, and R. Narayanan, "Compact ultrawideband UHF array antenna for through-wall radar applications," *IEEE Antennas Wireless Propag. Lett.*, vol. 8, pp. 1302-1305, Dec. 2009.
- [23] Q. Liu, Y. Wang, and A. Fathy, "Towards low cost, high speed data sampling module for multifunctional real-time UWB radar," *IEEE Trans. Aerosp. Electron. Syst.*, vol. 49, pp. 1301-1316, Apr. 2013.
- [24] S.-T. Yang, "Design and application of microstrip leaky wave antennas for radar sensing," Ph.D. dissertation, The University of Texas at Austin, Austin, TX, 2014.
- [25] Y. Wang, "UWB pulse radar for human and Doppler detection applications," Ph.D. dissertation, University of Tennessee, Knoxville, TN, 2012.
- [26] Y.-S. Yoon and M. G. Amin, "High-resolution through-the-wall radar imaging using beamspace MUSIC," *IEEE Trans. Antennas Propag.*, vol. 56, pp. 1763-1774, June 2008.
- [27] S. S. Ram and H. Ling, "Through-wall tracking of human movers using joint Doppler and array processing," *IEEE Geosci. Remote Sens. Lett.*, vol. 5, pp. 537-541, July 2008.
- [28] P. C. Chang, R. J. Burkholder, and J. L. Volakis, "Adaptive CLEAN with target refocusing for through-wall image improvement," *IEEE Trans. Antennas Propag.*, vol. 58, pp. 155-162, Jan. 2010.
- [29] M. Aftanas, "Through wall imaging with UWB radar system," Ph.D. dissertation, Technical University of Kosice, Kosice, Slovakia, 2009.

- [30] B. Levitas and J. Matuzas, "UWB radar high resolution ISAR", in *Ultrawideband and Ultrashort Impulse Signals (UWBUSIS)*, Sevastopol, Ukraine, pp. 228-230, Sept. 2004.
- [31] The Effects of Wind Turbine Farms on Air Defence Radars, Air Warfare Center, Royal Air Force, UK, Jan. 2005.
- [32] Report to the Congressional Defense Committees on The Effect of Windmill Farms On Military Readiness, United States Department of Defense Report to the Congressional Defense Committees, Aug. 2006.
- [33] Radar, Radio Links, and Wind Turbines, 60th IEA Topical Expert Meeting, Senternovem, Netherlands, Nov. 18-19, 2009.
- [34] H. Ling, M. F. Hamilton, R. Bhalla, W. E. Brown, T. A. Hay, N. J. Whiteloni, S.-T. Yang and A. Naqvi, "Assessment of offshore wind farm effects on sea surface, subsurface and airborne electronic systems," Final Report for DE-EE0005380, Dept. of Energy, Sept. 2013.
- [35] B. M. Kent, A. Buterbaugh, K. C. Hill, G. Zelinski, R. Hawley, L. Cravens, T. Van, C. Vogel, and T. Coveyou, "Dynamic radar cross section and radar Doppler measurements of commercial General Electric windmill power turbines part 1 – predicted and measured radar signatures," *IEEE Antennas Propag. Mag.*, vol. 50, no. 2, pp. 211-219, Apr. 2008.
- [36] A. Buterbaugh, B. M. Kent, K. C. Hill, G. Zelinski, R. Hawley, L. Cravens, T. Van, C. Vogel, and T. Coveyou, "Dynamic radar cross section and radar Doppler measurements of commercial General Electric windmill power turbines part 2 – predicted and measured radar signatures," in *Proc. 2007 AMTA Symp.*, St. Louis, MO, pp. 1-7, Nov. 2007.

- [37] G. Greving, W.-D. Biermann, and R. Mundt, "On the relevance of the measured or calculated RCS for objects on the ground – case wind turbines," in *Proc. European Conf. Antennas Propag. (EuCAP)*, Berlin, Germany, pp. 2216-2220, Mar. 2009.
- [38] E. Van Lil, D. Trappeniers, J. De Belser, and A. Van de Capelle, "Computations of radar returns of wind turbines," in *Proc. European Conf. Antennas Propag. (EuCAP)*, Berlin, Germany, pp. 3852-3856, Mar. 2009.
- [39] A. Naqvi, S.-T. Yang, and H. Ling, "Investigation of Doppler features from wind turbine scattering," *IEEE Antennas Wireless Propag. Lett.*, vol. 9, pp. 485-488, 2010.
- [40] A. Belmonte and X. Fabregas, "Analysis of wind turbines blockage on Doppler weather radar beams," *IEEE Antennas Wireless Propag. Lett.*, vol. 9, pp. 670–673, 2010.
- [41] I. Angulo, D. de la Vega, O. Rodriguez, O. Grande, and D. Guerra, "Analysis of the mast contribution to the scattering pattern of wind turbines in the UHF band," in *Proc. European Conf. Antennas Propag. (EuCAP)*, Rome, Italy, pp. 707-711, Apr. 2011.
- [42] Y. Zhang, A. Huston, R. D. Palmer, R. Albertson, F. Kong, and S. Wang, "Using scaled models for wind turbine EM scattering characterization: techniques and experiments," *IEEE Trans. Instrum. Meas.*, vol. 60., pp. 1298-1306, Apr. 2011.
- [43] D. Jenn and C. Ton, "Wind turbine radar cross section," *Int. J. Antennas Propag.*, vol. 2012, 14 pages, 2012.
- [44] L. Danoon and A. K. Brown, "Modeling methodology for computing the radar cross section and Doppler signature of wind farms," *IEEE Trans. Antennas Propag.*, vol. 61, pp. 5166-5174, Oct. 2013.

- [45] M. J. Algar, L. Lozano, J. Moreno, I. Gonzalez, and F. Catedra, "Application of asymptotic and rigorous techniques for the characterization of interferences caused by a wind turbine in its neighborhood," *Int. J. Antennas Propag.*, vol. 2013, 10 pages, 2013.
- [46] C. J. Li, R. Bhalla, and H. Ling, "Investigation of the dynamic radar signatures of a vertical-axis wind turbine," *IEEE Antennas Wireless Propag. Lett.*, vol. 14, pp. 763-766, 2014.
- [47] C. J. Li, S.-T. Yang, and H. Ling, "ISAR imaging of a windmill - measurement and simulation," in *Proc. European Conf. Antennas Propag. (EuCAP)*, the Hague, Netherlands, pp. 4434-4438, Apr. 2014.
- [48] Sandia National Laboratories, *Sandia Labs News Releases*, July 30, 2012 [Online]. Available: <http://www.sandia.gov/news/>.
- [49] T. D. Ross, S. W. Worrell, V. J. Velton, J. C. Mossing, and M. L. Bryant, "Standard SAR ATR evaluation experiments using the MSTAR public release data set," in *Proc. SPIE Algorithms for Synthetic Aperture Imagery V*, vol. 3370, pp. 566-773, Apr. 1998.
- [50] M. L. Bryant and F. D. Garber, "SVM classifier applied to MSTAR public data set," in *Proc. SPIE Algorithms for Synthetic Aperture Imagery VI*, vol. 3721, pp. 355-360, Apr. 1999.
- [51] M. Boshra and B. Bhanu, "Bounding SAR ATR performance based on model similarity," in *Proc. SPIE Algorithms for Synthetic Aperture Imagery VI*, vol. 3721, pp. 716-729, Apr. 1999.
- [52] Y. Sun, Z. Liu, S. Todorovic, and J. Li, "Adaptive boosting for SAR automatic target recognition," *IEEE Trans. Aerosp. Electron. Syst.*, vol. 43, pp. 112-125, Jan. 2007.

- [53] L. E. Y. Mimbela and L. A. Klein. "Summary of vehicle detection and surveillance technologies used in intelligent transportation systems," The Vehicle Detector Clearinghouse, Aug. 2007 [Online]. Available: <http://www.fhwa.dot.gov/policyinformation/pubs/vdstits2007>.
- [54] J. Holzner, U. Gebhardt, and P. Berens, "Autofocus for high resolution ISAR imaging," in *Proc. European Conference on Synthetic Aperture Radar (EUSAR 2010)*, Aachen, Germany, pp. 720-723, June 2010.
- [55] J. S. Kulpa, M. Malanowski, D. Gromek, P. Samczynski, K. Kupla, and A. Gromek, "Experimental results of high-resolution ISAR imaging of ground-moving vehicles with a stationary FMCW radar," *Int. J. Electron. Telecomm.*, vol. 59, pp. 293-299, 2013.
- [56] G. Rubin, E. V. Sager, and D. H. Berger, "GPU acceleration of SAR/ISAR imaging algorithms," in *Proc. Antenna Measurement Techniques Association Symp. (AMTA 2010)*, Atlanta, Georgia, pp. 430-435, Oct. 2010.
- [57] "Amazon unveils futuristic plan: delivery by drone," CBS News, 60 Minutes: Overtime, Dec. 2013 [Online]. Available: <http://www.cbsnews.com/news/amazon-unveils-futuristic-plan-delivery-by-drone>.
- [58] D. Schultz, "Game of Drones," *Science*, vol. 347, pg. 497, Jan. 2015.
- [59] Federal Aviation Administration, "Operation and Certification of Small Unmanned Aircraft Systems," *FAA-2015-0150*, Feb. 2015.
- [60] L. V. Morris, "On or coming to your campus soon: drones," *Innov. High. Educ.*, vol. 40, pp. 1-2, Apr. 2015.
- [61] J. B. Keller, "Geometrical theory of diffraction," *J. Opt. Soc. Am.*, vol. 52, pp. 116-130, Jan. 1962.

- [62] R. G. Kouyoumjian, "The geometrical theory of diffraction and its applications," in *Numerical and Asymptotic Techniques in Electromagnetics*, ed. by R. Mittra, New York: Springer-Verlag, 1975.
- [63] W. H. Press, B. P. Flannery, S. A. Teukolsky, W. T. Vetterling, *Numerical Recipes* (2nd Ed.), New York: Cambridge University Press, 1986.
- [64] FEKO Version 6.3, EM Software & Systems, Stellenbosch, South Africa, 2013 [Online]. Available: <http://www.feko.info>.
- [65] FEKO (Nov. 2013), *FEKO Student Paper Competition Results for 2013* [Online]. Available: <https://www.feko.info/about-us/News/feko-student-competition-results-for-2013>.
- [66] H. Ling, R.-C. Chou, S.-W. Lee, "Shooting and bouncing rays: calculating the RCS of an arbitrarily shaped cavity," *IEEE Trans. Antennas Propagat.*, vol. 37, pp. 194-205, Feb. 1989.
- [67] D. C. Munson, J. D. O'Brien, and W. K. Jenkins, "A tomographic formulation of spotlight-mode synthetic aperture radar," *Proceedings of the IEEE*, vol. 71, pp. 917-925, Aug. 1983.
- [68] D. L. Mensa and K. Vaccaro, "Near-field to far-field transformation of RCS data," in *Proc. AMTA Symp.*, Williamsburg, VA, pp. 155-161, Nov. 1995.
- [69] N. Whiteloni, S.-T. Yang, and H. Ling, "Application of near-field to far-field transformation to Doppler features from wind turbine scattering," *IEEE Trans. Antennas Propagat.*, vol. 60, pp. 1660-1665, Mar. 2012. (The factor of two in the first phase term shown in Eq. (3) is incorrect. It should be replaced by a factor of four.)
- [70] J. Pinto, J. C. G. Matthews, and C. Sarno, "Stealth technology for wind turbines," *IET Radar Sonar Navig.*, vol. 4, pp. 126-133, 2010.

- [71] J. J. McDonald, B. C. Brock, S. E. Allen, P. G. Clem, J. A. Paquette, W. E. Patitz, W. K. Miller, D. A. Calkins, and H. J. Loui, "Radar-cross-section reduction of wind turbines (Part 1)," Sandia National Labs, Rept. SAND2012-0480, Mar. 2012.
- [72] A. Naqvi, N. Whiteloni, and H. Ling, "Doppler features from wind turbine scattering in the presence of ground," *Progress Electromag. Research Lett.*, vol. 35, pp. 1-10, 2012.
- [73] D. L. Donoho, "Sparse components of images and optimal atomic decomposition," *Constructive Approx.*, vol. 17, pp. 353-382, 2001.
- [74] Federal Aviation Administration, "Registration and marking requirements for small unmanned aircraft," FAA-2015-7396, Dec. 2015.
- [75] Federal Aviation Administration, "FAA Tests FBI Drone Detection System at JFK," May 2016 [Online]. <http://www.faa.gov/news/updates/?newsId=85546>
- [76] Advanced Radar Technologies, Madrid, Spain, "ART drone sentinel product brief," May 2015 [Online]. <http://www.advancedradartechnologies.com/products-services/art-drone-sentinel>.
- [77] F. Fioranelli, M. Ritchie, H. Griffiths, and H. Borrión, "Classification of loaded/unloaded micro-drones using multistatic radar," *IET Elec. Lett.*, vol. 51, no. 22, pp. 1813-1815, 2015.
- [78] J. Bric, "Imaging a BQM-74E target drone using coherent radar cross section measurements," *Johns Hopkins APL Technical Digest*, vol. 18, no. 3, pp. 365-376, 1997.
- [79] Efield AB, Kista, Sweden, "RCS simulation of a predator drone," Jan. 2010 [Online]. http://www.efieldsolutions.com/example_rcs_predator.pdf.
- [80] L. To, A. Bati, and D. Hillard, "Radar cross section measurements of small unmanned air vehicle systems in non-cooperative field environments," in *Proc.*

- 2009 *European Conference on Antennas and Propagation*, Berlin, Germany, pp. 3637-3641, Mar. 2009.
- [81] P. Molchanov, K. Egiazarian, J. Astola, R. I. A. Harmanny, "Classification of small UAVs and birds by micro-Doppler signatures," in *Proc. 2013 European Radar Conference*, Nuremberg, Germany, pp. 172-175, Oct. 2013.
- [82] P. Pouliguen, L. Lucas, F. Muller, S. Quete, and C. Terret, "Calculation and analysis of electromagnetic scattering by helicopter rotating blades," *IEEE Trans. Antennas Propagat.*, vol. 50, pp. 1396-1408, Oct. 2002.
- [83] M. Bell and R. A. Grubbs, "JEM modeling and measurement for radar target identification," *IEEE Trans. Aerosp. Elect. Syst.*, vol. 29, pp. 73-87, Jan. 1993.
- [84] DJI, <http://store.dji.com/product/phantom-2>.
- [85] <http://users.ece.utexas.edu/~ling/DroneISARMovie.gif>.
- [86] 3D Robotics, <https://3drobotics.com/>.
- [87] DJI, <http://store.dji.com/product/inspire-1>.
- [88] DJI, <http://www.dji.com/product/phantom-3-adv>.
- [89] S. I. Tsunoda, F. Pace, J. Stence, M. Woodring, W. H. Hensley, A. W. Doerry, and B. C. Walker, "Lynx: A high-resolution synthetic aperture radar," in *IEEE Aerospace Conf. Proc.*, vol. 5, pp. 51-58, Mar. 2000.
- [90] E. C. Zaugg, D. L. Hudson, and D. G. Long, "The BYU μ SAR: a small, student-built SAR for UAV operation," in *Proc. IEEE Int. Geosci. Remote Sens. Symp.*, Denver, CO, pp. 411-414, Aug. 2006.
- [91] V. C. Koo, Y. K. Chan, V. Gobi, M. Y. Chua, C. H. Lim, C. S. Lim, C. C. Thum, T. S. Lim, Z. Ahmad, K. A. Mahood, M. H. Shahid, C. Y. Ang, W. Q. Tan, P. N. Tan, K. S. Yee, W. G. Cheaw, H. S. Boey, A. L. Choo, and B. C. Sew, "A new

- unmanned aerial vehicle synthetic aperture radar for environmental monitoring,” *Progress Electromag. Research*, vol. 122, pp. 245-268, 2012.
- [92] D. Bruemmer. (2016, May 18). Accelerating self-driving cars [Online]. Available: <https://www.linkedin.com/pulse/accelerating-self-driving-cars-david-bruemmer>.
- [93] I. J. LaHaie, “Overview of an image-based technique for predicting far field radar cross-section from near field measurements,” *IEEE Antennas Propagat. Mag.*, 2003.
- [94] H.-J. Li and F.-L. Lin, “Near-field imaging for conducting objects,” *IEEE Trans. Antennas Propagat.*, 1991.
- [95] C. A. Balanis, *Antenna Theory: Analysis and Design*, 3rd Ed., New Jersey: John Wiley & Sons, Inc., 2005, Appendix VIII, pp. 1089-1093.